Electronic Structure and Normal State Properties
in $La_{2-x}Sr_xCuO_4$

Electronic Structure and Normal State Properties in La$_{2-x}$Sr$_x$CuO$_4$

La$_{2-x}$Sr$_x$CuO$_4$ の電子構造及び常伝導相の物性

潮　秀樹

Acknowledgements

Contents

Chapter 1.

Introduction

Since Bednorz and Müller[1] discovered the high T_c superconductivity in $La_{2-x}Ba_xCuO_4$, many types of high T_c superconductors have been discovered[2,3]. The crystal structures of high T_c superconductors are layered-perovskite, consisting of CuO_2 planar sheets and interstitial insulating sheets. They are classified into three types according to the types of Cu-O networks, such as octahedra- (T-phase), square- (T'-phase) and pyramid-type (T*-phase)[2]. They are also classified by the number of Cu-O sheets in a unit cell. There seems to be general agreement that CuO_2 planes play a main role in the superconductivity and normal state transport, and in this context a number of theoretical models have been proposed[4,5]. Most of them are based on a Cu $d_{x^2-y^2}$ - O p_σ band in a CuO_2 sheet. However, it seems difficult to explain high T_c superconductivity by using a model consisting of only a single CuO_2 sheet, because almost all the hole-doped high T_c superconductors consist of pyramid-type CuO_5 or octahedral-type CuO_6 clusters, so that the difference of T_c values in octahedral and pyramid type cuprates seems to be difficult to be explained. On the other hand Kamimura and his co-workers [6,7,8,9,10,11,12,13,14,15,16,17,18] have claimed the important role of the a_{1g}^* band consisting of Cu dz^2 orbitals, Op_σ orbitals in a CuO_2 layer and Op_z orbitals of apical oxygen, due to the effect of Hund's coupling.

In this context it is necessary to calculate the many-body electronic structure of copper oxides from the first principles. From this standpoint, Kamimura and Eto[8]

tried to calculate the electronic structure of a single CuO_6 octahedron embedded in $La_{2-x}Sr_xCuO_4$ (abbreviated as LSCO) from the first principles as accurate as possible, by using the multi-configuration selfconsistent field variational method with configuration interaction. According to Kamimura and Eto the lowest multiplet state of a CuO_6 octahedron changes from the spin-singlet $^1A_{1g}$ state to the spin-triplet $^3B_{1g}$ state when the Sr concentration increases, where A_{1g} and B_{1g} represent irreducible representations of a tetragonal symmetry group D_{4h}. However, the energy difference between the $^3B_{1g}$ and $^1A_{1g}$ multiplet states is at most 0.2eV, and thus these two states are easily mixed by the transfer interactions between neighboring CuO_6 octahedra which is approximately 0.3eV for LSCO.

In order to verify the existence of the $^3B_{1g}$ state which is due to the Hund's coupling, Chen et al.[19] have performed polarization-dependent X-ray absorption measurements for O K-edge and Cu L-edge in LSCO. They have observed the doping-induced satellite peak(L'_3) for both polarizations of the electric vector of X-ray, E, parallel and perpendicular to the c-axis, at the same energy. Their result has suggested that the dopant holes must consist of $^3B_{1g}$ and $^1A_{1g}$ states, since the $E\|c$ and the $E\perp c$ polarizations detect the existence of $^3B_{1g}$ and $^1A_{1g}$ states, respectively.

The coexistence of local antiferromagnetism and superconductivity in LSCO has been observed by, for example, neutron scattering experiments by Birgeneau et al[20]. In other words the localized spins form a two-dimensional local antiferromagnetic (AF) order even in the superconducting state and a dopant hole moves interacting with the localized spins. If we assume that a dopant hole hops from a $^3B_{1g}$ (or an $^1A_{1g}$) multiplet state at one site to the same multiplet state at a neighbouring site, the motion of the dopant hole disturbs the AF order of the localized spins. On the other hand if a dopant hole hops from a $^3B_{1g}$ (or an $^1A_{1g}$) multiplet state at one site to an $^1A_{1g}$ (or a $^3B_{1g}$) multiplet state at a neighbouring site, and then from the $^1A_{1g}$ to the $^3B_{1g}$ state, etc., the local AF order of the localized spins is not disturbed at all.

From this standpoint Kamimura and Suwa[21] have recently constructed a new electronic structure in the underdoped superconducting concentration regime of hole-

doped cuprates. In their model they assumed that the localized spins form local AF order in the area whose diameter is a spin-correlation length, and then that the carriers take the $^3B_{1g}$ high-spin state and the $^1A_{1g}$ low-spin state alternately in this spin-correlated region. In $^3B_{1g}$ state, which is called the Hund's coupling triplet, the dopant hole occupies the antibonding a_{1g}^* orbital consisting of Cu d_{z^2}, in-plane oxygen p_σ and apical oxygen p_z orbitals, and constitutes a spin triplet multiplet with the localized holes accommodated in an antibonding b_{1g}^* orbital consisting mainly of a Cu $d_{x^2-y^2}$ orbital. (See Fig. 1) In the $^1A_{1g}$ state, which is called the Zhang-Rice singlet, the dopant hole occupies the bonding b_{1g} orbital consisting mainly of the in-plane O p_σ orbitals and constitutes a spin singlet multiplet with the localized hole in a b_{1g}^* orbital. The dopant hole hops from the a_{1g}^* orbital at one site to the b_{1g} orbital at the neighboring site, interacting with localized spins.

The characteristic feature of the theoretical model of the coupled fermion-spin system by Kamimura and Suwa is the alternating appearance of the Hund's coupling triplet and the Zhang-Rice singlet in a spin-correlated region of the local antiferromagnetic ordering. This characteristic feature is originally called "two-story house model" by Mott[22] and Cohen[23], but now we call "extended two-story house model"[6,22,23], because the upper story corresponding to the states of itinerant carriers consists of two kinds of orbital states a_{1g}^* and b_{1g}. The effective model Hamiltonian for describing this "extended two-story house model"[6,22,23] is originally expressed as[21,24]

$$
\begin{aligned}
H = &\sum_{i,m,\sigma} \varepsilon_m C_{im\sigma}^\dagger C_{im\sigma} + \sum_{(i,j),m,n,\sigma} t_{mn}(C_{im\sigma}^\dagger C_{jn\sigma} + \text{h.c.}) \\
&+ J\sum_{(i,j)} S_i \cdot S_j + \sum_{i,m} K_m s_{im} \cdot S_i + U\sum_{i,m} n_{im\uparrow} n_{im\downarrow},
\end{aligned}
$$

$$(1.1)$$

where ε_m ($m = a_{1g}^*$ or b_{1g}) represents the effective one-electron energy of the a_{1g}^*- and b_{1g}-orbital states, $C_{im\sigma}^\dagger$ ($C_{im\sigma}$) the creation (annihilation) operator of a dopant hole in the i-th CuO_6 cluster, t_{mn} the effective transfer of a dopant hole between m-type and n-type orbitals of neighboring CuO_6 octahedra, J the superexchange coupling between the spins S_i and S_j of the $d_{x^2-y^2}$ localized holes in the antibonding b_{1g}^* orbital at the nearest Cu
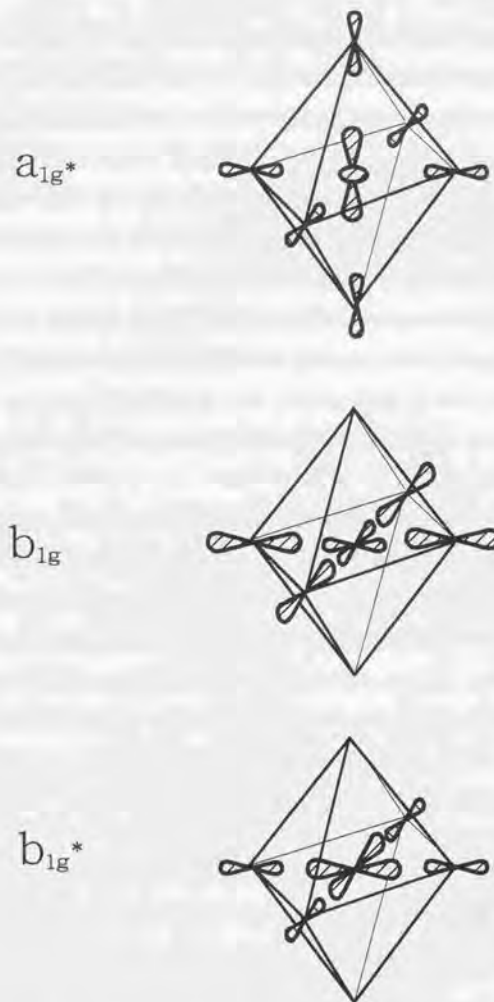
2

3

a_{1g}^*

b_{1g}

b_{1g}^*

Figure 1: The schematical views of an antibonding a_{1g}^* orbital consisting of a Cu d_{z^2} orbital hybridized by in-plane oxygen p_σ and apical oxygen p_z orbitals, a bonding b_{1g} orbital consisting of in-plane oxygen p_σ orbitals hybridized by a Cu $d_{x^2-y^2}$ orbital, and an antibonding b_{1g}^* orbital consisting of a Cu $d_{x^2-y^2}$ orbital hybridized by in-plane oxygen p_σ orbitals.

i and j sites ($J > 0$, antiferromagnetic), K_m the exchange integral between the spins of a dopant hole s_{im} and a $d_{z^2-y^2}$ localized spin S_i in the i-th CuO_6 ($K_{a_{1g}^*} < 0$ for a triplet spin state with a_{1g}^* orbital, ${}^3B_{1g}$, and $K_{b_{1g}} > 0$ for a singlet spin state with b_{1g} orbital, ${}^1A_{1g}$), and U the Hubbard U-like parameter with $n_{im\sigma} = C_{im\sigma}^\dagger C_{jn\sigma}$.

Among many kinds of high T_c superconducting Cu-oxides, LSCO is regarded as the proto-type high T_c superconductor among the hole-doped cuprates, so that it will be powerful approach to high T_c superconductivity to investigate LSCO. The main purposes of the present thesis are to derive an effective one-electron-type energy band structure for a carrier system in LSCO from the Hamiltonian (1.1), to clarify that the alternate appearance of the a_{1g}^* and the b_{1g} orbitals is realized in the CuO_2 network, and to examine the validity of the calculated effective one electron-type band structure, wave functions and Fermi surfaces by comparing the obtained results with experimental ones.

In the present treatment the b_{1g}^* band splits into two bands, the upper and the lower Hubbard bands, due to strong U-effect. The upper Hubbard band is empty while the lower Hubbard band is fully occupied by electrons even in the superconducting LSCO as well as in the undoped La_2CuO_4. And the spins of the holes in upper Hubbard band form the local AF order in the superconducting concentration region due to the superexchange coupling J in the Hamiltonian (1.1). Then we treat the exchange interaction between the spins of a dopant hole and a localized spin in the fourth term in the right hand side of Eq. (1.1) by the molecular field approximation. As a result $\sum_{i,m} K_m s_{im} \cdot S_i$ becomes $\sum_{i,m} K_m s_{im_z} \langle S_i \rangle$ where $\langle S_i \rangle$ is the average value of the sublattice magnetization and z-axis is taken as a direction of the sublattice magnetization. In the present paper, as to the value of $\langle S_i \rangle$, we take that at $T = 0K$ so that $\langle S_i \rangle$ is taken to be $\pm S$ depending on whether the localized spin of the site is up or down. This means that the antiferromagnetic order exists in a whole system but not locally. Since the area of the antiferromagnetic ordering is finite in a real situation, so the present treatment for a perfect antiferromagnetic ordering is a drastic approximation. By this molecular field approximation we can separate the hole carriers and the localized spins. Thus an effective one-electron-type energy band structure for a carrier system in LSCO is calculated.

5

In order to calculate the effective energy bands for a carrier system based on the present approximation for the antiferromagnetic ordering we first adopt an AF unit cell, then derive the effective one electron type 34×34 dimensional Hamiltonian matrix $(\tilde{H}(\boldsymbol{k}))$ and finally diagonalize it, where $2p_x$, $2p_y$ and $2p_z$ atomic orbitals for each of eight oxygen atoms and $3d_{yz}$, $3d_{zx}$, $3d_{xy}$, $3d_{x^2-y^2}$ and $3d_{z^2}$ atomic orbitals for each of two Cu atoms in the unit cell are taken as the basis functions. In this way we have obtained the effective one-electron-type energy band structure, wave functions and the Fermi surfaces at which the Fermi distribution function shows discontinuity for up-spin and down-spin dopant hole carriers separately.

The calculated effective one-electron-type energy band structure shows that, in the concentration below the onset of superconductivity the holes with up-spin are accommodated in b_{1g} orbital constructed from oxygen p_σ orbitals at a CuO_6 cluster with localized up-spin (A-site) while in b_{1g} orbital consisting of hybridized oxygen p_σ and Cu $d_{x^2-y^2}$ orbitals in CuO_2 plane at a CuO_6 cluster with localized down-spin (B-site), consistent with the result of the cluster calculation by Kamimura and Eto[8]. In the superconducting regime, on the other hand, the holes itinerate alternately from the a_{1g}^* orbital at an A-site to the b_{1g} orbital at a B-site, consistent with the experimental results of polarized X-ray absorption by Chen et al.[19].

As for superconductivity, early experimental findings such as very small isotope effects, the coexistence of superconductivity and magnetism seemed to have supported theoretical models based on non-Fermi-liquid and/or non-phononic mechanisms. [4,5,25] Recently, however, some of experimental groups have suggested the phonon-mechanism based on their experimental results, such as (1) a non-zero isotope effect such as $\alpha \sim 0.1 \sim 0.8$ depending on x in the T_c versus $M^{-\alpha}$ relation in $La_{2-x}Sr_xCuO_4$, where M is the atomic mass of oxygen[26,27,28], (2) the pronounced softening of the phonon density of states measured by the neutron time-of-flight spectroscopy[29], (3) the anomalies in certain phonon branches near the zone boundary[30], (4) the changes of Raman frequencies as well as line shapes which indicate the interaction of the Raman-active modes with underlying electronic continuum[31], and (5) the disappearance of the phonon structure

in the tunneling experiments above T_c[32,33,34,35]. In this context keen attention has been paid recently to the electron-phonon interaction of high temperature superconductor, since Kamimura et al.[36,37,38,39,40] showed that even the electron-phonon mechanism lead to the d-wave pairing in case where the local AF order exists and also since the problems of the coexistence of the spin and charge orderings related to the appearance of stripes have been actively discussed in connection with the electron-phonon interaction[41]. It is another important purpose of the present thesis to show that the present electronic structure leads to d-wave superconductivity even in the electron-phonon mechanism.

We calculate the strengths of the electron-phonon interactions for various phonon modes in $La_{2-x}Sr_xCuO_4$ and also the $\boldsymbol{k}, \boldsymbol{k}'$ dependent spectral function, using the electronic structure calculated in Chapter 4. Based on this result, we show that the electron-phonon interactions which scatter the pairs of electrons from a pair state $(\boldsymbol{k} \uparrow, -\boldsymbol{k} \downarrow)$ to a different pair state $(\boldsymbol{k}' \uparrow, -\boldsymbol{k}' \downarrow)$ are repulsive for some combinations of $\boldsymbol{k}$ and $\boldsymbol{k}'$ and attractive for other combinations, while those containing the processes of virtual emissions and absorptions of various modes of phonons by a single electron are always attractive. We show that the calculated momentum-dependent spectral function $\alpha^2 F_{\uparrow\downarrow}(\Omega, \boldsymbol{k}, \boldsymbol{k}')$ changes its sign as a function of $\boldsymbol{k}$ and $\boldsymbol{k}'$, showing the $d_{x^2-y^2}$ symmetry. Then we calculate the d-wave component of the spectral function and the transition temperature for d-wave superconductivity, T_c. The phonon-mediated d-wave superconductivity, which is consistent with experimental results such as Josephson junction π-tunneling experiments, is originated from the alternant appearance of the a_{1g}^* and the b_{1g} orbitals and the different spatial distribution of Bloch wave functions for up-spin and down-spin holes. A preliminary result of this calculation has been published elsewhere[42,36,43].

In the present thesis, first we give a brief summary of experimental results on LSCO in Chapter 2. The Chapter 3 is devoted to developing the formalism of how to calculate the effective one-electron type band structure and the effective Fermi surface including many body effect. In Chapter 4, the numerical results of the effective one-electron type band structure and the effective one-electron type wave function are presented based on

the Hamiltonian matrix formulated in Chapter 3. And, in Chapter 5, these results are applied to explain the the normal state properties of LSCO, such as the resistivity [44,45, 46,47,48,49,50], the Hall coefficient [44,45,46,51] and the electronic heat capacity[52,53]. In Chapter 6 the momentum-dependent spectral functions and the transition temperature for d-wave superconductivity are calculated by using the effective one-electron type band structure and the effective one-electron type wave functions presented in Chapter 4. We give a summary and a discussion in Chapter 7.

Chapter 2.

Brief
Summary of Experimental Information on
$La_{2-x}Sr_xCuO_4$

2-1. Crystal structure

The crystal structure of LSCO is layered perovskite with the octahedral-type Cu-O networks and is in tetragonal phase at high temperature, the unit cell of which is shown in Fig. 2. It undergoes an orthorhombic distortion near 200K, where the CuO_6 octahedra are rotated at about $2°$ in the bc-plane. However, orthorhombic distortion is small and the crystal structure of the orthorhombic phase is not significantly different from that of the tetragonal phase. Thus in the present thesis, we perform the band structure calculation and consideration for tetragonal phase. In Fig. 2 we describe the crystal structure of LSCO, where a_1, a_2 and a_3 are the lattice vectors of this system with ordinary unit cell. As seen in this figure, CuO_2 form a square network in each layer perpendicular to the c-axis (z-axis). The CuO_6 octahedra are stretched along the c-axis, then Cu-O(2) distance is 2.39Å while Cu-O(1) distance is 1.89Å. The apical oxygen, O(2), is not positioned in the La-plane and the distance between CuO_2-plane and La-plane is 1.86Å which is smaller than Cu-O(2) distance.

If we consider the antiferromagnetic system, as will be mentioned in Chapter 3, we must distinguish neighbouring Cu atoms with respect to spin orientation. Thus we have

to consider a super-unit-cell including sub-lattices consisting of two Cu atoms. In this figure a_1, a_2 and a_3' are the lattice vectors of this super-unit-cell with 14 atoms involved. In Fig. 3 the Brillouin zones of ordinary unit cell and antiferromagnetic super-unit-cell are shown.
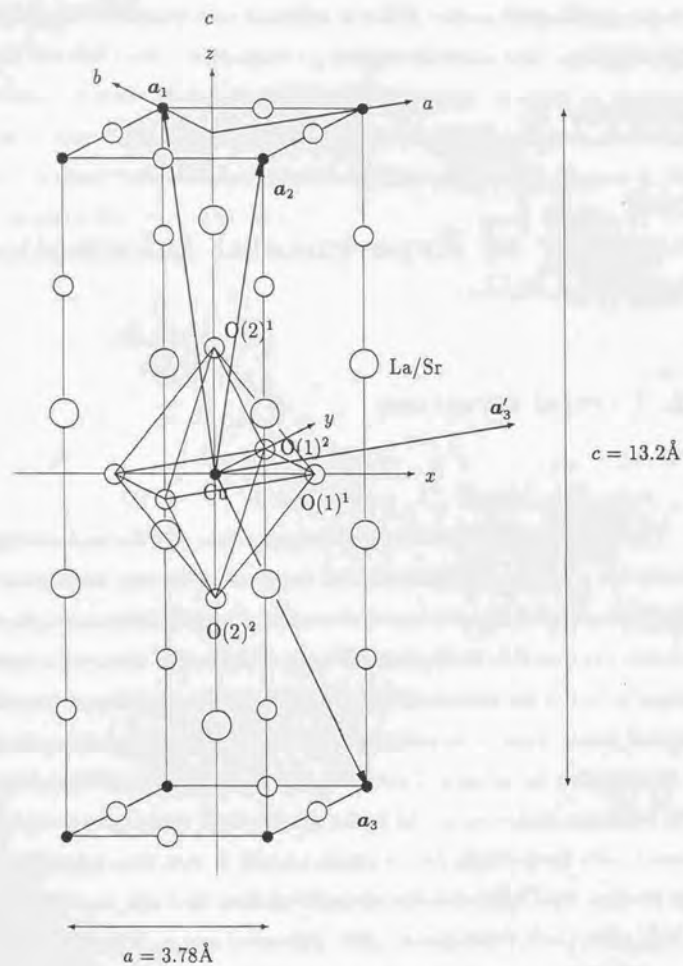
Figure 2: Crystal structure with CuO_6 octahedron in LSCO. Here a_1, a_2 and a_3 are the lattice vectors of this system with ordinary unit cell and a_1, a_2 and a_3' are the lattice vectors of AF unit cell including sub-lattices consisting of two Cu atoms.
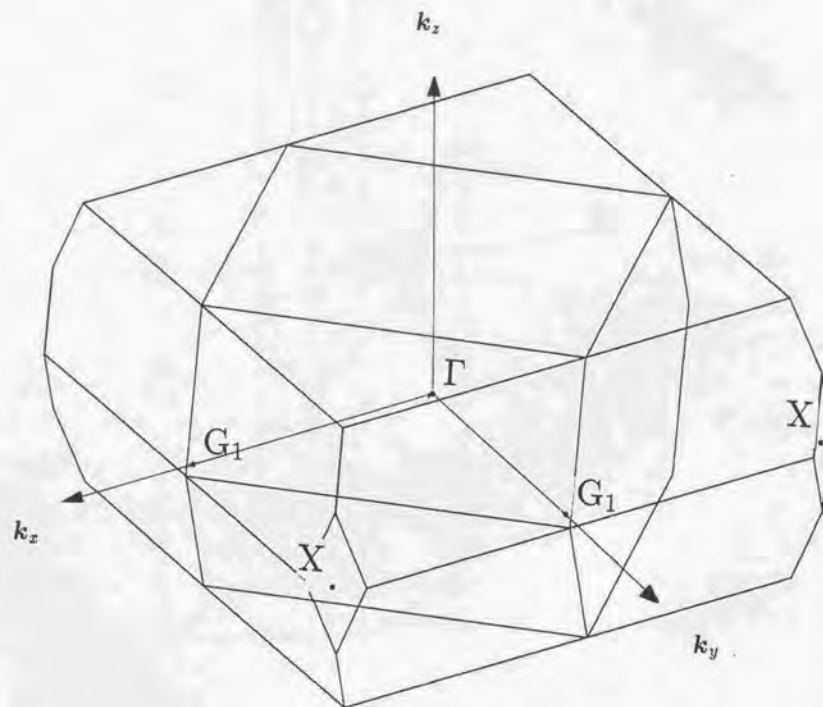
Figure 3: The Brillouin zones of ordinary unit cell and antiferromagnetic super-unit cell. One at the outermost part is the ordinary Brillouin zone and the inner part is the folded Brillouin zone for the antiferromagnetic unit cell in LSCO. Here the k_x axis is taken along $\overline{\Gamma G_1}$, corresponding to the x-axis (the Cu - O - Cu direction) in a real space.

2-2. Transport properties in normal state $La_{2-x}Sr_xCuO_4$

As well known, a parent compound of LSCO, La_2CuO_4, shows semiconducting behavior. With only one percent or less Sr doping, the resistivity drastically decreases to the order of 10^{-3}ohm-cm and T linear resistivity is observed in a wide temperature region starting just above T_c and extending to several hundreds degree[44,45,46,47,48,49,50]. Temperature dependence of the resistivity for LSCO with various Sr content observed by Takagi *et al.* is shown in Fig. 4. This linear temperature dependence of resistivity, which is a common feature of high T_c cuprates, is possibly derived from the transport relaxation time due to the hole-phonon scattering, because of a small Fermi surface calculated in Chapter 4 and a two-dimensional character of LSCO. At around $x = 0.05$ the superconductivity appears. Above $x = 0.15$, T_c decreases rapidly while the magnitude of resistivity is still decreasing.
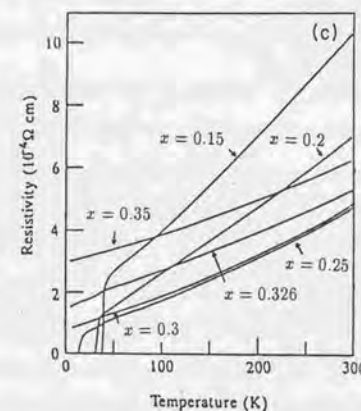
Figure 4: Temperature dependence of the resistivity for LSCO with various Sr content observed by Takagi *et al.* (see ref. [44])
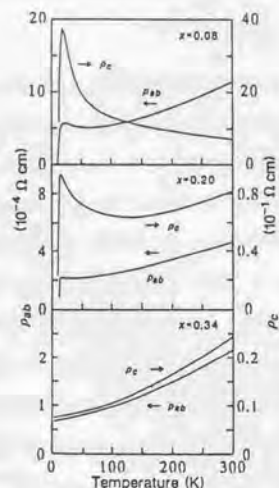
Figure 5: Temperature dependences of ρ_{ab} and ρ_c for three compositions of LSCO observed by Ito *et al.* (see ref. [54])

Figure 6: Sr content dependence of the Hall coefficient R_H for LSCO at 80K (circles) and 300K (triangles observed by Takagi *et al.* The sign of R_H is positive for $x < 0.15$ and negative for $x > 0.15$, respectively (see ref. [44])

The characteristic small deviation from linearity is observed in overdoped LSCO. The change in the resistivity slope in YBCO was measured at T^*, where a spin gap in NMR and neutron scattering appears[55]. This may be attributed to the crossing from the small Fermi surface calculated in chapter 4 to the ordinary large Fermi surface, which is due to the disappearance of the local AF order.

Transport perpendicular to the CuO_2 layers is controversial. The temperature dependence of the resistivity parallel to the c axis, ρ_c, shows non-metallic behavior even in the Sr content region where the resistivity in CuO_2 plane is metallic[54] (See Fig. 5.).

This feature is observed in many high T_c cuprates. The only exception is fully oxygenated $YBa_2Cu_3O_7$ with $T_c \sim 90K$, which shows metallic-like temperature behavior, with the mean-free path comparable or slightly less than the inter-plane distance. However, in most superconducting compounds it is non-metallic. Thermally activated transport parallel to c-axis seems to suggest the localization of carriers in a CuO_2 plane. Based on the electron and spin structure calculated in chapter 4, the two dimensional localization of holes may be explained by assuming that the local AF order is restricted in a CuO_2 plane and holes have to be localized in a CuO_2 plane in order that the holes with up-spin itinerate alternately from the a_{1g}^* orbital in a CuO_6 cluster with localized up-spin (A-site) to the b_{1g} orbital in a CuO_6 cluster with localized down-spin (B-site).

The positive Hall coefficient decreases almost in proportion to the inverse of the

14

15

Sr concentration, $1/x$, in the low concentration region[44,45,46,51] (See Fig. 6). It is a strange character if one assumes a large Fermi surface, while it is a natural consequence of a small Fermi surface calculated in Chapter 4. With further doping , the Hall coefficient decreases more rapidly than expected from Mott-Hubbard picture and changes its sign from positive to negative at $x \sim 0.3$. The Hall coefficient shows negative temperature dependence in spite of the metallic resistivity in the superconducting concentration region. In Chapter 5 we will calculate the Hall coefficient based on the electronic structure derived in Chapter 4, and show that the x- and T-dependences of Hall coefficient come from the characteristic features of the present electronic structure (See Chapter 4) such as the occurrence of a sharp peak in density of states and the drastic change of the shape of Fermi surfaces, which is hole-like at E_F corresponding to low Sr content while electron-like at E_F corresponding to well over-doped region.

However de Haas-van Alphen measurement is not yet carried out in LSCO, Kido et $al.$[56] have carried out the de Haas-van Alphen measurement on $YBa_2Cu_3O_7$ and found a broad band centering at 540T, which suggests the existence of a small Fermi surface.

2-3. Thermal Properties in Normal State $La_{2-x}Sr_xCuO_4$

Thermoelectric power S is large, positive, and temperature-independent in parent compound La_2CuO_4[57,58,59] (See Fig. 7). In the doped LSCO, thermoelectric power is reduced and weakly temperature dependent. The large value and the weak temperature dependence of the thermoelectric power are observed in many under-doped high T_c cuprates.
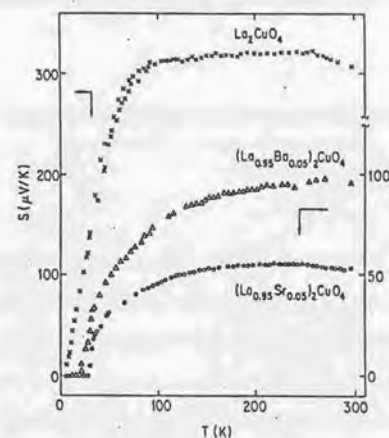
Figure 7: Temperature dependence of thermoelectric power $S(T)$ relative to gold for pure La_2CuO_4 and two lower concentration alloys observed by Cooper et $al.$ (see ref. [57])
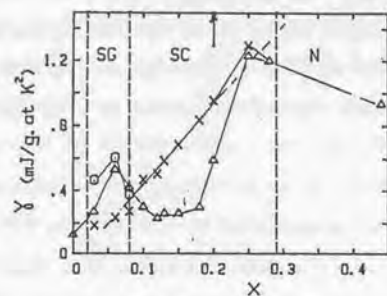
Figure 8: The coefficient of electronic specific heat in LSCO, γ, observed by Loram *et al.* (see ref. [60])

As for heat capacity, Loram *et al.* presented a detailed investigation of the specific heat of LSCO[60] (See Fig. 8). They observed the difference in specific heat between the each sample and the parent compound using a differential calorimeter, and then correlated the anomaly at T_c to give the normal state electronic term γ_n. They observed the non-zero normal state electronic term γ_n in the superconducting concentration region ($0.05 < x < 0.25$), and showed the existence of large density of state at Fermi energy, consistent with the angle-resolved photoemission data[61,62]. The density of states obtained from the experimental result of normal state electronic term γ_n is consistent with that calculated in Chapter 4. (See Chapter 5)

18

2-4. Optical Properties in Normal State $La_{2-x}Sr_xCuO_4$

Infrared absorption and reflection measurements provide an insight into the nature of charge carriers and their interaction with the lattice. Uchida *et al.* obtained the optical conductivity spectra $\sigma(\omega)$ from the Kramers-Kronig transformation of the reflectivity spectrum[63,64] (See Fig. 9). The spectrum of the parent compound La_2CuO_4 is dominated by the optical phonons in the far-infrared region and the CT excitation peaked at $\sim$ 2eV. For low-doping LSCO, $\sigma(\omega)$ seems to consist of two components, a narrow Drude-like peak at $\omega \sim 0$ and a broad band centered in the mid-IR region. It may be possible to regard the former as coherent motion of doped holes as is expected in the electronic structure calculated in chapter 4. As doping proceeds, the intensity of the Drude peak increases and the mid-IR peak shifts toward zero-frequency.
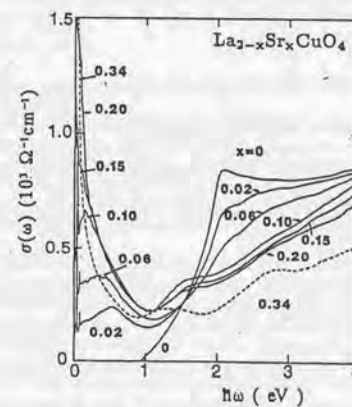
Figure 9: Evolution of optical conductivity with doping in LSCO observed by Uchida *et al.* (see ref. [63])

19
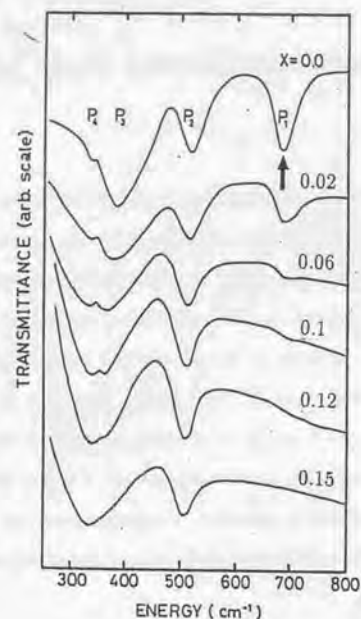
Figure 10: Infrared spectra for LSCO observed by Ohbayashi *et al.* (see ref. [65])

Figure 11: Valence-band photoemission spectra of LSCO and $Bi_2Sr_2CaCu_2O_8$ observed by Fujimori *et al.* (see ref. [67])

Relevant optical excitations are not seen in the spectrum with the polarization perpendicular to the CuO_2 plane, consistent with the the data of c-axis resistivity[54] which is larger by orders of magnitude than the ab plane resistivity and shows a non-metallic temperature dependence. This is an indication of confinement of the dopant hole within the CuO_2 plane.

Ohbayashi *et al.*[65,66] observed an anomalous behavior of the infrared active mode at about 680 cm^{-1} (E_u mode) in LSCO, which is observed commonly in high T_c cuprate. However the peak at about 680 cm^{-1} indicated by an arrow in Fig. 10 is clearly observed for La_2CuO_4, its intensity decreases with increase of the Sr concentration x and it is almost invisible for $x \geq 0.1$. This clear correlation of infrared anomaly with appearance of superconductivity seems to provide direct evidence of the importance of electron-phonon

interaction in copper oxides.

Important information on the electronic structure of the copper oxides has been obtained from the high-energy spectroscopic studies such as photoemission, inverse photoemission (BIS), and X-ray absorption spectroscopy (XAS). The combination of photoemission and inverse photoemission spectra clearly shows the existence of a finite density of states at the Fermi level, which supports the electronic structure calculated in chapter 4. Fujimori [67,68] has observed, in $Bi_2Sr_2Ca_{1-x}Y_xCu_2O_8$, that the Fermi energy is located at the top of the valence band as is expected. While, the E_F is found to be near the center of the band gap in LSCO, which seems to be due to the existence of smaller indirect band gap.
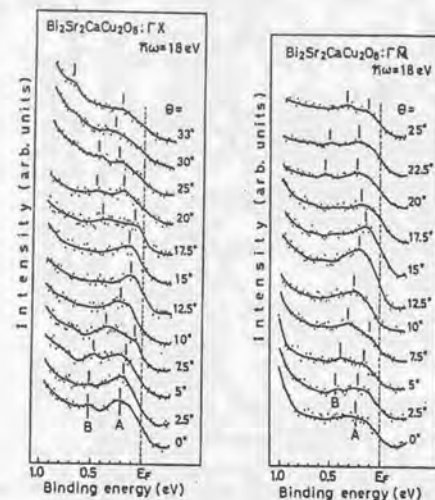
Figure 12: Angle-resolved photoemission spectra near the Fermi level measured with the photon energy of 18eV for two high symmetry direction in the Brillouin zone, by Takahashi. (see ref. [61])

Figure 13: Fluorescence yield photoabsorption spectra for $E_h\|c$ and $E_h\perp c$ as a function of Sr content observed by Chen *et al.* (a) Low-energy region of the O K-edge absorption; (b) the L_3 white line region of the Cu L-edge absorption. (see ref. [19])

Fujimori observed valence-band photoemission spectra of $La_{1.92}Sr_{0.08}CuO_4$[67] (See Fig. 11). He finds that the parent compounds of the copper-oxide superconductors prove to be charge-transfer insulators, in which the band gap is of the oxygen p-to-Cu d charge transfer type, and that an extra hole in LSCO is more than 90% oxygen p-like.

Angle-resolved photoemission spectroscopy is a very powerful experimental method to study the energy band structure in a crystal. Takahashi *et al.* observed two dispersive bands which cross the Fermi level midway between Γ-point and the zone boundary in $Bi_2Sr_2Ca_{1-x}Y_xCu_2O_8$[61], consistent with the result obtained from combination of photoemission and inverse photoemission spectra. (See Fig. 12)

Polarized X-ray absorption spectroscopy provides a direct information on the nature and the symmetry of the unoccupied electronic state above Fermi level. Recently Chen *et al.*[19] (See Fig. 13) performed polarization-dependent X-ray absorption measurements for O K- and Cu L-edges in LSCO. In a shoulder area of the doping-independent Cu L_3 line, they observed the doping-induced satellite peak (L_3') for both polarization of $E\perp c$ and $E\|c$. According to Kamimura, Ohura, Eto and Chen[21,70], the appearance of the doping-induced satellite peak for both polarization *at the same energy* has suggested that a state of dopant holes must consist of high-spin and low-spin states, since the polarization $E\perp c$ and $E\|c$ detect low-spin and high-spin states respectively. This is the basis of the present calculation of electronic structure given in Chapter 4.

22

23
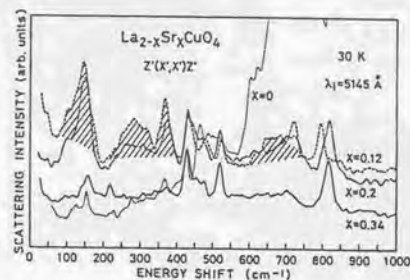
Figure 14: Resonant Raman spectra of $YBa_2Cu_3O_6$ showing Raman forbidden, infrared active LO modes (wavy arrows). (see ref. [71])

The Raman scattering spectra give the evidence of strong electron-phonon interactions. Cardona *et al.*[71,72] observed Raman forbidden, infrared active modes in resonant Raman spectrum (See Fig. 14). The peaks of infrared active B_{2u} modes are at 145, 282, 367, 670 cm^{-1}, for LSCO with superconductor composition[73;74]. The appearance of the infrared active modes in the Ramam spectra indicates the loss of inversion symmetry caused by the local distortion.

2-5. Magnetic Properties in Normal State LSCO

The parent material La_2CuO_4 is an antiferromagnet with T_N=240K and the peak in the temperature dependence of the susceptibility appears near 240K[44]. The peak disappears with doping, indicating the suppression of the antiferromagnetic order above the well-over-doped region. The susceptibility increases with increasing temperature for LSCO with low Sr content. For higher doping, a broad peak in temperature dependence appears. This broad peak disappears and the susceptibility decrease monotonously with
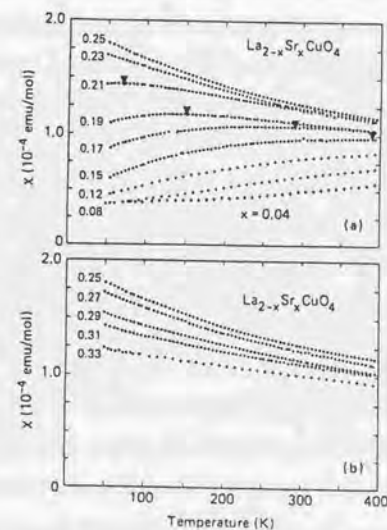
Figure 15: Normal-state magnetic susceptibility of LSCO observed by Torrance *et al.* (see ref. [47])
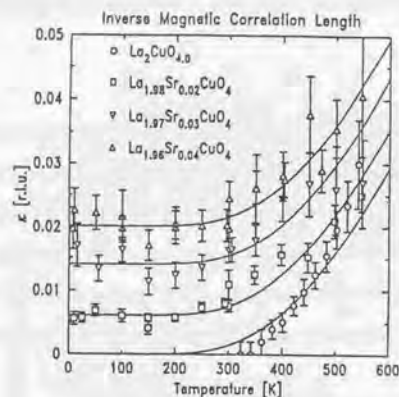
Figure 16: Doping dependence of the wave vector for the spin correlations in LSCO observed by Endoh *et al.* (see ref. [76])

increasing temperature, in over-doped region. As for the x dependence, the low temperature susceptibility increases with increasing x for $0.04 \leq x \leq 0.25$, and decreases for $0.25 \leq x \leq 0.33$[47] (See Fig. 15). This x-dependence of the susceptibility coincides fairly well with the 'Pauli-para' spin susceptibility of dopant holes calculated by using the effective one electron type conduction band in Chapter 4. However 'Pauli-para' spin susceptibility is small at small Sr content region compared with experimental data, Matsuno and Kamimura[75] argue that the difference is due to the strong suppression of 'Pauli-para' spin susceptibility by the interplay between the nature of the spin-fixed energy band derived in Chapter 4 and the electron-electron interaction.

Neutron inelastic scattering experiment is very powerful , because it can give us its magnetic excitation spectra at any fixed point of momentum and energy space. The spatial extent or correlation length ζ of the spins within the CuO_2 plane can also be obtained from neutron inelastic scattering experiment[76,77] (See Fig. 16). The thermal

evolution of the inverse correlation length, $\kappa = \zeta^{-1}$, established the magnetic roll of the hole doping, which frustrates the antiferromagnetic squared lattice. The observed κ is the sum of κ_0 and $\kappa(T)$, where the former, κ_0, is temperature invariant, determined by the Sr content x and proportional to the average hole pair distance, *i.e.* $\zeta/a = 1/\sqrt{x}$, and the latter, $\kappa(T)$, is just the thermal evolution for the undoped crystal La_2CuO_4. The survival of local AF order of localized spin also supports the present electron and spin structure characterized by the alternant appearance of $^1A_{1g}$ and $^3B_{1g}$ multiplets.

Another important aspect of neutron scattering in LSCO is the appearance of the incommensurate peak[76,78]. Possible interpretation of the incommensurate peak is given in Chapter 4. The incommensurability or the shift of the wave vector, Δq, apparently develops with the appearance of the superconductivity and shows the nonlinear x-dependence.

For YBCO, a gap-like structure develops at low temperatures as was first reported by Grenoble group[79,80]. Spin gap $E_G = 0.028eV$ is observed below and above T_c in YBCO with unpolarized neutron scattering. Spin gap seems to be a natural consequence of the present electronic structure calculated in chapter 4. The AF magnon energy is the minimum at Γ-point in the Brillouin zone which corresponds to $(0,0,0)$. When k vector changes directly from Γ to Δ point which corresponds to $(\pi/2a, \pi/2a, 0)$, the magnon energy increases monotonously. Let us introduce the coherence length λ_s which represents the scale of local AF correlation region. Then, for the case of local AF order, the magnon energy is meaningful only when k vector lies outside a radius $2\pi/\lambda_s$ around the Γ point. Consequently the spin gap, *i.e.* a minimum energy to flip a direction of single spin in the local AF order, is to be observed.
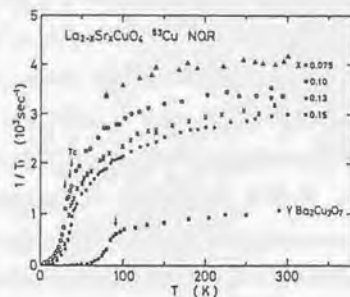
Figure 17: Temperature dependence of $1/T_1$ ($=2W$) of ^{63}Cu observed by Kitaoka *et al.* (see ref. [81])

NMR studies are playing an important role in clarifying separately the electronic stat of oxygen site and that of copper site in the CuO_2 plane. The main features of nuclear spin relaxation rate in LSCO, as well as in other high T_c cuprates, are the absence of the Hebel-Slichter coherent peak below T_c and the temperature dependent Korringa ratio $1/TT_1$ above T_c[81] (See Fig. 17). The deviation from Korringa low of ^{63}Cu spin relaxation rate reveals the anomalous enhancement due to the AF fluctuation of the localized spin of Cu, showing that the AF spin correlation is significantly developed in low concentration region as clarified by the neutron scattering experiment. The fact that $1/T_1$ decreases markedly without a coherence peak just below T_c, has been interpreted in terms of d-wave superconductivity model[82].

2-6. Anomalies in $La_{1.875}M_{0.125}CuO_4$

In $La_{1.875}Ba_{0.125}CuO_4$ (LBCO), curious disappearance of bulk superconductivity in a narrow range of x near 0.125 is observed[83,84,85] (See Fig. 18). Suppression of T_c is also reported in the same concentration range for LSCO, but the degree of the suppression is small compared with LBCO. These anomalies are accompanied with the structural transition from the mid-temperature orthorhombic (OMT) phase to the low-temperature tetragonal (TLT) phase at temperature $T_{d2} \sim 60K$. The structure of TLT phase is different from that of a high temperature tetragonal (THT) phase which appears at higher temperature than $T_{d1} \sim 200K$ in $La_{1.875}Ba_{0.125}CuO_4$.
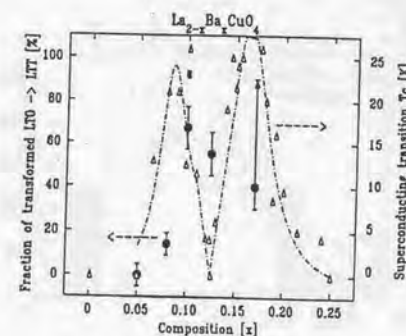
Figure 18: Transition temperature T_c (triangles) and the fraction of TLT phase present in low-temperature observed by Axe *et al.*, where circles and rectangles reveal X-ray and neutron data respectively. (see ref. [83])

In the TLT phase the electrical conductivity becomes non-metallic and the density of states reduces, which is suggested by the enhancement of thermal-conductivity and the linear coefficient of the specific heat. Investigation through the partial substitution of Ni, Zn and Ga for Cu [86] shows that this low temperature structural phase transition originates from electronic instability related to the hole concentration of $x = 0.125$ rather than from something based on the Ba concentration. And it is consistent with the interpretation based on the electronic structure calculated in chapter 4.

2-7. Superconducting Properties of $La_{2-x}Sr_xCuO_4$

As is well known, superconductivity in LSCO appears at $x \sim 0.05$ and the transition temperature T_c increases for $0.05 \leq x \leq 0.15$ (under-doped region) then it decreases[44] (See Fig. 19).

A number of tunneling spectroscopy experiments have been performed for $Bi_2Sr_2CaCu_2O_y$. Kitazawa *et al.* have proved that the surface BiO layer is essentially semiconductive with a certain energy gap in room temperature[87], by performing scanning tunneling spectroscopy (STS) which can probe the local density of states specific to each atomic site or atomic layer. It strongly supports the two-dimensional conduction in the CuO_2 network.
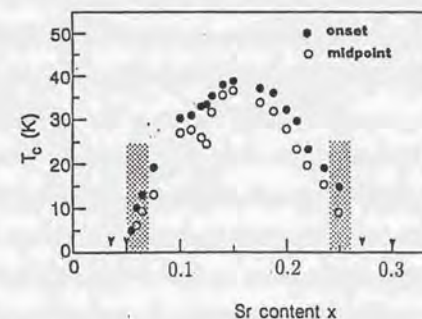
Figure 19: Sr content dependence of the superconducting transition temperature T_c for LSCO observed by Takagi *et al.* (see ref. [44])

Miyakawa *et al.*[33,34,35,32] observed phonon structures on tunneling conductance spectrum, suggesting the superconductivity mediated by phonons. As for LSCO Ekino *et al.*[88] observed the well distinguished phonon structures in the superconducting $La_{1.85}Sr_{0.15}CuO_4$ which correspond to the generalized neutron phonon density of states, suggesting the phonon mechanism of superconductivity[88]. As for the energy gap, the data of tunneling spectroscopy is still controversial. The obtained values of $2\Delta/k_BT_c$ are scattered from $5 \sim 6$[88] to 9[87].

The previously observed small oxygen isotope effect or the absence of it in various high T_c cuprates[89,90,91] has been considered as an important evidence for non-phononic superconductivity. However, the oxygen isotope effect has been reported for LSCO. Particularly the value of α in the relation of $T_c \sim M^{-\alpha}$ varies in the region of $0.1 \sim 0.8$, depending strongly on the hole concentration x, with the maximum α values (~ 0.8) found for x near 0.12[92].

Recently keen attention has been paid to the symmetry of superconducting gap, *i.e* whether it is s wave-, or extended s wave-, or d wave-symmetry. Several phase-sensitive experiments have supported d wave-symmetry for $YBa_2Cu_3O_7$ (YBCO). Recently the d-wave symmetry for YBCO was established by several new pairing symmetry experiments, for examples, tricrystal ring experiment based on macroscopic coherence effect[93,94].

Chapter 3.

Formalism of How to Calculate the Electronic Structure of $La_{2-x}Sr_xCuO_4$

3-1. Introduction

In the copper oxides, there exist areas in each CuO_2 layer in which the localized spins form an antiferromagnetic (AF) short range ordering[76,77]. Here we call these areas "spin-correlated regions". The size of each spin-correlated region is characterized by the spin correlation length. Then, following the results of Kamimura and Eto, a dopant hole with up-spin in the spin-correlated region occupies an a_{1g}^* orbital which consists of a Cu d_{z^2} orbital and the in-plane oxygen p_σ and apical oxygen p_z orbitals, at a CuO_6 octahedron with localized up-spins, forming the Hund's coupling triplet state, $^3B_{1g}$, while it occupies a bonding b_{1g} orbital which consists of the in-plane oxygen p_σ orbitals and a Cu $d_{x^2-y^2}$ orbital at a CuO_6 octahedron with a localized down-spin, forming the Zhang-Rice spin-singlet state[95], $^1A_{1g}$.

As a result the dopant holes move resonantly from a CuO_6 octahedron to a neighboring CuO_6 octahedron in a CuO_2 layer by a transfer interaction of about 0.3eV. Such coherent motion of dopant holes is possible when the spin correlation length is much larger than the distance between neighboring copper sites, and the magnitudes of transfer interactions between neighboring CuO_6 cluster are larger than the energy difference between $^1A_{1g}$ and $^3B_{1g}$ multiplets. As a result an exotic metallic state is created for LSCO with hole concentration, $x \leq 0.2$.

It is now well established that the parent compounds of high T_c cuprates are charge-transfer insulators, in which the states near band gaps are of the ligand p-to-metal d

charge-transfer type[69]. Then the dopant holes have mainly Op_σ character, while the localized spins have mainly Cu $d_{x^2-y^2}$ character. In other word it is necessary to take at least two bands, one for localized spins and one for dopant holes, in order to construct an appropriate model for high T_c cuprates. In the present treatment the band for the localized spins consists of a b^*_{1g} orbital and that for dopant holes consists of b_{1g} and a^*_{1g} orbitals. And the upper Hubbard b^*_{1g} band is fully occupied by holes and the lower Hubbard b^*_{1g} band is empty even in the doped LSCO as well as the undoped La_2CuO_4. Here 'upper' (or 'lower') means that the electron energy of the Hubbard band is higher (or lower).

In order to solve the Hamiltonian (1.1) we first separate a system of the localized spins which occupy the upper Hubbard b^*_{1g} band and form the antiferromagnetic ordering due to the superexchange interaction between the localized spins, J in Eq.(1.1), from a hole carrier system. Then we treat the the exchange interaction between the spins of a dopant hole and a localized spin in Eq.(1.1), $\sum_{i,m} K_m s_{im} \cdot S_i$, in the mean field approximation by replacing S_i by its average value $\langle S_i \rangle$. In the present treatment the values at $T = 0K$ are taken as the average values of $\langle S_i \rangle$, that is $+1$ for A-site and -1 for B-site. Thus the effect of the localized spins is dealt with like a molecular field acting on a dopant hole.

In order to derive the effective one-electron-type Hamiltonian for the dopant holes, we determine the 'molecular field' of the localized spins so as to reproduce the first principles calculation for a CuO_6 octahedron by Kamimura and Eto[8]. In doing so, we determine the effective-one-electron type Hamiltonian in a periodic system so that the energy of $^3B_{1g}$ and $^1A_{1g}$ multiplet states calculated by using the effective one-electron-type Hamiltonian coincides with that of first principles calculation by Kamimura and Eto, and further assumed that the lifetime broadening effect due to the finite spin correlation length is neglected.

In this context the calculation of the effective one-electron-type band structure of the carrier system is performed by renormalizing the effects of the the exchange integral between the spins of a dopant hole and a localized spin into the carrier states. In doing

so we first note that the holes which are accommodated in the antibonding b^*_{1g} orbitals are localized at Cu site by the strong U effect and the spins of localized holes in b^*_{1g} orbitals are coupled antiferromagnetically due to the superexchange interaction between the localized spins, J in Eq.(1.1). Since the dopant holes move coherently over a long distance, alternating from the high-spin $^3B_{1g}$ multiplet to the low-spin $^1A_{1g}$ multiplet and then to the high-spin $^3B_{1g}$ multiplet in the 'molecular field' of the localized spins, we take a unit cell so as to contain two neighboring CuO_6 octahedra with up- and down-localized spins called A- and B-sites. And in order to realize the alternant appearance of b_{1g} and a^*_{1g} orbitals through O p_σ orbitals, we take into account the CuO_2 network structure explicitly and consider the 34×34 dimensional matrix ($\tilde{H}(k)$), where $2p_x$, $2p_y$ and $2p_z$ atomic orbitals for each of eight oxygen atoms and $3d_{yz}$, $3d_{zx}$, $3d_{xy}$, $3d_{x^2-y^2}$ and $3d_{z^2}$ atomic orbitals for each of two Cu atoms in the unit cell are taken as the basis functions. This Hamiltonian matrix $\tilde{H}(k)$ consists of two parts; the one-electron part $\tilde{H}_0(k)$, and the effective interaction part $\tilde{H}_{int}(k)$ which comprises the many-body interactions such as the exchange interaction between carriers and localized spins in Eq.(1.1) and Hubbard U interaction for the localized holes in b^*_{1g} orbitals.

Then, in the case of a dopant hole with up-spin, the energy of b^*_{1g} state in a CuO_6 cluster with localized up-spin (A-site) is taken to be so high that the b^*_{1g} state at A-site is filled with holes even in undoped La_2CuO_4, while that in a CuO_6 cluster with localized down-spin (B-site) is so low that the b^*_{1g} state at B-site is empty. The difference between the energy of b^*_{1g} states at A-site and B-site is due to the strong U effect. Further the energy of a^*_{1g} state at A-site is taken to be higher than that at B-site by Hund's coupling energy, while the energy of b_{1g} state at B-site is taken to be higher than that at A-site by the spin-singlet coupling in $^1A_{1g}$ state, so as to reproduce the characteristic electronic structure where up-spin carriers take the $^3B_{1g}$ state at A-site and the $^1A_{1g}$ state at B-site. In this chapter the energy of b^*_{1g}, b_{1g} or a^*_{1g} state indicates the energy for a electron but not a hole.

In this way we can include the many-body interaction effects of the Hubbard U interaction for the localized holes in b^*_{1g} orbital as well as of the exchange interaction

in Hamiltonian (1.1) in the the 34×34 dimensional effective interaction part $\tilde{H}_{int}(\boldsymbol{k})$. Further all the matrix elements related to the transfer interactions which appear in the one-electron part of the 34×34 dimensional Hamiltonian matrix, $\tilde{H}_0(\boldsymbol{k})$, can be estimated from the Slater-Koster (SK) parameters. In the present calculation we have used the values of the SK parameters fitted to an APW band calculation[96] by DeWeert $et\ al.$[97] and thus the one-electron part of the Hamiltonian, $\tilde{H}_0(\boldsymbol{k})$, reproduces the APW bands well.

In order to obtain $\tilde{H}_{int}(\boldsymbol{k})$, we first construct the eigenstates localized at A-site or B-site by taking the linear combination of the doubly degenerated eigenstates of $\tilde{H}_0(\boldsymbol{k}_0)$, where vector $\boldsymbol{k}_0$ indicates $(\frac{\pi}{2a}, \frac{\pi}{2a}, 0)$. The resultant eigenstates are $\sum_l \cos(\frac{\pi}{2a}x_l + \frac{\pi}{2a}y_l)\varphi_{al}$ and $\sum_l \sin(\frac{\pi}{2a}x_l + \frac{\pi}{2a}y_l)\varphi_{al}$, which we regard to be localized at A-site and B-site respectively, where φ_{al} are the Wannier type eigenstates of $\tilde{H}_0(\boldsymbol{k}_0)$.

If we take these functions as a basis function, the effective interaction part $\tilde{H}_{int}(\boldsymbol{k})$ is obtained, by setting the energy of the b_{1g}^* state at A-site, that of b_{1g}^* state at B-site, that of b_{1g} state at B-site, that of a_{1g}^* state at A-site and that of a_{1g}^* state at B-site so as to reproduce the energy difference between multiplet $^3B_{1g}$ and $^1A_{1g}$ calculated by Kamimura and Eto[8]. Then by a unitary transformation we can obtain the expression of $\tilde{H}_{int}(\boldsymbol{k}_0)$ with the ordinary basis of Wannier type atomic functions.

The method described above is similar in its idea to the (LDA+U) method developed by Anisimov $et\ al.$[98] for copper oxides, but the interactions are treated more accurately in the present method. As described above, all the matrix elements in the 34×34 dimensional Hamiltonian matrix ($\tilde{H}$) become one-electron type, and thus we can diagonalize it easily. In this way we can obtain a band structure including the many-body effects in a molecular field approximation for LSCO. The obtained band structure for up-spin dopant holes is shown in Fig, 20 in Chapter 4, where the Brillouin zone is also shown in the inset. The same shape of the band structure is also obtained for down-spin dopant holes. Here one should note that the Hubbard bands for localized b_{1g}^* holes are removed from the band structure in Fig. 20. In un-doped La_2CuO_4 all the bands except for upper Hubbard b_{1g}^* band are occupied by electrons and the localized b_{1g}^* holes have mainly Cu

d character, while the dopant holes have mainly O p_σ character. Thus the present theory shows definitely that La_2CuO_4 is a charge transfer type insulator, consistent with the experimental result.[44].

3-2. Slater-Koster Method

The Slater-Koster method, in which the analytical form of the tight binding (TB) Hamiltonian is fitted to the first principle band calculation, can be used to give insight into difficult problems which are intractable with a standard first principle calculation method. Therefore, it has been used to consider the structural phase transition associated with a charge density wave[99], the phonon spectra and the electron-phonon mediated superconductivity in high T_c cuprates[100,101] etc.. In the present paper we use the Slater-Koster method as a starting point for a many-body calculation of the electronic structure of LSCO. The Slater-Koster (SK) method was applied to LSCO by DeWeert *et al.*[97]. They determined the on-site elements and the overlap integrals so as to fit the analytical form of the tight binding Hamiltonian to the first principle APW calculation. They performed the augmented-plane-wave (APW) calculation to generate the eigenvalues $E_n(\boldsymbol{k})$ and the angular momentum components, $Q_{nlm}(\boldsymbol{k})$ which mean the fraction of electronic charge in the n-th band for the l-th angular momentum component of the m-th basis atom. In the Slater-Koster fits they identify the angular momentum components as the squares of the norms of the coefficients of TB wave functions in terms of atomic-like orbitals. In order to generate the TB band with a proper angular momentum character, they minimize the functional $F = \sum_{\boldsymbol{k},n}[f_n(\boldsymbol{k})]^2$, where

$$f_n(\boldsymbol{k}) = \left| E_n^{\mathrm{APW}}(\boldsymbol{k}) - E_n^{\mathrm{SK}}(\boldsymbol{k}) \right| + \sum_{lm} \left| Q_{nlm}^{\mathrm{APW}}(\boldsymbol{k}) - Q_{nlm}^{\mathrm{SK}}(\boldsymbol{k}) \right| / W$$

where the superscripts APW and SK denotes the first principle calculated values and the Slater-Koster values, respectively, and W is a weight used to adjust the relative importance of $E_n(\boldsymbol{k})$ and $Q_{nlm}(\boldsymbol{k})$ in their fit. Thus the SK method affords a basis for a 'tight binding' Hamiltonian as a starting point for many-body calculations. In this section we will give a formalism of a 'tight binding' Hamiltonian for the undistorted crystal structure by using the Slater-Koster parameters.

In the tight-binding model, the Bloch functions are constructed from the atomic orbitals $\varphi_a(\boldsymbol{r} - \boldsymbol{R}_{l\mu})$ as

$$\Phi_{\mu a \boldsymbol{k}}^0(\boldsymbol{r}) = \frac{1}{\sqrt{N}} \sum_l e^{i\boldsymbol{k}\cdot\boldsymbol{R}_{l\mu}} \varphi_a(\boldsymbol{r} - \boldsymbol{R}_{l\mu}), \tag{3.1}$$

where $\boldsymbol{R}_{l\mu} = \boldsymbol{R}_l + \boldsymbol{\tau}_\mu$ represents the position of the μth ion in the lth unit cell, $\boldsymbol{\tau}_\mu$ the position of the μth ion in the unit cell, N the total number of unit cells in the crystal, $\boldsymbol{k}$ a wave vector and a specifies an orbital.

Neglecting the overlap integrals, the energy eigenvalues and the wave functions are obtained by solving the following equation,

$$\mathrm{Det} |\tilde{H}_0(\boldsymbol{k}) - E_{n\boldsymbol{k}}^0 \tilde{1}| = 0, \tag{3.2}$$

where $\tilde{H}_0(\boldsymbol{k})$ is the Hamiltonian matrix and $\tilde{1}$ the unit matrix. The energy eigenvalues $E_{n\boldsymbol{k}}^0$ and the wave functions $\Psi_{n\boldsymbol{k}}^0(\boldsymbol{r})$ are represented by using the transformation matrix $\tilde{U}$

$$\tilde{E}_0(\boldsymbol{k}) = \tilde{U}^{-1}(\boldsymbol{k}) \tilde{H}_0(\boldsymbol{k}) \tilde{U}(\boldsymbol{k}) \tag{3.3}$$

$$\Psi_{n\boldsymbol{k}}^0(\boldsymbol{r}) = \sum_{\mu a} U_{\mu a,n}(\boldsymbol{k}) \Phi_{\mu a \boldsymbol{k}}^0(\boldsymbol{r}), \tag{3.4}$$

where $\tilde{E}_0(\boldsymbol{k}) = E_{n\boldsymbol{k}}^0 \tilde{1}$. The matrix elements of the Hamiltonian $\tilde{H}_0(\boldsymbol{k})$ is defined by

$$H_{\mu a \nu b}^0(\boldsymbol{k}) = \langle \Phi_{\mu a \boldsymbol{k}}^0 | \mathcal{H}_e | \Phi_{\nu b \boldsymbol{k}}^0 \rangle, \tag{3.5}$$

where $\mathcal{H}_e$ represents the one-electron Hamiltonian which is regarded to include a part of electron correlation because the Slater-Koster (SK) parameters are determined so as to reproduce the electronic energy and the wave functions of first principle band calculation. This Hamiltonian matrix $\tilde{H}_0(\boldsymbol{k})$ is expressed by taking the atomic orbitals as bases in the following way,

$$H_{\mu a \nu b}^0(\boldsymbol{k}) = \sum_{l-l'} e^{-i\boldsymbol{k}\cdot(\boldsymbol{R}_{l\mu} - \boldsymbol{R}_{l'\nu})} H_{l\mu a l'\nu b}^0 \tag{3.6}$$

where

$$H_{l\mu a l'\nu b}^0 = \langle \varphi_a(\boldsymbol{r} - \boldsymbol{R}_{l\mu}) | \mathcal{H}_e | \varphi_b(\boldsymbol{r} - \boldsymbol{R}_{l'\nu}) \rangle \tag{3.7}$$

Further all the matrix elements related to the transfer interactions which appear in the Hamiltonian matrix $(\tilde{H}_0(\boldsymbol{k}))$ are expressed in terms of the SK parameters which represent the transfer integrals between two atomic orbitals, c_m at the origin and c'_m at an arbitrary position $\boldsymbol{R}$, where c and c' represent s, p and d, and m denotes the magnetic quantum number of the orbital angular momentum with respect to the direction of $\boldsymbol{R}$. The SK parameters are conventionally symbolized as $t(cc'\sigma)$, $t(cc'\pi)$ and $t(cc'\delta)$ corresponding to $m = 0$, ± 1 and ± 2, respectively.

In the present paper we restrict the basis functions to include $2p_x$, $2p_y$ and $2p_z$ atomic orbitals for each oxygen atom and $3d_{yz}$, $3d_{xz}$, $3d_{xy}$, $3d_{x^2-y^2}$ and $3d_{z^2}$ atomic orbitals for each Cu atom in the unit cell. Then the Hamiltonian matrix is expressed by 17 SK parameters if we consider only first neighbor interactions. They are listed in Table 1. In this table, for instance, $t(dd\sigma)$ represents the transfer integrals between two neighbouring Cu d orbitals with the magnetic quantum number $m = 0$ of the orbital angular momentum with respect to the Cu-Cu direction. The Hamiltonian matrix is shown in Table 2, and the expressions of its matrix elements are given in Appendix A.

Table 1

Table 2

on-site parameters

O(1) :in plane	E_p^1
O(2) :apical	E_p^2
Cu	$E_{d_{xy}}$
	$E_{d_{x^2-y^2}} = E_{d_{z^2}}$

first-neighbor parameters

Cu-Cu	$t(dd\sigma)$
	$t(dd\pi)$
	$t(dd\delta)$
Cu-O(1)	$t_1(dp\sigma)$
	$t_1(dp\pi)$
Cu-O(2)	$t_2(dp\sigma)$
	$t_2(dp\pi)$
O(1)-O(1)	$t_1(pp\sigma)$
	$t_1(pp\pi)$
O(1)-O(2)	$t_2(pp\sigma)$
	$t_2(pp\pi)$
O(2)-O(2)	$t_3(pp\sigma)$
	$t_3(pp\pi)$
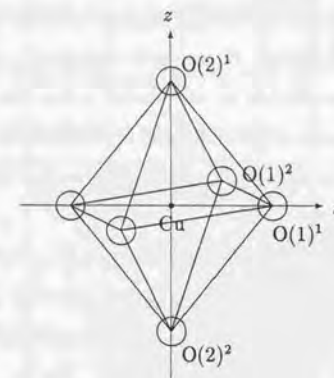
Table 1 : Slater-Koster parameters

Table 2: Matrix elements of $\tilde{H}^0(k)$

		Cu					O(2)²			O(2)¹			O(1)²			O(1)¹		
		z^2	x^2-y^2	zx	yz	xy	z	y	x	z	y	x	z	y	x	z	y	x
O(1)¹	x	T_{14}	T_{13}	0	0	0	T^*_5	0	T^*_4	T_5	0	T_4	0	T_2	T_1	0	0	E_1
	y	0	0	T_{15}	0	T_{15}	0	T^*_6	0	0	T_6	0	0	T_1	T_2	0	E_1	
	z	0	0	0	0	0	T_7	0	T^*_5	T_7	0	T_5	T_3	0	0	E_1		
O(1)²	x	T'_{14}	T'_{13}	0	0	T'_{15}	0	T^*_4	T^*_6	T_5	T_4	T_6	0	0	E_1			
	y	0	0	0	T'_{15}	0	T^*_5	T^*_5	0	T_7	T_5	0	0	E_1				
	z	0	0	$-T^*_{16}$	$-T^*_{16}$	0	T^*_7	T_{10}	0	0	0	0	E_1					
O(2)¹	x	$-T^*_{17}$	0	0	0	0	T_{11}	T_8	T_8	0	0	E_2						
	y	0	0	0	0	0	T_{12}	T_{12}	T_{10}	0	E_2							
	z	0	0	T_{16}	T_{16}	0	T_9	0	T_{11}	E_2								
O(2)²	x	T_{17}	0	0	0	0	0	0	E_2									
	y	0	0	0	0	0	0	E_2										
	z	0	0	0	0	0	E_2											
Cu	xy	T_{18}	0	0	0	E_3												
	yz	0	0	0	E_4													
	zx	0	0	E_5														
	x^2-y^2	0	E_6															
	z^2	E_7																

3-3. Computation Method

High-energy neutron scattering studies have shown a persistence of 2D antiferromagnetic spin correlation in the superconducting state of LSCO[77], and the ARPES results by Aebi *et al.*[102] have proved the prediction of a $\sqrt{2} \times \sqrt{2}$ antiferromagnetic local order by Kamimura and Suwa. In this context we calculate a new electronic structure in the superconducting concentration region in which, if the localized spins form antiferromagnetic ordering in a spin-correlated region, the carriers take the $^3B_{1g}$ high-spin multiplet state and the $^1A_{1g}$ low-spin multiplet state alternately in this spin-correlated region. In this respect a unit cell is taken so as to include two neighbouring CuO_6 octahedra with localized up- and down-spins. This unit cell is called "antiferromagnetic unit cell", and two neighbouring CuO_6 octahedra are called A-site and B-site, respectively.

The Hamiltonian matrix $\check{H}(k)$ consists of two parts; the one-electron part $\check{H}_0(k)$, and the effective interaction part $\check{H}_{int}(k)$, as described in Section 3-1. In the antiferromagnetic unit cell, the one-electron part Hamiltonian matrix $\check{H}_0(k)$ is expressed by 34×34 matrix as

$$\check{H}_0(k) = \begin{bmatrix} \hat{H}^0_{AA}(k) & \hat{H}^0_{BA}(k) \\ \hat{H}^0_{AB}(k) & \hat{H}^0_{BB}(k) \end{bmatrix} \qquad (3.8)$$

where $\hat{H}^0_{AA}(k)$, $\hat{H}^0_{BA}(k)$, $\hat{H}^0_{AB}(k)$ and $\hat{H}^0_{BB}(k)$ are the 17×17 matrices which represent Hamiltonian matrix components between A- and A-sites, B- and A-sites, A- and B-sites, and B- and B-sites, respectively. Their elements are defined in Table 3, and the expressions of its matrix elements are given in Appendix B. In the present calculation we have used [Table 3] the values of the SK parameters fitted to the APW calculation[96] by DeWeert *et al*[97]. Those values are given in Table 4. . [Table 4]

Now we will take into account the many-body interaction terms of Hamiltonian (1.1) in the 34×34 dimensional effective interaction part $\check{H}_{int}(k)$. In order to renormalize the

Table 3

Table 3: Matrix elements of $\tilde{H}_{AA}^0(\boldsymbol{k})$, $\tilde{H}_{AB}^0(\boldsymbol{k})$, $\tilde{H}_{BA}^0(\boldsymbol{k})$ and $\tilde{H}_{BB}^0(\boldsymbol{k})$, where $T^- = T(-k_z)$.

	O(1)¹ x	O(1)¹ y	O(1)¹ z	O(1)² x	O(1)² y	O(1)² z	O(2)¹ x	O(2)¹ y	O(2)¹ z	O(2)² x	O(2)² y	O(2)² z	Cu xy	Cu yz	Cu zx	Cu x^2-y^2	Cu z^2
O(1)¹ x	E_1	0	0	T_1	T_2	0	T_4	0	T_5	T_4^-	0	T_5^-	0	0	T_{15}	T_{13}	T_{14}
O(1)¹ y		E_1	0	T_2	T_1	0	0	T_6	0	0	T_6^-	0	T_{15}	0	0	0	0
O(1)¹ z			E_1	0	0	T_3	T_5	0	T_7	T_5^-	0	T_7^-	0	0	0	0	0
O(1)² x				E_1	0	0	T_4^-	0	T_5^-	T_8	T_{10}	T_{11}	T_{15}^-	0	0	T_{13}	T_{14}^-
O(1)² y					E_1	0	0	T_6^-	0	T_{10}	T_8	T_{12}	0	T_{15}^-	0	0	0
O(1)² z						E_1	T_5^-	0	T_7^-	T_{11}	T_{12}	T_9	0	0	0	0	0
O(2)¹ x							E_2	0	0	0	0	0	0	0	$-T_{16}^-$	0	0
O(2)¹ y								E_2	0	0	0	0	0	$-T_{16}^-$	0	0	0
O(2)¹ z									E_2	0	0	0	0	0	0	0	$-T_{17}^-$
O(2)² x										E_2	0	0	0	0	T_{16}	0	0
O(2)² y											E_2	0	0	T_{16}	0	0	0
O(2)² z												E_2	0	0	0	0	T_{17}
Cu xy													E_3	0	0	0	0
Cu yz														E_4	0	0	0
Cu zx															E_5	0	0
Cu x^2-y^2																E_6	T_{18}
Cu z^2																	E_7

---

on-site parameters in rydbergs

O(1) :in plane	E_p^1	0.2965
O(2) :apical	E_p^2	0.3333
Cu	E_{dxy}	0.3506
	$E_{dx^2-y^2}$ E_{dz^2}	0.4375

first-neighbor parameters in Ry

Cu-Cu	$t(dd\sigma)$	0.0048
	$t(dd\pi)$	−0.0049
	$t(dd\delta)$	−0.0058
Cu-O(1)	$t_1(dp\sigma)$	0.0921
	$t_1(dp\pi)$	0.0631
Cu-O(2)	$t_2(dp\sigma)$	0.0418
	$t_2(dp\pi)$	0.0277
O(1)-O(1)	$t_1(pp\sigma)$	0.0431
	$t_1(pp\pi)$	−0.0282
O(1)-O(2)	$t_2(pp\sigma)$	−0.0152
	$t_2(pp\pi)$	−0.0144
O(2)-O(2)	$t_3(pp\sigma)$	0.0126
	$t_3(pp\pi)$	−0.0018

Table 4 : The values of Slater-Koster parameters determined by DeWeert *et al.*

effects of the the exchange integral between the spin of a dopant hole and localized spin, K in Eq. (1.1), and the Hubbard U-like parameter into the carrier states, we first construct the antibonding b_{1g}^* orbital at A-site and B-site mainly consisting of a Cu $d_{x^2-y^2}$ atomic orbital, the bonding b_{1g} orbital at A-site and B-site consisting of the O p_σ orbitals in a CuO_2 layer hybridized by a Cu $d_{x^2-y^2}$ atomic orbital , and a_{1g}^* orbital at A-site and B-site consisting of Cu dz^2 orbital hybridized by Op_σ orbitals in a CuO_2 layer and Op_z orbitals of apical oxygen. The antibonding b_{1g}^* orbitals at A-site and B-site are accommodated by up-spin and down-spin holes, respectively, due to the Hubbard U interaction and the superexchange interaction. Then the a_{1g}^* state at A-site and the b_{1g} state at B-site constitute the $^3B_{1g}$ high-spin multiplet and the $^1A_{1g}$ low-spin multiplet, respectively, with the localized b_{1g}^* holes.

We construct localized states at A-site and B-site, by taking linear combination of the doubly degenerated eigenstates of the one-electron Hamiltonian $\tilde{H}_0(\boldsymbol{k}_0)$ where vector $\boldsymbol{k}_0$ indicates $(\frac{\pi}{2a}, \frac{\pi}{2a}, 0)$. This is possible because the eigenstates $|\boldsymbol{k}_0\rangle$ and $|-\boldsymbol{k}_0\rangle$ are degenerate, reflecting the fact that the difference between two wave vectors, $\boldsymbol{k}_0$ and $-\boldsymbol{k}_0$, coincides with a reciprocal lattice vector. The resultant eigenstates are $\sum_l \cos(\frac{\pi}{2a}x_l + \frac{\pi}{2a}y_l)\varphi_{al}$ and $\sum_l \sin(\frac{\pi}{2a}x_l + \frac{\pi}{2a}y_l)\varphi_{al}$, respectively, where φ_{al} are the Wannier type eigenstates of $\tilde{H}_0(\boldsymbol{k}_0)$ which are localized at lth-site and constructed with the linear combinations of atomic orbitals. Strictly speaking, these eigenstates are not localized only at a particular site, but we will consider these eigenstates as those localized at A-site and B-site. Using the transformation matrix $\tilde{U}(\boldsymbol{k}_0)$ which yields such localized eigenstates, $\tilde{H}_0(\boldsymbol{k}_0)$ is diagonalized;

$$\tilde{U}^{-1}(\boldsymbol{k}_0)\tilde{H}_0(\boldsymbol{k}_0)\tilde{U}(\boldsymbol{k}_0) = \tilde{E}_0(\boldsymbol{k}_0). \tag{3.9}$$

The eigenstates of $\tilde{E}_0$ are expressed as linear combinations of atomic orbitals localized at A-site or B-site; for example, a_{1g}^* orbital at A-site, a_{1g}^* orbital at B-site, b_{1g}^* orbital at A-site, b_{1g}^* orbital at B-site, and so on. In order to construct, for example, a_{1g}^* orbital at B-site, in numerical calculations we take a linear combination of two degenerate a_{1g}^* orbitals which correspond to the eigenstates $|\boldsymbol{k}_0\rangle$ and $|-\boldsymbol{k}_0\rangle$ so that the component of

Cu dz^2 orbital at A-site disappears.

If we renormalize the effects of the exchange interaction between the spin of a dopant hole and a localized spin, K in Eq. (1.1) into the carrier states, then, in the case of a dopant hole with up-spin, the energy of a electron in a_{1g}^* state at A-site is taken to be higher than that at B-site by Hund's coupling energy which is 2eV [103]. On the other hand, as regards the energy of b_{1g} state at B-site, it is first taken to be higher than that at A-site by the energy of the spin-singlet coupling in $^1A_{1g}$ multiplet which is 4eV [103]. Then we have to proceed to include the effects of the crystalline potential in LSCO, in the energy of b_{1g} state. Those are such as the energy difference between the $^3B_{1g}$ and $^1A_{1g}$ multiplets due to the effective Madelung energy which has been included in the cluster calculation by Kamimura and Eto [103]. In this context, we have added 2eV to the on-site energy of the b_{1g} orbital leaving the on-site energy of the a_{1g}^* orbital unchanged. As a result the energy of b_{1g} state at B-site which is the sum of the spin-singlet coupling energy, 4eV, and the on-site energy of b_{1g} orbital, 2eV, becomes 6eV. Thus the up-spin carriers take the $^3B_{1g}$ state at A-site and the $^1A_{1g}$ state at B-site for the k-values in the underdoped region. Lastly the energy of b_{1g}^* state in a CuO_6 cluster with localized up-spin (A-site) is taken to be higher than that in a CuO_6 cluster with localized down-spin (B-site) by Hubbard U parameter, which is taken as 10eV in the present treatment in order to separate the localized spin band b_{1g}^* from the hole carrier system.

Then the total Hamiltonian $\tilde{H}(\boldsymbol{k})$ is constructed with the one-electron part and the effective interaction part, and the effective interaction part has the eigenvalue of the b_{1g}^* state at A-site which is +10eV, that of b_{1g}^* state at B-site −10eV, that of b_{1g} state at B-site +6eV, that of a_{1g}^* state at A-site +1eV and that of a_{1g}^* state at B-site −1eV. Here it should be noted that $\tilde{H}(\boldsymbol{k})$ is the Hamiltonian matrix for a electron but not a hole. Then the total Hamiltonian $\tilde{H}(\boldsymbol{k})$ should be transformed by transformation matrix $\tilde{U}(\boldsymbol{k}_0)$, as

$$\tilde{U}^{-1}(\boldsymbol{k}_0)\tilde{H}(\boldsymbol{k}_0)\tilde{U}(\boldsymbol{k}_0) = \tilde{E}_0(\boldsymbol{k}_0) + \tilde{E}_{int}(\boldsymbol{k}_0). \tag{3.10}$$

where

$$\tilde{E}_{\text{int}}(\boldsymbol{k}_0) = \begin{bmatrix} \ddots & & & & & & \\ & +10 & & & & & \\ & & -10 & & & & \\ & & & \ddots & & & \\ & & & & +1 & & \\ & & & & & -1 & \\ & & & & & & \ddots & \\ & & & & & & & +6 \\ & & & & & & & & \ddots \end{bmatrix} \quad \begin{matrix} \vdots \\ \text{A-site } b_{1g}^* \\ \text{B-site } b_{1g}^* \\ \vdots \\ \text{A-site } a_{1g}^* \\ \text{B-site } a_{1g}^* \\ \vdots \\ \text{B-site } b_{1g} \\ \vdots \end{matrix} \quad (3.11)$$

with the energy being measured in eV. By inverse transformation we can obtain, $\tilde{H}_{\text{int}}(\boldsymbol{k}_0) = \tilde{U}(\boldsymbol{k}_0)\tilde{E}_{\text{int}}(\boldsymbol{k}_0)\tilde{U}^{-1}(\boldsymbol{k}_0)$. The similar calculation with respect to $\boldsymbol{k}_0' = (\frac{\pi}{2a}, -\frac{\pi}{2a}, 0)$ gives $\tilde{H}_{\text{int}}(\boldsymbol{k}_0')$ as well.

Then, using the approximation that the effective interaction term $\tilde{H}_{\text{int}}$ have matrix elements only between nearest neighbor atomic orbitals, we can represent the $\boldsymbol{k}$ dependence of the effective interaction part of the Hamiltonian matrix, $\tilde{H}_{\text{int}}(\boldsymbol{k})$, as is shown in Appendix C. Then we can determine $\langle a|\tilde{H}_{\text{int}}^{\text{even}}|b\rangle$ and $\langle a|\tilde{H}_{\text{int}}^{\text{odd}}|b\rangle$, where 'even' and 'odd' mean that the interchanging of the two atomic orbitals, a and b, produces $+1$ and -1 in sign, respectively. In this way we can include the exchange interaction terms of Hamiltonian (1.1) and the Hubbard U interaction for the localized holes in b_{1g}^* orbital in the the 34×34 dimensional effective interaction part $\tilde{H}_{\text{int}}(\boldsymbol{k})$. As for the value for the difference between $\epsilon_{a_{1g}^*}$ and $\epsilon_{b_{1g}}$ in Eq. (1.1), it is taken so as to reproduce the energy difference between multiplets $^3B_{1g}$ and $^1A_{1g}$ calculated by Kamimura and Eto[8].

As described above, all the matrix elements in the 34×34 dimensional Hamiltonian matrix ($\tilde{H}$) become one-electron type on the result of the mean field approximation, and thus we can diagonalize it easily. In this way we can obtain a band structure including the many-body effects dealt with like a molecular field acting on the dopant holes for LSCO.

Chapter 4.

The Numerical Results of the Electronic Structure and Renormalized Fermi Surface of $\text{La}_{2-x}\text{Sr}_x\text{CuO}_4$

4-1. Effective One-Electron Type Band Structure

In the previous section, all the matrix elements in the 34×34 dimensional Hamiltonian matrix $\tilde{H}(\boldsymbol{k})$ have been expressed as one-electron type, due to the molecular field approximation. By diagonalizing it, we have obtained a one-electron type band structure including the many-body effects in a mean-field sense for LSCO. The obtained band structure for up-spin dopant holes is shown in Fig. 20, where the Brillouin zone is also shown in the inset. The same shape of the band structure is also obtained for down-spin dopant holes. Here one should note that the energy in this figure is taken for electron energy and the Hubbard bands for localized b_{1g}^* holes are removed from this figure.

In the undoped La_2CuO_4 all the bands except for upper Hubbard b_{1g}^* band are occupied by electrons so that La_2CuO_4 is an insulator. In this respect our band structure is completely different from the ordinary energy band obtained by the local density approximation (LDA). The localized holes are accommodated in the upper Hubbard b_{1g}^* band which consist mainly of $d_{x^2-y^2}$ orbitals forming AF spin ordering, while the dopant holes in the highest band in Fig. 20 marked by # 1 have mainly O p_σ character. Thus the present theory shows definitely that La_2CuO_4 is a charge transfer type insulator,
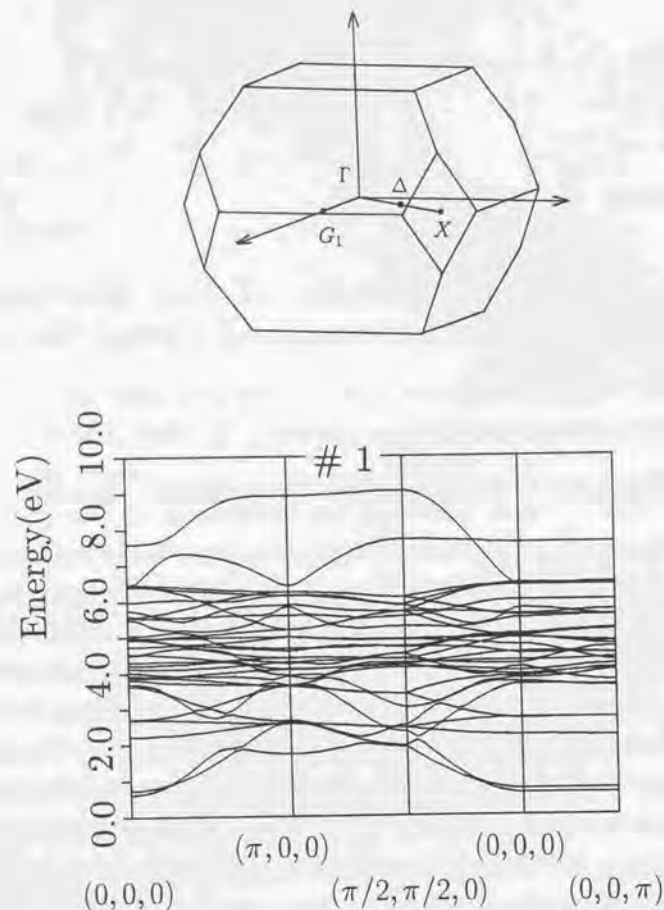
Figure 20: The many-body-effect included band-structure for up-spin dopant holes, obtained by solving the effective one-electron-type 34×34 dimensional Hamiltonian matrix $\tilde{H}$ for an antiferromagnetic unit cell, where the ordinary Brillouin zone corresponding to an ordinary unit cell consisting of a single CuO_6 octahedron is shown in the upper part of the figure. The highest occupied band is marked by #1. The Δ-point corresponds to $(\pi/2a,\ \pi/2a,\ 0)$, while the G_1-point to $(\pi/a,\ 0,\ 0)$. In this figure the Cu-O-Cu distance, a, is taken to be unity.

consistent with the experimental result[67,44].

Now let us introduce holes into this undoped La_2CuO_4. Then doped holes are accommodated in the highest band in Fig. 20 marked by #1 (referred as the conduction band hereafter). The wave function of the conduction band for up-spin holes consists of a_{1g}^* orbitals at A-site and b_{1g} orbitals at B-site, as will be shown in Section 4-2. Besides the localized b_{1g}^* holes in the upper Hubbard bands, a_{1g}^* orbitals at A-site and b_{1g} orbitals at B-site form the $^3B_{1g}$ high-spin multiplet state and $^1A_{1g}$ low-spin multiplet state, respectively. Thus the present calculated results realize the electronic structure, where the carriers take $^3B_{1g}$ high-spin state and $^1A_{1g}$ low-spin state alternately in the spin-correlated region.

In the present calculation we have assumed the long range AF order, while the results of neutron inelastic scattering experiments[20] suggest that the localized spins are fluctuating and there is no long range AF order in the superconducting regime although the local AF order has been observed. Thus it is necessary to discuss how the fluctuation of localized spins affect the experimental properties of LSCO. Let λ_s be the characteristic length within which the coherent motion of a dopant hole is retained due to the local AF order. Then the simplest picture for the electronic states with the fluctuation effect taken into account, is that the holes in the present conduction band have coherence within an area whose radius is the spin correlation length λ_s. In other word the holes have coherence within a time τ_s defined as $v_F\tau_s = \lambda_s$, where v_F is the velocity of the holes near the Fermi surface. As regards the angle resolved photoemission (ARPES) or other optical phenomena the effect of non-existence of long range AF order is considered to be small, since the time scale of optical measurement is shorter than the characteristic frequency $1/\tau_s$. It does not affect seriously the transport properties when the mean free path is smaller compared with λ_s due to strong electron-phonon interaction. On the other hand it affects seriously the thermal properties because the characteristic time scale is much longer than τ_s. The Fermi surface is affected by it and becomes to have finite lifetime. It also affects seriously the superconductivity and reduces T_c by eliminating the contribution from the retarded effective pair interaction of time argument larger than τ_s as is shown in section 6-5.

4-2. Features of the Conduction Band and Density of States

When Sr are doped, holes begin to occupy the top of the conduction band at Δ which corresponds to $(\pi/2a, \pi/2a, 0)$. At the onset concentration of superconductivity, x_c, the Fermi level is located at the energy of $E = 9.04eV$ which is a little higher than that of the G_1 point, where the G_1 point in the Brillouin zone corresponds to $(\pi/a, 0, 0)$. The characteristic feature of the conduction band is the existence of the flat band along the line G_1 to Δ. This is consistent with the angle-resolved photoemission data by Shen et al.[104] and Desseau et al.[105], who observed an extended region of flat band very near E_F around $\overline{M}$ point, which corresponds, in the present notation, to G_1 in the Brillouin zone, $(\pi/a, 0, 0)$.

In Fig. 21 the wave functions of an up-spin carrier in the antiferromagnetic unit cell $\boxed{\text{Fig. 21}}$ are shown for Δ and G_1 points, where the right hand side of the figure corresponds to a CuO_6 cluster with localized up-spin (A-site) while the left hand side to a CuO_6 cluster with localized down-spin (B-site) in the antiferromagnetic unit cell, and the figure of an orbital is drawn in a large size when the probability of finding a hole in the orbital is large. The mixing ratio of the in-plane Op, apical Op, $Cu\ dx^2 - y^2$ and $Cu\ dz^2$ orbitals in the wave function for five k values along the line G_1 to Δ in the Brillouin zone are shown in Table 5, where the provability of finding a hole in each atomic orbital is shown. One can see from Fig. 21 and Table 5 that, in the concentration below the onset of $\boxed{\text{Table 5}}$ superconductivity, the holes with up-spin are accommodated in b_{1g} orbital constructed mainly from the oxygen p_σ orbitals in a CuO_2 plane, consistent with the result of the cluster calculation by Kamimura and Eto[8], while in the superconducting concentration region the holes hop coherently from a_{1g}^* orbital at the A-site to b_{1g} orbital at the B-site.

The calculated result shows that mixing ratio of the $^1A_{1g}$ state to the $^3B_{1g}$ state for the k value of $(3\pi/8, 5\pi/8, 0)$ in the underdoped regime of LSCO is 7 to 1, as shown
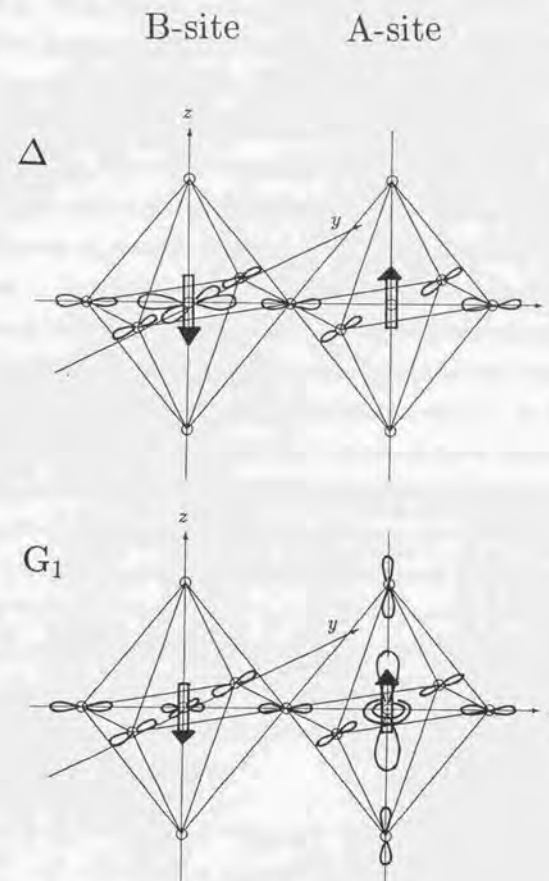
Figure 21: The wave functions at Δ and G_1 points. Here, the right hand side of the figure corresponds to a CuO_6 cluster with localized up-spin (A-site) and the left hand side to a CuO_6 cluster with localized down-spin (B-site).

(k_x, k_y, k_z)	in-plane Op	apical Op	$dx^2 - y^2$	dz^2
$(\frac{1}{2}\pi, \frac{1}{2}\pi, 0)$	0.61	0.0	0.39	0.0
$(\frac{3}{8}\pi, \frac{5}{8}\pi, 0)$	0.58	0.003	0.37	0.05
$(\frac{1}{4}\pi, \frac{3}{4}\pi, 0)$	0.49	0.01	0.33	0.17
$(\frac{1}{8}\pi, \frac{7}{8}\pi, 0)$	0.41	0.02	0.29	0.28
$(0, \pi, 0)$	0.38	0.02	0.28	0.32

Table 5: The mixing ratio of the in-plane Op, apical Op, Cu $dx^2 - y^2$ and Cu dz^2 orbitals in the wave function for five k values along the line G_1 to Δ in the Brillouin zone.

in Table 5. Thus, although we have mentioned that the alternating appearance of the Zhang-Rice singlet $^1A_{1g}$ and the Hund's coupling triplet $^3B_{1g}$ is the characteristic feature of the electronic structure of the underdoped superconducting regime of LSCO, the result of Table 5 indicates that the weight of the $^1A_{1g}$ state is about seven times stronger than that of the $^3B_{1g}$. This result is consistent with the experimental one by the polarized XAS by C. T. Chen *et al.*[19] They have observed the doping-induced satellite peak(L_3') for both polarizations of the electric vector of X-ray, E, parallel and perpendicular to the c-axis, in the shoulder area of the doping-independent Cu L_3 line, where the L_3 line corresponds to the transitions from Cu 2p core level to the upper Hubbard Cu $d_{x^2-y^2}$ band. Since the $E\|c$ and the $E\perp c$ polarizations detect the existence of a_{1g}^* and b_{1g} states, respectively, the appearance of the doping-induced satellite peak for both polarizations at nearly the same energy has suggested that the state of dopant holes must consist of both a_{1g}^* and b_{1g} states. According to Kamimura, Ohura and Chen[106], the large difference in the intensities between $E\perp c$ and $E\|c$ polarizations is due to the large difference between the components of b_{1g} and a_{1g}^* in the wave functions for the wave vectors on the Fermi surfaces[106].

Reflecting the alternate appearance of a_{1g}^* and b_{1g} orbitals among A and B sites, the top of the conduction band in Fig. 20 appears at the Δ point in the Brillouin zone, where the Δ point corresponds to $(\pi/2a, \pi/2a, 0)$. The conduction band is approximated in the following form,

$$
\begin{aligned}
E_{\mathbf{k}} = \quad & A \quad [\cos(ak_x + ak_y) + \cos(-ak_x + ak_y)] \\
+ \quad & B \quad \cos(ak_x + ak_y)\cos(-ak_x + ak_y) \\
+ \quad & C \quad \cos(ak_x + ak_y)\cos(-ak_x + ak_y)\cos\frac{a}{2}k_x\cos\frac{a}{2}k_y\cos\frac{c}{2}k_z \\
+ \quad & D \quad [\cos(ak_x + ak_y) + \cos(-ak_x + ak_y)]\cos\frac{a}{2}k_x\cos\frac{a}{2}k_y\cos\frac{c}{2}k_z \\
+ \quad & E_0 \quad .
\end{aligned}
\tag{4.1}
$$

Here a and c are the lattice constants of the tetragonal unit cell, where $a = 3.78$Å and $c = 13.25$Å. The values of coefficient A to E_0 in Eq. (4.1) are determined so as to reproduce the numerically calculated conduction band. The value of A to E_0 thus determined are
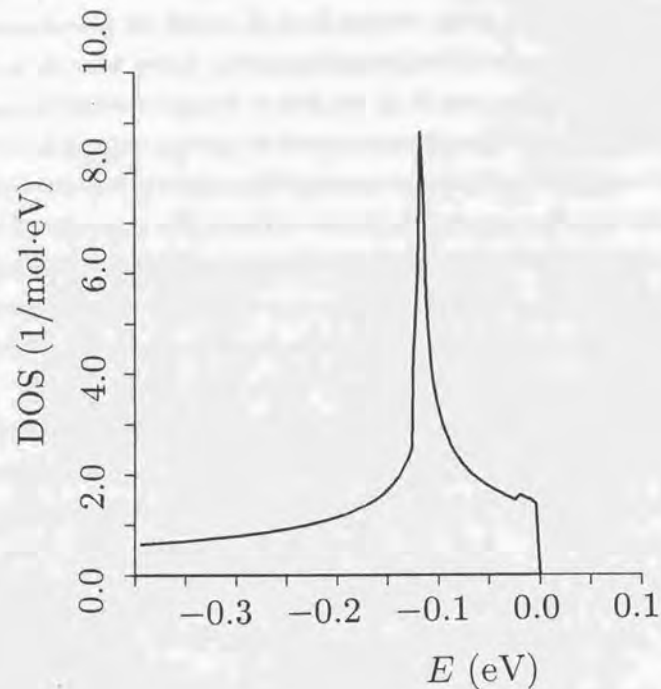
55

Figure 22: The density of states of LSCO as a function of energy. The solid lines are the calculated one of the #1 band in the renormalized band structure[23,25]. The energy is measured from the top of the band. Holes enter from the top.

$A = -0.3311$ eV, $B = -0.3936$ eV, $C = -0.0006$ eV, $D = -0.0047$ eV and $E_0 = 8.647$ eV. The lower energy region of the conduction band does not fit well to the one calculated numerically. However, this disagreement does not influence the following calculation because only the upper energy region of the conduction band above $E \geq 8.9$eV contributes to the electronic structure for the hole concentration region of $x \leq 0.4$.

We have also calculated the density of states of the conduction band in LSCO. The calculated density of states is shown as a function of energy in Fig. 22, where the origin of the energy is taken at the top of the conduction band at the Δ point. The density of states for the conduction band has a sharp peak at E_F corresponding to $x \sim 0.3$ in $La_{2-x}Sr_xCuO_4$. The appearance of this sharp peak is due to a modified type of a saddle point singularity at G_1 point, as described below. The energy of the conduction band near the G_1 point increases towards the Δ point (along the direction of $(\pm 1, \pm 1, 0)$), while it decreases towards the Γ point (along the direction of $(\pm 1, 0, 0)$ or $(0, \pm 1, 0)$).

Fig. 22

57

4-3. Fermi Surface Structure

We have constructed the Fermi surfaces, based on the calculated energy of the conduction band shown in Fig. 20 This Fermi surface is completely different from that of an ordinary Fermi liquid calculated by the local density approximation (LDA), as already pointed out by us[36,43], because the conduction band in the present result is fully occupied by electrons in the undoped case while the LDA band always yield a metallic state. Further a carrier system with up or down spin has a respective Fermi surface, although their shape and their position in k-space are the same. The Fermi surface is constructed, by connecting the points in the k-space at which the Fermi distribution function shows discontinuity. In Fig. 23 the Fermi surface structures thus obtained for | Fig. 23 | $x = 0.05$, 0.1, 0.125, 0.15, and 0.2 are shown, where one Fermi surface consists of two pairs of extremely flat tube, which are directed along bisectors between k_x and k_y axis and are orthogonal to each other and displaced by $Q_1 = (\pi/a, \pi/a, 0)$ or $Q_2 = (-\pi/a, \pi/a, 0)$ due to the folding effect based on the antiferromagnetic unit cell. Although four flat tubes are shown in this figure, two of these are the Fermi surfaces translated by reciprocal lattice vector. Then we should say 'two pairs of flat tube' instead of 'four flat tubes'.

It should be noticed that the appearance of the center of the Fermi surfaces at the Δ point is due to the alternant appearance of $^1A_{1g}$ and $^3B_{1g}$ multiplets among A and B sites. Let us assume, for example, a simple folding of a b_{1g} band in the presence of the AF order. Then the dopant holes are accommodated from the top of the upper branch of the folded b_{1g} band at Γ-point which corresponds to the k value of $(0,0,0)$, since the undoped La_2CuO_4 is a charge transfer type insulator and both the upper and the lower branches of the folded b_{1g} bands are fully occupied by electrons in the undoped case. Therefore the center of the Fermi surface is at Γ-point in this case. On the other hand, according to the present calculation, the b_{1g} and a_{1g}^* bands split into four bands in the presence of AF order. The upper two bands among the four bands corresponding to a

58

character consisting of a_{1g}^* orbitals at A-site and b_{1g} orbitals at B-site and the character of lower two bands consist of a_{1g}^* orbitals at B-site and b_{1g} orbitals at A-site. Since both the b_{1g} and the a_{1g}^* bands are fully occupied by electrons in the undoped La_2CuO_4, the dopant holes are accommodated from the top of the highest band, and thus the character of the highest band is not pure b_{1g} orbitals, but the mixture of two kinds of orbitals, a_{1g}^* and b_{1g}. Therefore, the result of the present calculation that the Δ-point is the top of this highest band is not obtained by a simple folding of a energy band in the presence of the AF order. Thus in order to obtain the present Fermi surface structure, it is essential to take account of the alternating appearance of b_{1g} and a_{1g}^* orbitals for a dopant hole in addition to b_{1g}^* orbital for a localized spin.

The cross-section of each Fermi surface is very small as seen in Fig. 23, and the dispersion of the conduction band is relatively flat. This unique feature of the Fermi surface structure is consistent with the experimental results of the angle-resolved photoemission (ARPES) for the superconducting $Bi_2Sr_{0.97}Pr_{0.03}CuO_{6+\delta}$ (Bi 2201) compounds which includes a single CuO_2 layer in a unit cell, like LSCO[107]. Fermi surface structures for $Bi_2Sr_2CaCu_2O_{8+\delta}$ (Bi 2212) determined by angle-resolved photoemission[102,104,105,108,109] are also very alike to the present result, although the Fermi surface structure for Bi2212 is more complicated due to the existence of two CuO_2 layers in a unit cell. Shen et al.[104] and Desseau et al.[105] have mapped out the near-E_F electronic structure and Fermi surface of Bi 2212 by angle-resolved photoemission. They have observed an extended region of the flat CuO_2 derived bands very near E_F around $\overline{M}$ point, that is the G_1 point in our notation, and the strong tendency of the nesting of the Fermi surface for a nesting vector Q near (π, π) which is responsible for many of the anomalous physical properties of the hole-type cuprates. In particular, Aebi et al[102,108] has found a c(2×2) superstructure on the Fermi surface suggesting the short range antiferromagnetic correlation. In fact, their Fermi surfaces with superstructure are shown in Fig. 24, where the calculated Fermi surface is also shown schematically for | Fig. 24 | comparison. It is easily seen from Fig. 24 that the ARPES results by Aebi et al. coincides well with the calculated Fermi surface. This means that our prediction of a $\sqrt{2} \times \sqrt{2}$

59

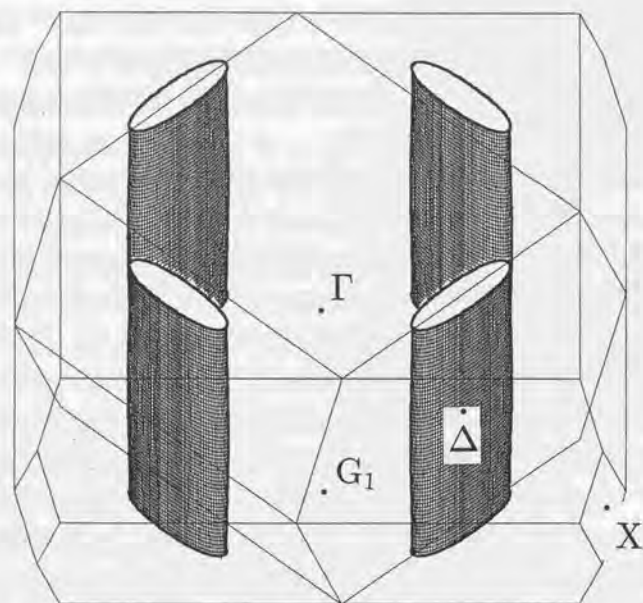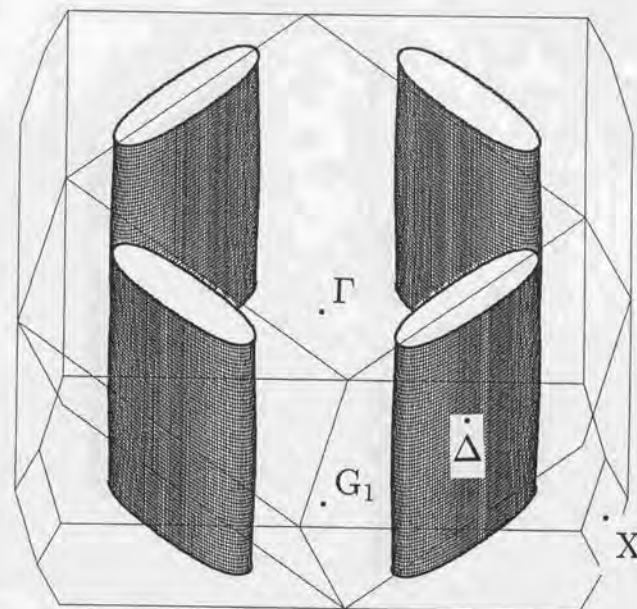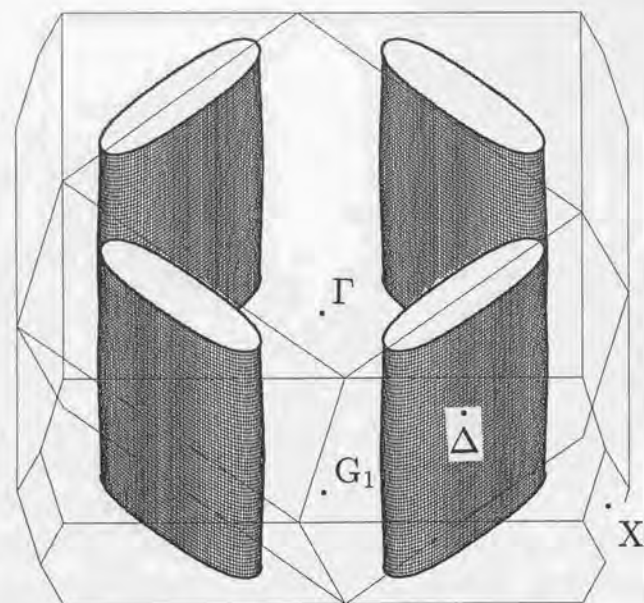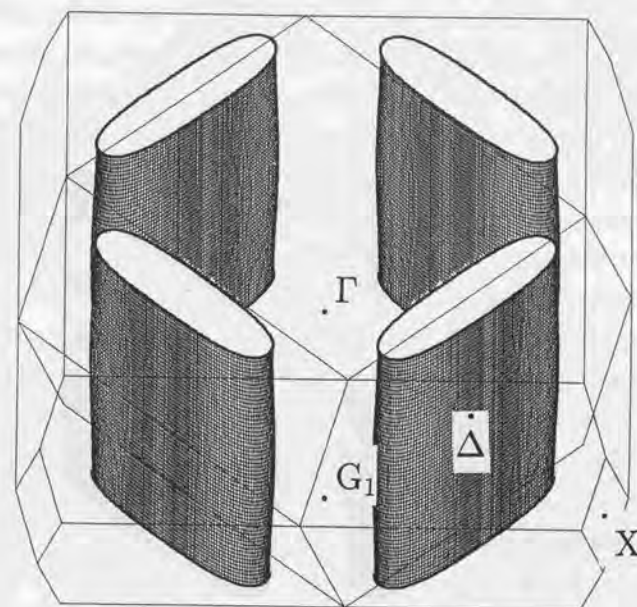FERMI SURFACE (X=0.05)
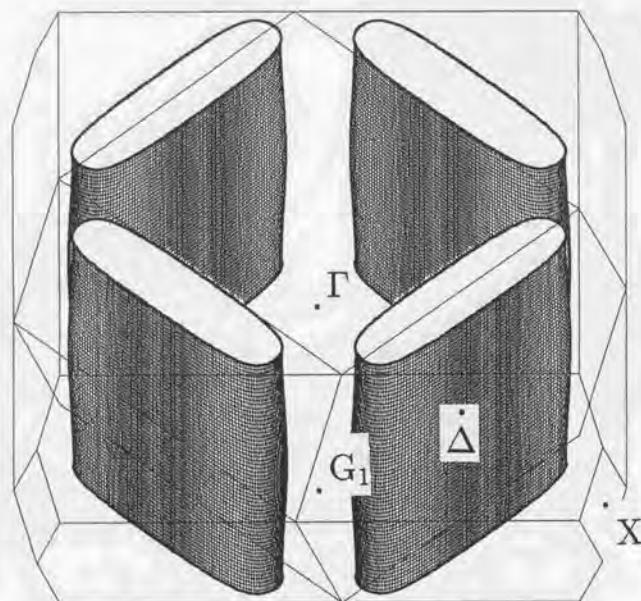
FERMI SURFACE (X=0.10)

Figure 23: (a) The Fermi surface for $x = 0.05$ calculated for the #1 band. Here two kinds of Brillouin zones are also shown. One at the outermost part is the ordinary Brillouin zone and the inner part is the folded Brillouin zone for the antiferromagnetic unit cell in LSCO. Here the k_x axis is taken along $\overline{\Gamma G_1}$, corresponding to the x-axis (the Cu - O - Cu direction) in a real space.

Figure 23: (b) The Fermi surface for $x = 0.1$ calculated for the #1 band. Here two kinds of Brillouin zones are also shown. One at the outermost part is the ordinary Brillouin zone and the inner part is the folded Brillouin zone for the antiferromagnetic unit cell in LSCO. Here the k_x axis is taken along $\overline{\Gamma G_1}$, corresponding to the x-axis (the Cu - O - Cu direction) in a real space.

Figure 23: **(c)** The Fermi surface for $x = 0.125$ calculated for the #1 band. Here two kinds of Brillouin zones are also shown. One at the outermost part is the ordinary Brillouin zone and the inner part is the folded Brillouin zone for the antiferromagnetic unit cell in LSCO. Here the k_x axis is taken along $\overline{\Gamma G_1}$, corresponding to the x-axis (the Cu - O - Cu direction) in a real space.

Figure 23: **(d)** The Fermi surface for $x = 0.15$ calculated for the #1 band. Here two kinds of Brillouin zones are also shown. One at the outermost part is the ordinary Brillouin zone and the inner part is the folded Brillouin zone for the antiferromagnetic unit cell in LSCO. Here the k_x axis is taken along $\overline{\Gamma G_1}$, corresponding to the x-axis (the Cu - O - Cu direction) in a real space.

FERMI SURFACE (X=0.20)

Figure 23: (e) The Fermi surface for $x = 0.2$ calculated for the #1 band. Here two kinds of Brillouin zones are also shown. One at the outermost part is the ordinary Brillouin zone and the inner part is the folded Brillouin zone for the antiferromagnetic unit cell in LSCO. Here the k_x axis is taken along $\overline{\Gamma G_1}$, corresponding to the x-axis (the Cu - O - Cu direction) in a real space.

antiferromagnetic local order has been proved experimentally. Further Marshall *et al.*[110] have also observed a small Fermi surface structure for the underdoped Dy concentration of $Bi_2Sr_2Ca_{1-x}Dy_xCu_2O_{8+\delta}$ with $T_c = 65K$, consistent with our prediction of a small Fermi surface. Here it should be remarked that the present Fermi surface structure is completely different from that obtained by simply folding a large Fermi surface due to the long range antiferromagnetic ordering, but that it is a reflection of the alternant appearance of the $^1A_{1g}$ and $^3B_{1g}$ multiplets as mentioned before.

Although the present calculation is based on a periodic system with the antiferromagnetic order, in a real system the spin correlation length is finite so that the appearance of the small Fermi surface structure has a finite lifetime. As a result various phenomena based on the present small Fermi surface structure are expected to have lifetime effects. For example, the outer edge of each section in the Fermi surface structure shown in Fig. 23(a)-(e) is not sharp compared with its inner edge due to the above lifetime effect, so that it might be very difficult to see both edge of each section in the Fermi surface clearly in the angle-resolved photoemission experiments. This is one of the reasons why the angle-resolved photoemission experiments can not determine clearly whether the Fermi surfaces are large or small. When the spin-correlation length becomes smaller, the regions of antiferromagnetic ordering become comparable to the mean-free path of carriers from the over-doped to the well over-doped region. In this case dynamical effects might make the boundary of the Fermi surfaces vague and the folding effect due to the local AF order on the Fermi surfaces may disappear and thus the present narrow Fermi surfaces may change into a large Fermi surface. This may explain the " cross-over phenomena " observed in various normal state transport properties. In connection with the appearance of the small Fermi surface one might have a question on whether the Fermi surface should include the contribution from the localized spin or not in connection with Luttinger's theorem[111]. The present small Fermi surface does not include the contribution from localized spins. However, this does not contradict the Luttinger theorem because the antiferromagnetic ordering exists locally in the present case.
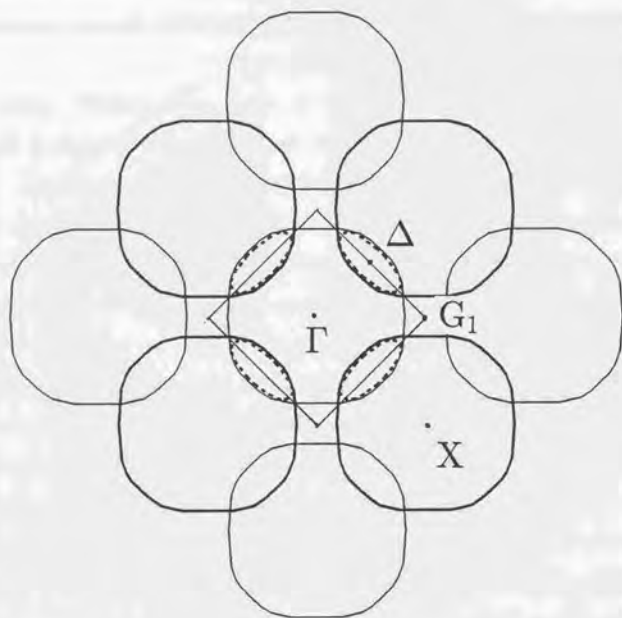
Figure 24: ARPES data of Aebi *et al* on Bi 2212, showing the Fermi surfaces. The weaker line and the stronger line observed in the measurement are distinguished by the thin solid line and the thick solid line respectively. The Fermi surface calculated for # 1 band is also shown schematically by dotted line for convention.

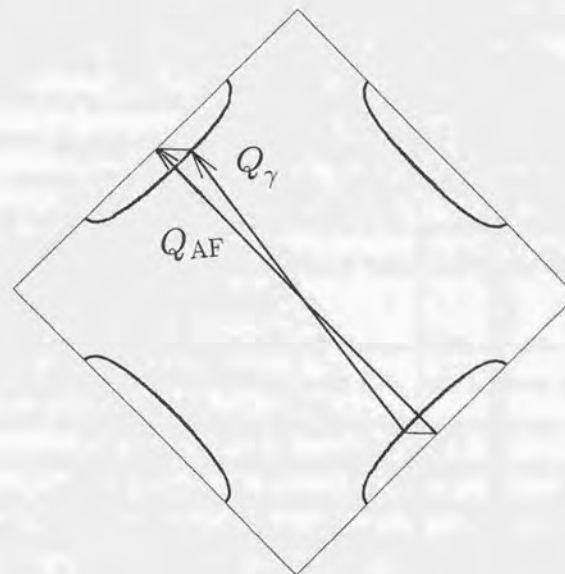**Figure 25:** (a) The Fermi surfaces in the k_x-k_y plane for $x = 0.1$ with the folded Brillouin zone for the antiferromagnetic unit cell in LSCO, and schematical view of the nesting vectors Q_γ, and the AF spanning vector Q_{AF}.
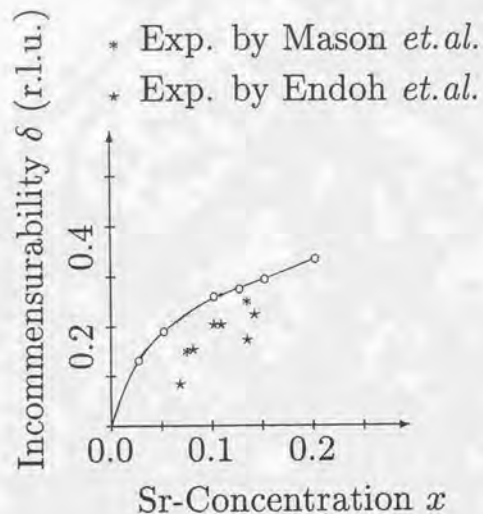
Figure 25: (b) Incommensurability δ in r.l.u. Circles are the calculated results.

A possible explanation of the origin for incommensurate peak observed in the inelastic neutron scattering experiment[112,78] might also be given by the unique shape of the present Fermi surface. We have already pointed out a possibility of nesting between Fermi surfaces with different spins for the nesting wave vector of Q_γ, which is deviated from commensurate wave vector $(-\pi, \pi, 0)$ by $(\delta \cdot \pi, 0, 0)$ as seen in Fig. 25(a). This nesting may be related to the appearance of incommensurate peak in the spin excitation spectra of LSCO observed by neutron diffraction experiments[112,78]. The incommensurability δ observed in neutron diffraction experiments for LSCO is determined from the nesting wave vector Q_γ for the calculated Fermi surfaces, and the results are plotted with open circles in Fig. 25(b), for various Sr-concentration. It shows non-linearity consistent with the experimental results by Endoh et.al.[76].

The 1/8 anomalies in $La_{1.875}Ba_{0.125}CuO_4$ may be explained on the basis of the present Fermi surface. In Fig. 26 the Fermi surfaces in the k_x-k_y plane is shown together with the Fermi surfaces translated by 'nesting' wave vector $\pi/2a$. These figures clearly show that the Fermi surfaces may nest by the 'nesting' wave vector $\pi/2a$ for the concentration region $x = 0.125 \sim 0.15$, despite of the shape of the Fermi surface for which nesting seems improbable. Because the density of states near the corner of the Fermi surface is large as is easily known from the small dispersion near G_1 along both the line G_1 to Δ and that G_1 to Γ in Fig. 20, an effective 'nesting' effect is expected to be large. The nesting of the Fermi surface with the 'nesting' wave vector $\pi/2a$ creates an energy gap at the part of Fermi surface and causes an suppressing effect on the appearance of superconductivity. In $La_{1.875}Ba_{0.125}CuO_4$, the 1/16 of total La atoms are substituted by Ba. As the substitution of Ba for La is accompanied with a displacement of apical oxygen, it creates a potential with the local periodicity $4a$ if the dopant Ba atoms are in local order. The potential with periodicity $4a$ hybridizes the two holes whose wave vectors are different from each other by the wave vector $\pi/2a$, and thus cooperate with the 'nesting' of Fermi surface for creating an energy gap at the Fermi surface.

Fig. 25

Fig. 26

FERMI SURFACE (X=0. 05)
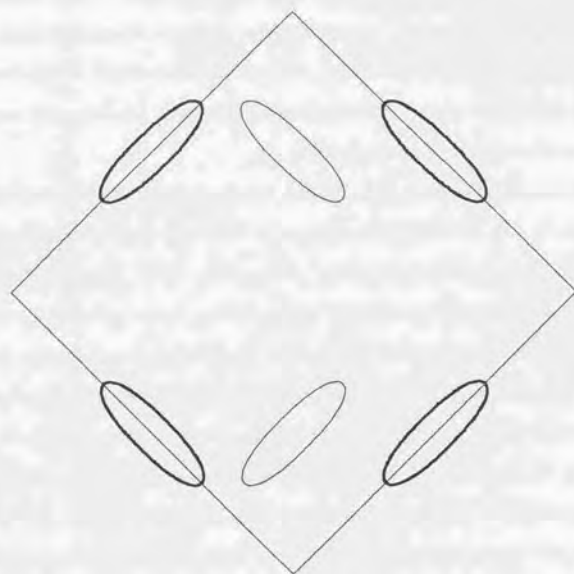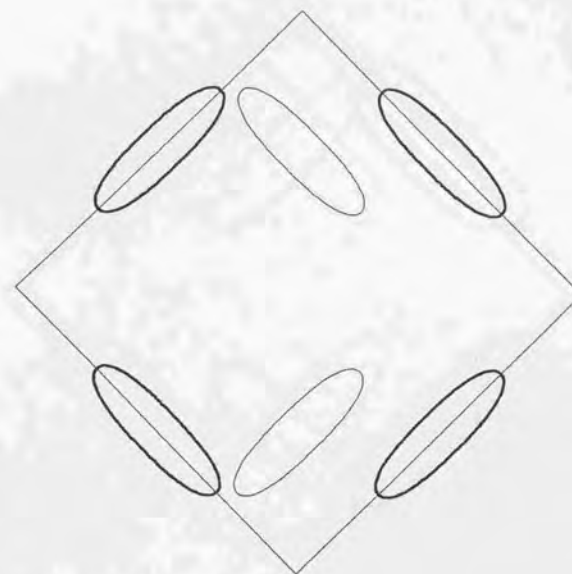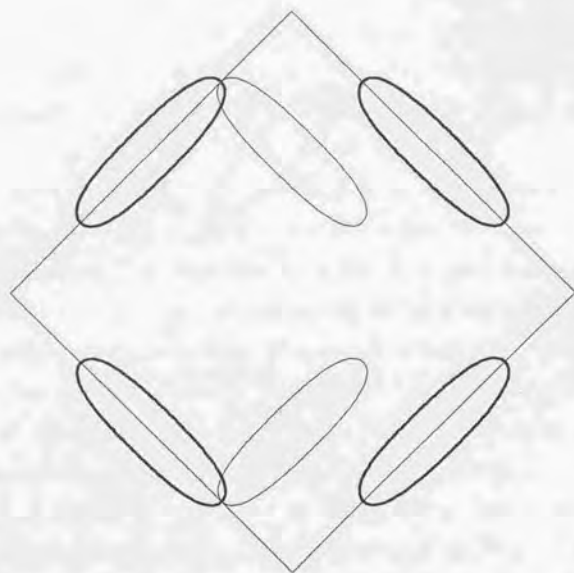
FERMI SURFACE (X=0. 075)

Figure 26: (a) The Fermi surfaces in the k_x-k_y plane for $x = 0.05$ with the folded Brillouin zone for the antiferromagnetic unit cell in LSCO. The Fermi surface drawn with thin solid line shows the Fermi surfaces transrated by 'nesting' wave vector $\pi/2a$.

Figure 26: (b) The Fermi surfaces in the k_x-k_y plane for $x = 0.075$ with the folded Brillouin zone for the antiferromagnetic unit cell in LSCO. The Fermi surface drawn with thin solid line shows the Fermi surfaces transrated by 'nesting' wave vector $\pi/2a$.
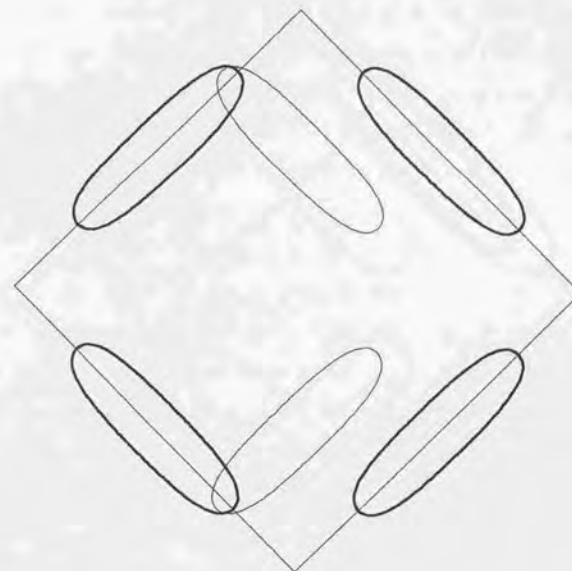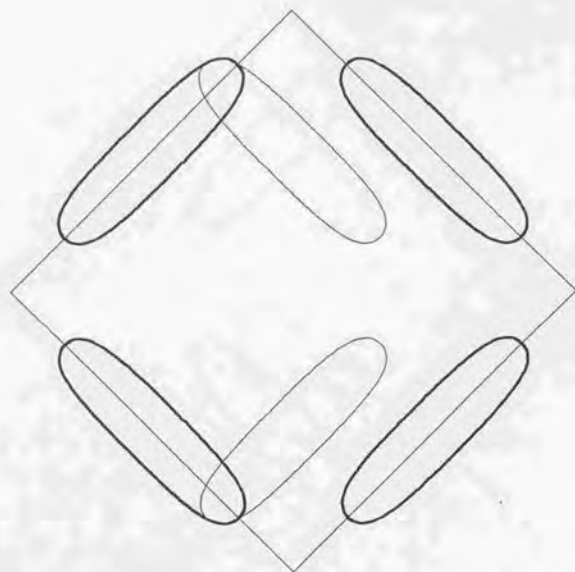
FERMI SURFACE (X=0.10)

FERMI SURFACE (X=0.125)

Figure 26: (c) The Fermi surfaces in the k_x-k_y plane for $x = 0.1$ with the folded Brillouin zone for the antiferromagnetic unit cell in LSCO. The Fermi surface drawn with thin solid line shows the Fermi surfaces transrated by 'nesting' wave vector $\pi/2a$.

Figure 26: (d) The Fermi surfaces in the k_x-k_y plane for $x = 0.125$ with the folded Brillouin zone for the antiferromagnetic unit cell in LSCO. The Fermi surface drawn with thin solid line shows the Fermi surfaces transrated by 'nesting' wave vector $\pi/2a$.
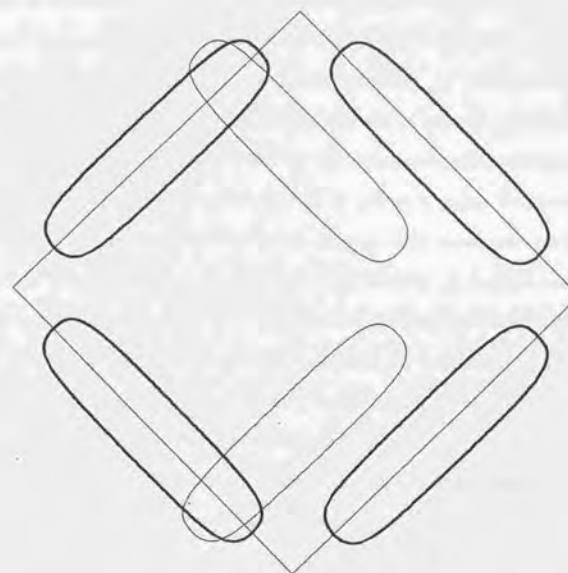
FERMI SURFACE (X=0.15)

Figure 26: (e) The Fermi surfaces in the k_x-k_y plane for $x = 0.15$ with the folded Brillouin zone for the antiferromagnetic unit cell in LSCO. The Fermi surface drawn with thin solid line shows the Fermi surface transrated by 'nesting' wave vector $\pi/2a$.

FERMI SURFACE (X=0.20)

Figure 26: (f) The Fermi surfaces in the k_x-k_y plane for $x = 0.2$ with the folded Brillouin zone for the antiferromagnetic unit cell in LSCO. The Fermi surface drawn with thin solid line shows the Fermi surfaces transrated by 'nesting' wave vector $\pi/2a$.

4-4. Conclusions

In this chapter the effective one-electron-type band structure is derived, by renormalizing the effects of the exchange integral between the spins of a dopant hole and localized spin, K in Eq. (1.1), and the Hubbard U-like parameter in Eq. (1.1) into the carrier states. In doing so we obtain the effective one-electron type band structure in which the antibonding b_{1g}^* orbitals which have a main character of Cu $d_{x^2-y^2}$ atomic orbital are localized at Cu site by the strong U effect and the spins of localized holes in b_{1g}^* orbitals are coupled antiferromagnetically by the effect of the superexchange interaction between the localized spins, J in Eq. (1.1), and in the concentration below the onset of superconductivity the holes with up-spin are accommodated in b_{1g} orbital constructed mainly from the oxygen p_σ orbitals in a CuO_2 plane, consistent with the result of the cluster calculation by Kamimura and Eto[8], while in the superconducting concentration region the holes itinerate from a_{1g}^* orbital at the A-site to b_{1g} orbital at the B-site.

The calculated density of states has a sharp peak at E_F corresponding to $x \sim 0.3$ in $La_{2-x}Sr_xCuO_4$, which is due to a modified type of a saddle point singularity at G_1 point. We have constructed the Fermi surfaces by connecting the points in the k-space at which the Fermi distribution function shows discontinuity based on the calculated conduction band shown in Fig. 20. This Fermi surface is completely different from that of an ordinary Fermi liquid, that calculated by the local density approximation (LDA) and that obtained by a simple folding in the presence of the antiferromagnetic order, as already pointed out by us[36,43], because all the bands except for the upper Hubbard b_{1g}^* band are fully occupied by electrons in the undoped case. The Fermi surface structure are consistent with the experimental results of the angle-resolved photoemission (ARPES) for the superconducting $Bi_2Sr_{0.97}Pr_{0.03}CuO_{6+\delta}$ (Bi 2201) compounds which includes a single CuO_2 layer in a unit cell, like LSCO[107], angle-resolved photoemission for $Bi_2Sr_2CaCu_2O_{8+\delta}$ (Bi 2212) [102,104,105,108,109]. Thus our prediction of a $\sqrt{2} \times \sqrt{2}$

antiferromagnetic local order has a support experimentally.

Possible explanations of the origin for incommensurate peak observed in the inelastic neutron scattering experiment and that for the anomalies in $La_{1.875}Ba_{0.125}CuO_4$, are also explained successfully in connection with the characteristic feature of the Fermi surfaces calculated in this chapter. It should be noticed that though various physical quantities appear in the present theory the values of these quantities are all determined theoretically by cluster calculations and/or band calculations.

Chapter 5.

Properties of Normal State in La$_{2-x}$Sr$_x$CuO$_4$

5-1. Introduction

It has been often said that the normal state properties of La$_{2-x}$Sr$_x$CuO$_4$ are anomalous. The normal state properties of La$_{2-x}$Sr$_x$CuO$_4$ are not only of fundamental interest in themselves, but also important for understanding the nature of the superconductivity, because the feature of electronic structure is often concealed behind the common feature of superconductivity.

Among all, the resistivity shows T-linear dependence down to T_c [44,45,46,47,48,49, 50], which has been explained qualitatively by Micnas *et al.*[113] and Ushio *et al.*[10] in terms of a small two-dimensional hole Fermi surface and a phonon-limited resistivity. Their argument is also valid for the present electronic structure and Fermi surfaces. Since the resistivity is governed by the electron-phonon scattering with small momentum transfer reflecting the small Fermi surface, the linear temperature dependence of the resistivity appears in a wide temperature region. In Section 5-2 we calculate the phonon-limited resistivity after the method in Ref. [10], based on the present effective-one-electron-type-conduction band calculated in chapter 4.

Hall coefficient decreases more rapidly than the $1/x$ behavior, changes its sign from positive to negative around $x=0.3$ and also shows anomalously large T-dependence[44,

45,46,51]. Schimizu and Kamimura [7] have calculated the Sr concentration dependence of the Hall coefficient in the normal state of La$_{2-x}$Sr$_x$CuO$_4$ for zero temperature. Ushio, Schimizu and Kamimura [12] have extended the theory to finite temperatures and showed that the observed anomalous behavior in both x and T dependences of the Hall effect can be explained by the small Fermi surface. In Section 5-3 we apply their theory to the present effective one electron band.

Electronic heat capacity in La$_{2-x}$Sr$_x$CuO$_4$ is interested in its value in superconducting phase [52,53,114]. However we have considered that the electronic heat capacity should be zero in superconducting phase and are here interested in the electronic heat capacity in a normal state. Recently Loram *et al.*[60] have presented a detailed investigation of the normal state electronic specific heat in LSCO using a differential calorimeter. We compare it with the calculated electronic specific heat based on the present electronic structure in Section 5-4. The calculated results of electronic heat capacity agree with that of experimental results by Loram *et al.*[60] in underdoped region.

The thermoelectric power is also calculated for the conduction band. However the large absolute values of thermoelectric power is obtained because of the singular energy dependence of the density of states, the calculated results does not agree so well with the experimental result by Cooper *et al.*[57]. In this context one should take into account that the AF spin correlation length become shorter with increasing temperature and the crossing behavior is expected when the present conduction band with small Fermi surfaces change into the ordinary LDA band structure with large Fermi surfaces. In this chapter we calculate the normal state properties using the present effective one-electron type band structure.

5-2. Resistivity

The temperature dependence of the resistivity in the normal state of $La_{2-x}Sr_xCuO_4$ has been reported by Takagi et al.[44]. It shows a linear temperature dependence above T_c, which has been explained qualitatively by Micnas et al.[113], and later by Ushio and Kamimura[10], in terms of a small two-dimensional hole Fermi surface. In this section the phonon-limited resistivity is calculated from the variational expression for the resistivity of metals[115], by using the energy band expressed by Eq.(4.1). The expression for the resistivity is given by [116],

$$\rho(T) = \frac{A\pi}{2e^2 k_B T} \int\int \omega_q \left| g_{k,k'} \right|^2 \cdot \left[\cosh(\frac{\hbar\omega_q}{k_B T}) - 1 \right]^{-1}$$
$$\times \left[(v_k - v_{k'}) \cdot u \right]^2 \frac{dS_k}{v_k} \frac{dS_{k'}}{v_{k'}}, \qquad (5.1)$$

with

$$A = \left[\int\int (v_k \cdot u)(v_{k'} \cdot u)(v_k \cdot v_{k'}) \frac{dS_k}{v_k} \frac{dS_{k'}}{v_{k'}} \right]^{-1}. \qquad (5.2)$$

Here $g_{k,k'}$ is the electron-phonon matrix element which we have assumed to be $|g_{k,k'}|^2 = (N/2M\omega_q) \cdot (C \cdot q)^2$ in the present calculation with C being a constant whose dimension is energy, $v_k = \partial E_k / \partial k$, $\int dS_k$ denotes an integration over the Fermi surface, $\hbar\omega_q$ is the phonon energy and u is the unit vector in the direction of the external electric field which is parallel to the x-axis. Since the phonon dispersion along the c-axis is small[117], it has been assumed to be two dimensional and may be expressed by $\hbar\omega_q = v_s \cdot q_\perp = v_s \cdot \sqrt{q_x^2 + q_y^2}$, with the sound velocity $v_s = 5 \times 10^5$ cm/s [117]. The calculated results are shown in Fig. 27. Because the resistivity is governed by the electron-phonon scattering with small [Fig. 27] momentum transfer due to the small Fermi surface, a linear temperature dependence of the resistivity appears in a wide temperature region, consistent with the experimental data of resistivity in normal state of $La_{2-x}Sr_xCuO_4$ by Takagi et al.[44].

For the values of x above 0.2, the experimental data of resistivity deviates upward
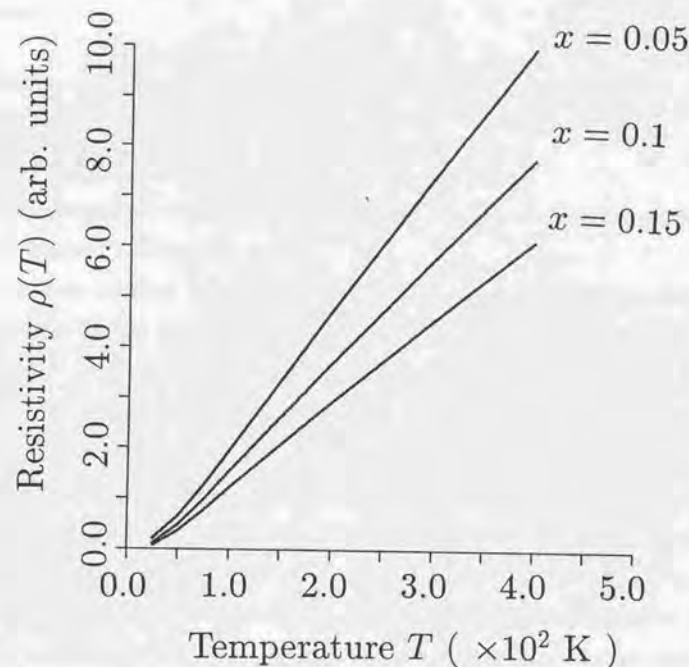
80

Figure 27: The calculated temperature dependence of the resistivity for LSCO with various hole concentration.

from the linear dependence in a low temperature region. The discrepancy may also be removed by taking into account the decrease of correlation length and the resultant large Fermi surface of LDA band in the well-over-doped region. The arguments in this section is also valid for a small Fermi surface obtained by a simple folding in the presence of the AF order.

5-3. Hall effect

The Hall coefficient R_H in the normal state of LSCO for finite temperatures can be calculated from the formula given in Schimizu and Kamimura's paper (Eq.(11) in Ref. [7]), by substituting $-\frac{\partial f}{\partial E_k}$ for the δ-function [12,118]. Its expression is given in Ref. [12] as follows:

$$
R_H = \frac{4\pi^3}{ec} \frac{\int_{BZ} dk \frac{\partial E_k}{\partial k_x} \left[\frac{\partial E_k}{\partial k_x} \frac{\partial^2 E_k}{\partial k_y^2} - \frac{\partial E_k}{\partial k_y} \frac{\partial^2 E_k}{\partial k_x \partial k_y} \right] (-\frac{\partial f}{\partial E_k})}{\left[\int_{BZ} dk \left(\frac{\partial E_k}{\partial k_x} \right)^2 (-\frac{\partial f}{\partial E_k}) \right]^2}, \tag{5.3}
$$

where E_k represents the energy dispersion of the effective one-electron type conduction band calculated in chapter 4.

Let us calculate both the Sr concentration dependence and the temperature dependence of R_H, using the effective-one-electron-type-band structure calculated in chapter 4. In doing so we note that the calculated Fermi surfaces change drastically at $x \sim 0.3$, that is, the four flat tubes of the Fermi surface calculated for $x \leq 0.3$ in Fig. 23 merge into one " large electron-type Fermi surface " shown in Fig. 29 for $x \geq 0.3$. Even in the concentration region $x \leq 0.3$ this electron-type Fermi surface contributes to Hall effect at finite temperature and leads to the large T-dependence of R_H and to the negative value of Hall coefficient R_H shown for $0.25 \leq x \leq 0.3$ at 80K in Fig. 28. The results thus calculated are given in Fig. 28, where the experimental data by Takagi et al.[44] are also shown for comparison. It is seen from this figure that the calculated Sr concentration dependence of R_H for T=80K and 300K agree with the experimental results by Takagi et al fairly well.

Fig. 29

Fig. 28

The calculated Fermi surfaces are valid for the hole concentration from underdoped ($x \leq 0.15$) to overdoped region ($0.15 \leq x \leq 0.2$), but not valid for well over-doped region ($x \geq 0.2$), because the concept of the renormalized band structure shown in Fig. 20 may
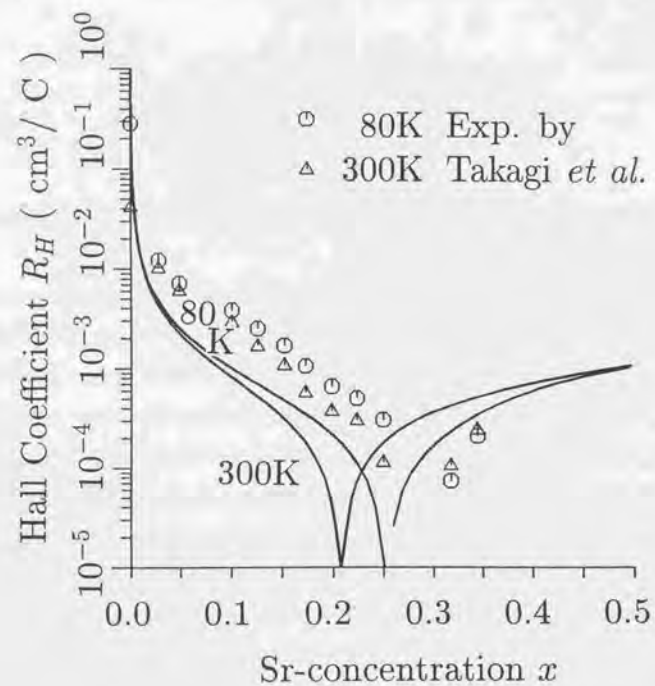
Figure 28: The calculated concentration dependence of the Hall coefficient R_H for $T=80$K and $T=300$K, together with the experimental results by Takagi et al.[26]
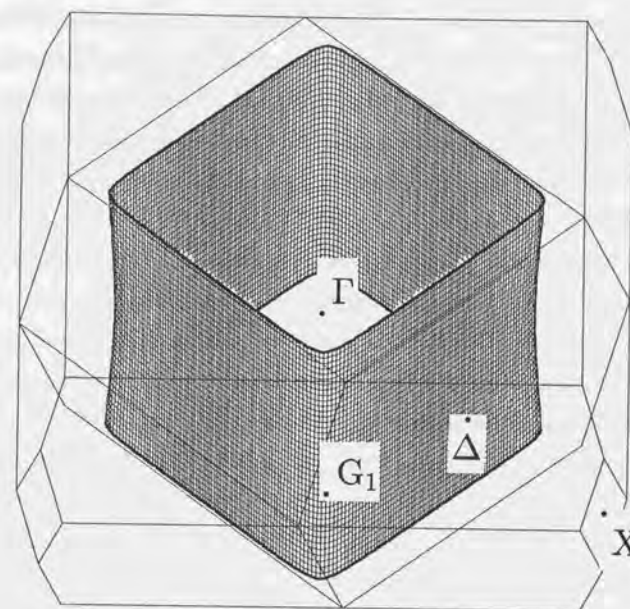
FERMI SURFACE (X=0.35)

Figure 29: The Fermi surface for $x = 0.35$ calculated for the #1 band. Here two kinds of Brillouin zones are also shown. One at the outermost part is the ordinary Brillouin zone and the inner part is the folded Brillouin zone for the antiferromagnetic unit cell in LSCO. Here the k_x axis is taken along $\overline{\Gamma G_1}$, corresponding to the z-axis (the Cu - O - Cu direction) in a real space.

not hold for the well-over-doped region, when the spin-correlation length becomes smaller than the band mean free path of carriers and the conduction band calculated in chapter 4 change into the ordinary LDA band. Therefor the calculated results in Fig. 28 are valid only for $x \leq 0.2$ and the Hall coefficient shows the crossing from the present calculated value in Fig. 28 to that of LDA band.

The Hall coefficient at high temperature, $T \gtrsim 600K$, observed by Nishikawa *et al.*, Takeda *et al.* and Sera *et al.*[119,120,121] is small and insensitive to the doping concentration. This suggests that a small Fermi surface changes into a large Fermi surface of ordinary LDA band by the temperature dependence of the local antiferromagnetic order. In other words the present conduction band in local AF order changes into the ordinary LDA band structure by the disappearance of local antiferromagnetic order due to localized spin at $T \gtrsim 200K$.

The fact that the decrease of R_H shows $1/x$ behavior in the low hole concentration region, is also derived from a small Fermi surface obtained by a simple folding in the presence of AF order. On the other hand, the more rapid decrease of R_H than $1/x$ behavior and the anomalously large T-dependence can not be explained by a simple folding of b_{1g} band in the presence of AF order.

5-4. Electronic heat capacity

As is well known, the electronic heat capacity is linearly proportional to T at sufficiently low temperature in normal state, and expressed as γT . In superconducting phase the parameter γ approaches to zero, because of the energy gap of superconductivity. In La$_{2-x}$Sr$_x$CuO$_4$, the electronic heat capacity attracted much interest because non zero electronic heat capacity is reported in superconducting phase at the early time. Recent experimental results, however, have reported a smaller value of electronic heat capacity in superconducting phase[53], so that the electronic heat capacity has been thought to be zero in the superconducting phase. We think the electronic heat capacity to be zero in the superconducting phase and our main interest in this section is the electronic heat capacity in the normal state. The parameter γ at 0K is given by the following expression,

$$\gamma = \frac{1}{3}\pi^2 \rho(\mu) k_B^2, \tag{5.4}$$

where $\rho(\mu)$ denotes the density of states at Fermi energy μ. Now we calculate the electronic heat capacity by this equation based on the calculated renormalized energy band.

The x dependence of the electronic specific heat is calculated based on the electronic structure derived in chapter 4 and compared with that observed by Loram *et al.*[60]. We Fig. 30 have calculated the normal state electronic specific heat at 50K by using the density of states which gets blunted by Fermi distribution function at 50K. In Fig. 30 we show the electronic specific heat thus calculated. In this figure the experimental results by Loram *et al.* are also shown by crosses for comparison. We notice in this figure that the theoretical results coincide well with experimental results in the concentration region $x \leq 0.2$, while the magnitude of the calculated electronic specific heat is larger than observed one around $x = 0.25$. Since the spin correlation length decreases sharply in the well-over-doped region above $x \sim 0.2$ and becomes smaller than the band mean free path of carriers, the concept of the effective one-electron type band structure shown in Fig. 20 may not hold for the well-over-doped region.
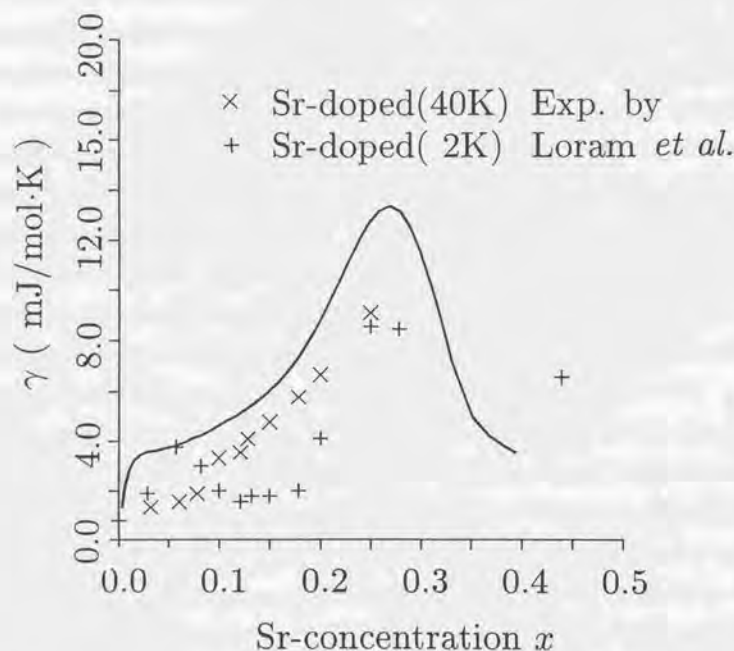
Figure 30: The electronic specific heat of LSCO as a function of hole concentration x. The solid lines are the calculated one of the #1 band in the renormalized band structure[23,25] while the crosses are the experimental data by Loram *et al.*[48]

5-5. Thermoelectric power

Thermoelectrical power shows, as is well known, anomalously large absolute values for the Sr concentration region $x \leq 0.2$ and the temperature dependence is rather flat in a wide temperature region[57,58,59]. It is also worth while to notice that the sign of thermoelectric power is still positive at the Sr concentration region where the sign of the Hall coefficient is negative. The most simple expression for the thermoelectric power S is obtained by putting the total electric and thermal currents to be zero and by using the Boltzmann equation as follows,

$$S = -\frac{\sigma_Q}{\sigma_{xx}} \tag{5.5}$$

$$\sigma_Q = \frac{e\tau}{4\pi^3} \int_{\text{BZ}} d\boldsymbol{k} \left(\frac{\partial E_{\boldsymbol{k}}}{\partial k_x}\right)^2 \left[\frac{E}{T} + T\frac{d}{dT}\left(\frac{\mu}{T}\right)\right]\left(-\frac{\partial f}{\partial E_{\boldsymbol{k}}}\right) \tag{5.6}$$

We calculate the thermoelectric power by this expression, assuming the conduction band in chapter 4. The calculated concentration dependence of thermoelectric power S is shown in Fig. 31. The calculated thermoelectric power agrees fairly well with the experimental data by Cooper *et al.*[57]. It is worth while to notice that in the present calculation the large absolute values of thermoelectric power is obtained because of the singular energy dependence of the density of states and the resultant large T-dependence of chemical potential μ.

However the temperature dependence of thermoelectric power does not show quantitative agreement with experimental result by Cooper *et al.*[57]. The disagreement may be ascribed to the disappearance of the local AF spin correlation with increasing temperature and also to the crossing from the present conduction band to the ordinary LDA band structure with large Fermi surface, at the hole concentration, $x \sim 0.2$.
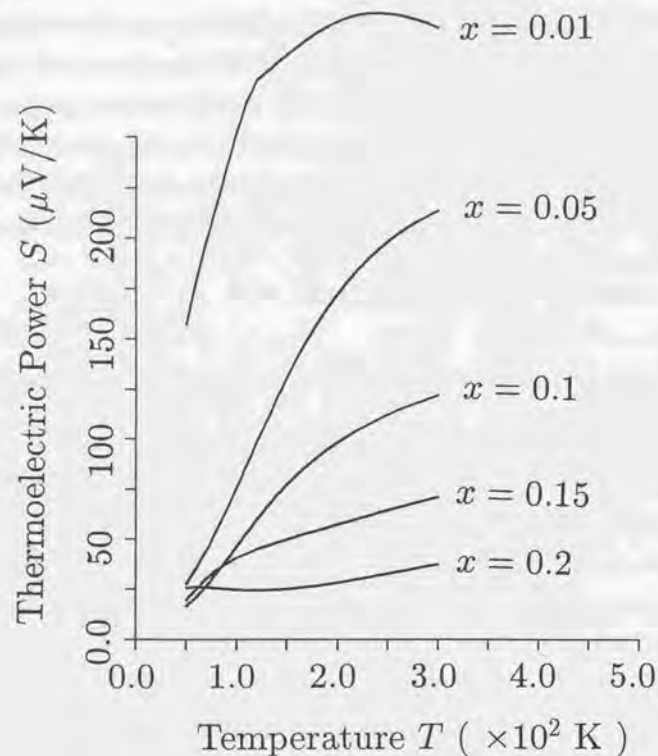
Figure 31: The calculated temperature dependence of thermoelectric power $S(T)$.

Chapter 6.

Electron-Phonon Interaction of $La_{2-x}Sr_xCuO_4$

6-1. Introduction

As regards the symmetry of Cooper pairs, various experiments such as NMR, tunneling spectroscopy and others have been done, and most of the experiments support d-wave symmetry. Recent experiments of high accuracy photo-emission spectroscopy[104] suggest that the superconductivity gap practically disappears in the planer direction which is in 45° from a- and b-axes. From this fact, the symmetry of Cooper pair is restricted to either extended s-wave or $d_{x^2-y^2}$-symmetry. In order to distinguish these two symmetries we need to know the phase of the gap rather than the magnitude of the gap. Such experiments was done by use of Josephson junction and it is now generally believed that Cooper pairs of hole-doped high T_c cuprates have $d_{x^2-y^2}$-symmetry from π-junction experiments[122].

More attention has been paid recently to the electron-phonon interaction, since non-zero isotope effect was reported by Crawford[26,27] (i.e. $\alpha \sim 0.1 \sim 0.8$, $T_c \sim M^{-\alpha}$, where M is the atomic mass of oxygen), suggesting the phonon mechanism of high T_c superconductivity, and Kamimura et al.[36,37,38,39,40] showed that even the electron-phonon mechanism lead to the d-wave pairing, in case where the local AF order existed in cuprates. They have shown that the electron-phonon interactions which scatter pairs of

electrons from one pair state $(k \uparrow, -k \downarrow)$ to a different state $(k' \uparrow, -k' \downarrow)$ are repulsive for some combinations of (k, k') and attractive for other combinations, while that contains the processes of virtual emissions and absorptions of various modes of phonons by a single electron are always attractive. This leads to the d-wave symmetry of superconductivity. In the following sections we will discuss electron-phonon interaction, calculate the spectral function, clarify the occurrence of the d-wave symmetry and calculate the transition temperature T_c in LSCO, by using the electronic structure calculated in Chapter 4

6-2. The Spectral Functions, $\alpha^2 F_{\uparrow\uparrow}(\Omega, k, k')$ and $\alpha^2 F_{\uparrow\downarrow}(\Omega, k, k')$

All relevant properties of the electron-phonon systems, including superconductivity, are derived from the electron-phonon spectral function $\alpha^2 F$, which is defined as follows,

$$\alpha^2 F_{\uparrow\uparrow}(\Omega, k, k') = \rho(E_F) \sum_{\gamma} \frac{V_{\uparrow}^{\gamma}(k, k') V_{\uparrow}^{\gamma}(-k, -k')}{2\omega_q^{\gamma}} \delta(\Omega - \omega_{k'-k}^{\gamma}), \qquad (6.1)$$

$$\alpha^2 F_{\uparrow\downarrow}(\Omega, k, k') = \rho(E_F) \sum_{\gamma} \frac{V_{\uparrow}^{\gamma}(k, k') V_{\uparrow}^{\gamma}(-k, -k')}{2\omega_q^{\gamma}} \delta(\Omega - \omega_{k'-k}^{\gamma}). \qquad (6.2)$$

Here $\alpha^2 F_{\uparrow\uparrow}(\Omega, k, k')$ and $\alpha^2 F_{\uparrow\downarrow}(\Omega, k, k')$ are the spectral functions which are related to the processes of virtual emission and absorption of various modes of phonons by the interaction with a single electron and the scattering processes of a pair of electrons from a pair state $(k \uparrow, -k \downarrow)$ to a different pair state $(k' \uparrow, -k' \downarrow)$, respectively. Further $\rho(E_F)$ is the density of states at the Fermi energy. The electron-phonon interaction matrix element between the k and k' states with spin σ, $V_{\sigma}^{\gamma}(k, k')$, is defined by

$$H_{e-p} = \sum_{Kkk'q\gamma\sigma} \frac{V_{\sigma}^{\gamma}(k, k')}{\sqrt{N\omega_q^{\gamma}}} a_{k\sigma}^{\dagger} a_{k'\sigma} \left(b_{q\gamma} + b_{-q\gamma}^{\dagger}\right) \delta(k - k' - q - K), \qquad (6.3)$$

where $b_{q\gamma}$ is an annihilation operator of phonon mode γ with momentum q, ω_q^{γ} the phonon frequency of the wave vector q in the AF Brillouin zone, N the total number of AF unit cells in a crystal, and $\delta(k - k' - q - K)$ takes the value 1 only when $k - k' - q$ coincides with a reciprocal lattice vector of the AF unit cell, K, and 0 otherwise. The spectral function $\alpha^2 F_{\uparrow\uparrow}(\Omega, k, k')$ causes a mass enhancement of electron states near the Fermi surface and a finite lifetime of quasi-particle states. On the other hand, the spectral function $\alpha^2 F_{\uparrow\downarrow}(\Omega, k, k')$ contributes to the formation of the Cooper-pair. These two kinds of spectral functions are different from each other in the present case due to the fact that the wave function for up-spin carriers differs from that for down-spin carriers, although they are the same in the ordinary case. Frequently this electron-phonon spectral function

is averaged over either one of k and k' or both of the k and k' values in the electron states (k, k') on the Fermi surface, as is shown below,

$$\alpha^2 F_{\uparrow\downarrow}(\Omega, k) = \frac{1}{\rho(E_F)} \sum_{k'} \alpha^2 F_{\uparrow\downarrow}(\Omega, k, k') \delta(E_{k'}^0 - E_F), \tag{6.4}$$

$$\alpha^2 F_{\uparrow\downarrow}(\Omega) = \frac{1}{\rho(E_F)^2} \sum_{kk'} \alpha^2 F_{\uparrow\downarrow}(\Omega, k, k') \delta(E_k^0 - E_F) \delta(E_{k'}^0 - E_F). \tag{6.5}$$

In the present paper we pay attention to the spectral function defined on the Fermi surface and averaged over k_z-axis. This spectral function is denoted by $\alpha^2 F_{\uparrow\downarrow}(\Omega, \theta, \theta')$, which is defined as follows,

$$\begin{aligned}
\alpha^2 F_{\uparrow\downarrow}(\Omega, \theta, \theta') =\ & \frac{1}{\rho(E_F)^2 N} \sum_{kk'q} \alpha^2 F_{\uparrow\downarrow}(\Omega, k, k') \\
& \times \delta(k - k' - q - K) \delta(E_k^0 - E_F) \delta(E_{k'}^0 - E_F) \\
& \times \delta(\theta - \tan^{-1} \frac{k_y}{k_x}) \delta(\theta' - \tan^{-1} \frac{k_y'}{k_x'}).
\end{aligned} \tag{6.6}$$

Here $\rho(E_F)$ and E_k^0 are the density of states of hole carriers at the Fermi energy and the energy of the renormalized band dispersion at a wave-vector k, respectively, both of which have been calculated in Chapter 4. Following the method of Motizuki *et al.*[99,100,101], we will derive the expression of a spectral function for a tight binding model in the next section.

6-3 Electron-Phonon Interaction in a Tight Binding Model

In this section we describe the formalisms of how to calculate the spectral functions based on the renormalized tight binding Hamiltonian given in Chapter 4. With the use of the electron-phonon coupling constant $V_\sigma^\gamma(k, k')$ defined in Eq (6.3), the momentum-dependent spectral function for a singlet Cooper pair, $\alpha^2 F_{\uparrow\downarrow}(\Omega, \theta, \theta')$, is expressed as follows,

$$\begin{aligned}
\alpha^2 F_{\uparrow\downarrow}(\Omega, \theta, \theta') =\ & \frac{1}{\rho(E_F)} \sum_{kk'q} \sum_\gamma \frac{V_\uparrow^\gamma(k, k') V_\downarrow^\gamma(-k, -k')}{2N \omega_q^\gamma} \\
& \times \delta(k - k' - q - K) \delta(E_k^0 - E_F) \delta(E_{k'}^0 - E_F) \delta(\Omega - \omega_{k'-k}^\gamma) \\
& \times \delta(\theta - \tan^{-1} \frac{k_y}{k_x}) \delta(\theta' - \tan^{-1} \frac{k_y'}{k_x'}).
\end{aligned} \tag{6.7}$$

In the present thesis we calculate the momentum-dependent spectral function by averaging with respect to phonon frequency ω_q^γ; in other words by replacing $\delta(\Omega - \omega_{k'-k}^\gamma)$ by the phonon density of states $P(\Omega)$. The obtained expression is given as,

$$\alpha^2 F_{\uparrow\downarrow}(\Omega, \theta, \theta') = \rho(E_F) N \sum_\gamma \frac{\langle V_\uparrow^\gamma(kk') V_\downarrow^\gamma(-k - k') \rangle_{\text{av.}}}{2\Omega} P(\Omega). \tag{6.8}$$

Here $\langle \cdots \rangle_{\text{av.}}$ means the average over k_z and k_z' on the Fermi surfaces, where $k_y/k_x = \tan\theta$ and $k_y'/k_x' = \tan\theta'$.

Now we calculate the change of the energy bands when the ions are displaced by a small amount from their equilibrium positions $R_{l\mu}$, $\delta R_{l\mu}$. In calculating the energy bands for a displaced structure we adopt the Fröhlich approach that one uses the atomic wave functions which move rigidly with ions. Therefore the basis function in the displaced structure becomes $\varphi_a(r - R_{l\mu} - \delta R_{l\mu})$ and the Bloch function in the displaced structure

is constructed as follows,

$$\Phi_{\mu a \mathbf{k}}(\mathbf{r}) = \frac{1}{\sqrt{N}} \sum_l e^{i\mathbf{k}\cdot\mathbf{R}_{l\mu}} \varphi_a(\mathbf{r} - \mathbf{R}_{l\mu} - \delta\mathbf{R}_{l\mu}), \tag{6.9}$$

where $\mathbf{R}_{l\mu} = \mathbf{R}_l + \boldsymbol{\tau}_\mu$ represents the position of the μ-th ion in the l-th unit cell, $\boldsymbol{\tau}_\mu$ the position of the μ-th ion within the unit cell, N the total number of the unit cells in a crystal, $\mathbf{k}$ a wave vector, and a specifies an atomic orbital. Then the matrix elements of the Hamiltonian is defined by

$$H_{\mu a \nu b}(\mathbf{k}, \mathbf{k}') = \langle \Phi_{\mu a \mathbf{k}} | \mathcal{H}_e | \Phi_{\nu b \mathbf{k}'} \rangle, \tag{6.10}$$

where $\mathcal{H}_e$ represents the effective one-electron Hamiltonian derived in Chapter 4. This Hamiltonian matrix is expressed by inserting Eq.(6.9) into Eq.(6.10) as follows;

$$H_{\mu a \nu b}(\mathbf{k}, \mathbf{k}') = \sum_{l-l'} e^{-i\mathbf{k}\cdot\mathbf{R}_{l\mu}} e^{i\mathbf{k}'\cdot\mathbf{R}_{l'\nu}} H_{l\mu a, l'\nu b}, \tag{6.11}$$

where

$$H_{l\mu a, l'\nu b} = \langle \varphi_a(\mathbf{r} - \mathbf{R}_{l\mu} - \delta\mathbf{R}_{l\mu}) | \mathcal{H}_e | \varphi_b(\mathbf{r} - \mathbf{R}_{l'\nu} - \delta\mathbf{R}_{l'\nu}) \rangle. \tag{6.12}$$

The matrix element $H_{l\mu a, l'\nu b}$ is a function of $\mathbf{R}$ which is the difference between the position vectors of the two ions. In the following we calculate the renormalized energy bands and expand them in terms of the atomic displacements $\delta\mathbf{R}_{l\mu}^\alpha$ or their Fourier transformations $u_{\mathbf{q}\mu}^\alpha$ defined by,

$$\delta\mathbf{R}_{l\mu}^\alpha = \frac{1}{\sqrt{N}} \sum_q e^{i\mathbf{q}\mathbf{R}_{l\mu}} u_{\mathbf{q}\mu}^\alpha, \tag{6.13}$$

where α indicates x, y and z. By expanding the energy bands up to the first order in $\delta\mathbf{R}_{l\mu}^\alpha$ or $u_{\mathbf{q}\mu}^\alpha$, the Hamiltonian matrix element $H_{\mu a \nu b}(\mathbf{k}, \mathbf{k}')$ is expressed as

$$H_{\mu a \nu b}(\mathbf{k}\mathbf{k}') = H_{\mu a \nu b}^0(\mathbf{k})\delta_{\mathbf{k}\mathbf{k}'} + \sum_q \sum_{\mu'\alpha} \dot{T}_{\mu'}^\alpha(\mu a \mathbf{k}, \nu b \mathbf{k}') u_{\mathbf{q}\mu'}^\alpha \delta_{\mathbf{k}-\mathbf{q},\mathbf{k}'}. \tag{6.14}$$

Here $H_{\mu a \nu b}^0(\mathbf{k})$ is the Hamiltonian matrix element for an undistorted structure and $\dot{T}_{\mu'}^\alpha(\mu a \mathbf{k}, \nu b \mathbf{k}')$ is a quantity related to the derivative of a transfer interaction or an on-site energy with regard to a displacement. Definition of $\dot{T}_{\mu'}^\alpha(\mu a \mathbf{k}, \nu b \mathbf{k}')$ is given as follows,

$$\dot{T}_{\mu}^\alpha(\mu' a \mathbf{k} \nu' b \mathbf{k}') = \frac{1}{\sqrt{N}}[\delta_{\mu\mu'}T_{\mu' a \nu' b}^\alpha(\mathbf{k}') - \delta_{\mu\nu'}T_{\mu' a \nu' b}^\alpha(\mathbf{k})] \quad \text{for } \mu'a \neq \nu'b,$$

$$\dot{T}_{\mu}^\alpha(\mu' a \mathbf{k} \nu' b \mathbf{k}') = \frac{1}{\sqrt{N}} T_{\mu c \nu' b}^{*\alpha}(\mathbf{k}' - \mathbf{k}) \qquad \text{for } \mu'a = \nu'b, \tag{6.15}$$

where

$$T_{\mu' a \nu' b}^\alpha(\mathbf{k}) = \sum_{l-l'} e^{-i\mathbf{k}\cdot(\mathbf{R}_{l\mu'}-\mathbf{R}_{l'\nu'})} T_{l\mu' a l'\nu' b}^\alpha, \tag{6.16}$$

$$T_{\mu c \nu' b}^{*\alpha}(\mathbf{k}) = \sum_{l-l'} e^{-i\mathbf{k}\cdot(\mathbf{R}_{l\mu}-\mathbf{R}_{l'\nu'})} T_{l\mu c l'\nu' b}^{*\alpha}, \tag{6.17}$$

$$T_{l\mu' a l'\nu' b}^\alpha = \frac{\partial}{\partial R^\alpha} H_{l\mu' a l'\nu' b} \Big|_{\mathbf{R}=\mathbf{R}_{l\mu'}-\mathbf{R}_{l'\nu'}}, \tag{6.18}$$

$$T_{l\mu c l'\mu' a}^{*\alpha}(\mu) = \frac{\partial}{\partial R^\alpha} H_{l'\mu' a l'\mu' a} \Big|_{\mathbf{R}=\mathbf{R}_{l\mu}-\mathbf{R}_{l'\mu'}}. \tag{6.19}$$

Then the electron-phonon interaction in Eq. (6.8) is calculated on a tight binding model as follows;

$$V^\gamma(\mathbf{k}, \mathbf{k} - \mathbf{q}) = \sum_{\mu\alpha} \frac{1}{\sqrt{M_\mu}} \epsilon_{\gamma\mu\alpha}(\mathbf{q}) g_\mu^\alpha(\mathbf{k}\mathbf{k} - \mathbf{q}), \tag{6.20}$$

$$g_\mu^\alpha(\mathbf{k}\mathbf{k}') = \sum_{n\mu'a} \sum_{n'\nu'b} [A^\dagger(\mathbf{k})]_{n\mu'a}[\dot{T}_\mu^\alpha(\mathbf{k}\mathbf{k}')]_{\mu' a \nu' b}[A(\mathbf{k}')]_{\nu' b n'}\epsilon_{\gamma\mu} \tag{6.21}$$

$$\epsilon_\gamma = \quad 1 \quad \cdots \quad \text{for the case where } \gamma \text{ is 1st-mode and thus } \mathbf{q} = \mathbf{k} - \mathbf{k}'$$

$$= -1 \quad \cdots \quad \text{for the case where } \gamma \text{ is 2nd-mode and thus } \mathbf{q} = \mathbf{k} - \mathbf{k}' - \mathbf{K}. \tag{6.22}$$

where $[A(\mathbf{k}')]_{\nu' b n'}$ is the $(\nu' b n')$-th element of the transformation matrix in the undistorted structure, $\epsilon_{\gamma\mu\alpha}(\mathbf{q})$ the polarization vector of μ-th atom for a phonon mode γ with $\alpha = x, y, z$, and $\mathbf{K}$ the reciprocal lattice vector of the AF unit cell. The detailed expressions of the electron-phonon matrix elements at μ-th atom between $\mathbf{k}$ and $\mathbf{k}'$ states are given in Appendix D.

In advance of the calculation of the spectral function, we will explain in Appendix E why the electron-phonon interactions which scatter pairs of electrons from one pair state $(\mathbf{k}\uparrow, -\mathbf{k}\downarrow)$ to a different pair state $(\mathbf{k}'\uparrow, -\mathbf{k}'\downarrow)$ are repulsive for some combinations of $(\mathbf{k}, \mathbf{k}')$ and attractive for others in the present model.

6-4. Calculated Results of the Spectral Function

Following the method of Motizuki *et al.*[99,100,101], we have approximated the band structure numerically calculated in Chapter 4 in a tight binding analytical form, and calculated the spectral function $\alpha^2 F_{\uparrow\downarrow}(\Omega, \theta, \theta')$, by using the expressions of $g_\mu^\alpha(\boldsymbol{k}, \boldsymbol{k}')$ and $V^\gamma(\boldsymbol{k}, \boldsymbol{k}')$ based on the tight binding model which are given in Appendix D. In the present theory, as the origins of the electron-phonon interactions $g_\mu^\alpha(\boldsymbol{k}, \boldsymbol{k}')$ we consider the change of both the transfer interactions and the on-site energies due to the displacement of atoms for each phonon mode[71,117]. The change of the on-site energies has not been taken into account in the treatment of Motizuki *et al.* In the present treatment, the derivatives of transfer integrals between Cu and O in CuO$_2$ plane are taken into account through the derivatives of the Slater Koster parameter, $t_1'(dp\sigma) = dt_1(dp\sigma)/dR = 2.6\text{eV\AA}^{-1}$, calculated by DeWeert *et al.*[97]. As for the effect of the displacement of atoms upon the on-site energies in the tight binding band, we calculate the change of the energies of the $^1A_{1g}$ and $^3B_{1g}$ multiplets, $dE_{A_{1g}}/dR$ and $dE_{B_{1g}}/dR$, by using the calculated results of energy difference with respect to the distance of Cu and apical O by Kamimura and Eto[8]. From the result of Kamimura and Eto we find that $E_{B_{1g}}' \equiv dE_{B_{1g}}/dR = 2.8\text{eV \AA}^{-1}$ and $E_{A_{1g}}' \equiv dE_{A_{1g}}/dR = 2.2 \text{ eV \AA}^{-1}$, where $E_{B_{1g}}$ and $E_{A_{1g}}$ denote the on-site energy of $^3B_{1g}$ and $^1A_{1g}$, respectively.

As examples of the calculated results, we present the calculated results of the spectral | Fig. 32 | functions $\alpha^2 F_{\uparrow\downarrow}(\Omega, \theta, \theta')$ for an A_{1g} phonon mode in Fig. 32(a), that for an E_u phonon mode in Fig. 32(b) and the calculated results of $\alpha^2 F_{\uparrow\uparrow}(\Omega, \theta, \theta')$ for an A_{1g} phonon mode in Fig. 32(c) for La$_{2-x}$Sr$_x$CuO$_4$. The momentum-dependent spectral functions for a singlet

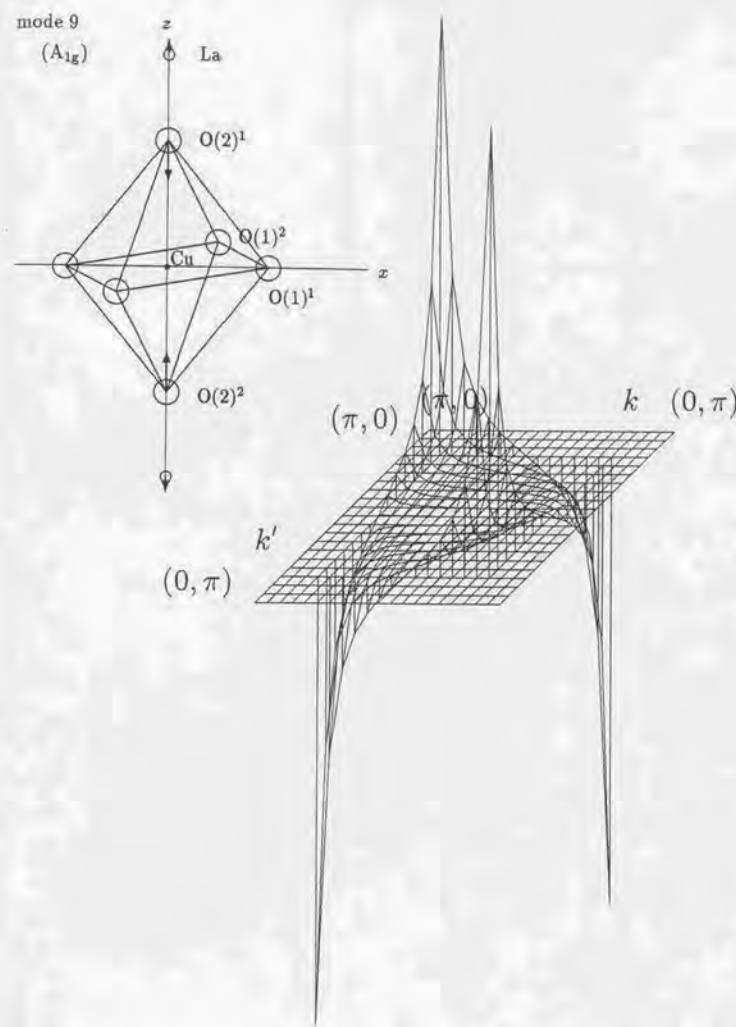**Figure 32:** (a.1) The θ and θ' dependence of the momentum-dependent spectral function $\alpha^2 F_{\uparrow\downarrow}(\Omega, \theta, \theta')$ calculated for an A_{1g} phonon mode shown in the inset of the figure for fixed values of Ω. In this figure $\alpha^2 F_{\uparrow\downarrow}(\Omega, \theta, \theta')$ is shown for $0 \leq \theta \leq \pi/2$ and $0 \leq \theta' \leq \pi/2$
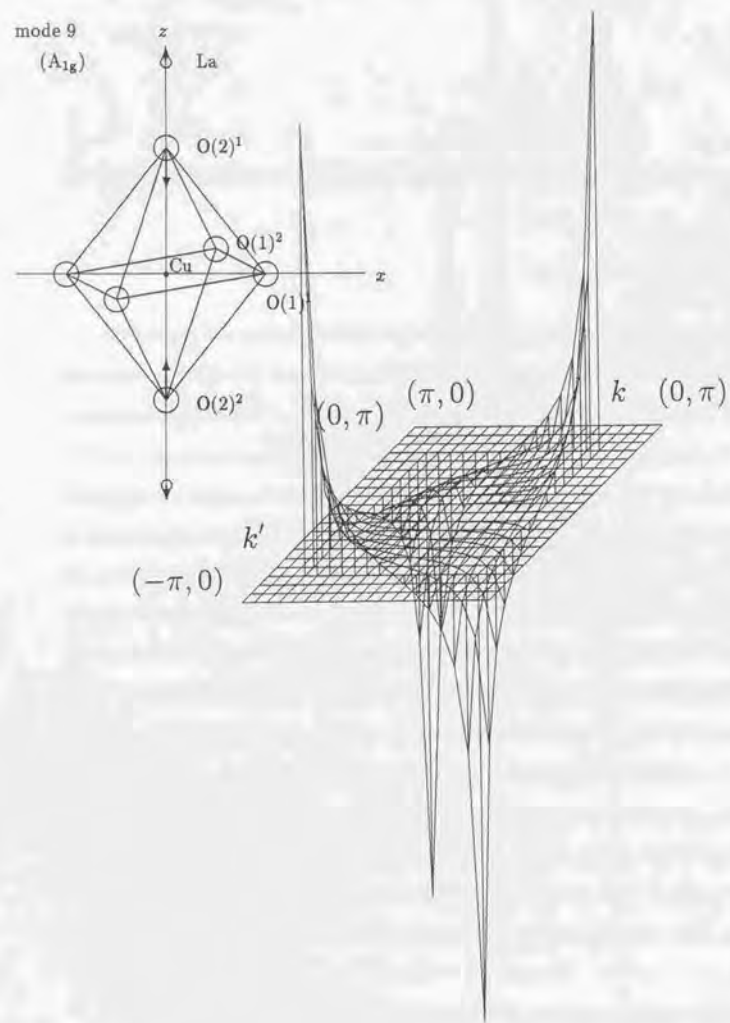
Figure 32: (a.2) The θ and θ' dependence of the momentum-dependent spectral function $\alpha^2 F_{\uparrow\downarrow}(\Omega, \theta, \theta')$ calculated for an A_{1g} phonon mode shown in the inset of the figure for fixed values of Ω. In this figure $\alpha^2 F_{\uparrow\downarrow}(\Omega, \theta, \theta')$ is shown for $\pi/2 \leq \theta \leq \pi$ and $0 \leq \theta' \leq \pi/2$
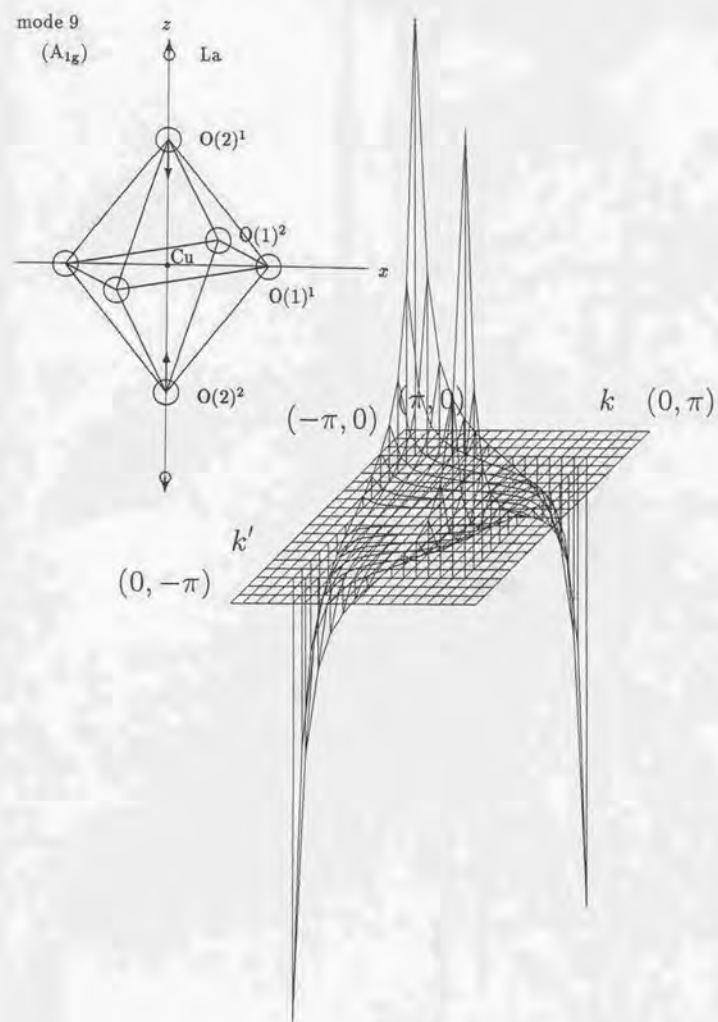
Figure 32: (a.3) The θ and θ' dependence of the momentum-dependent spectral function $\alpha^2 F_{\uparrow\downarrow}(\Omega, \theta, \theta')$ calculated for an A_{1g} phonon mode shown in the inset of the figure for fixed values of Ω. In this figure $\alpha^2 F_{\uparrow\downarrow}(\Omega, \theta, \theta')$ is shown for $\pi \leq \theta \leq 3\pi/2$ and $0 \leq \theta' \leq \pi/2$
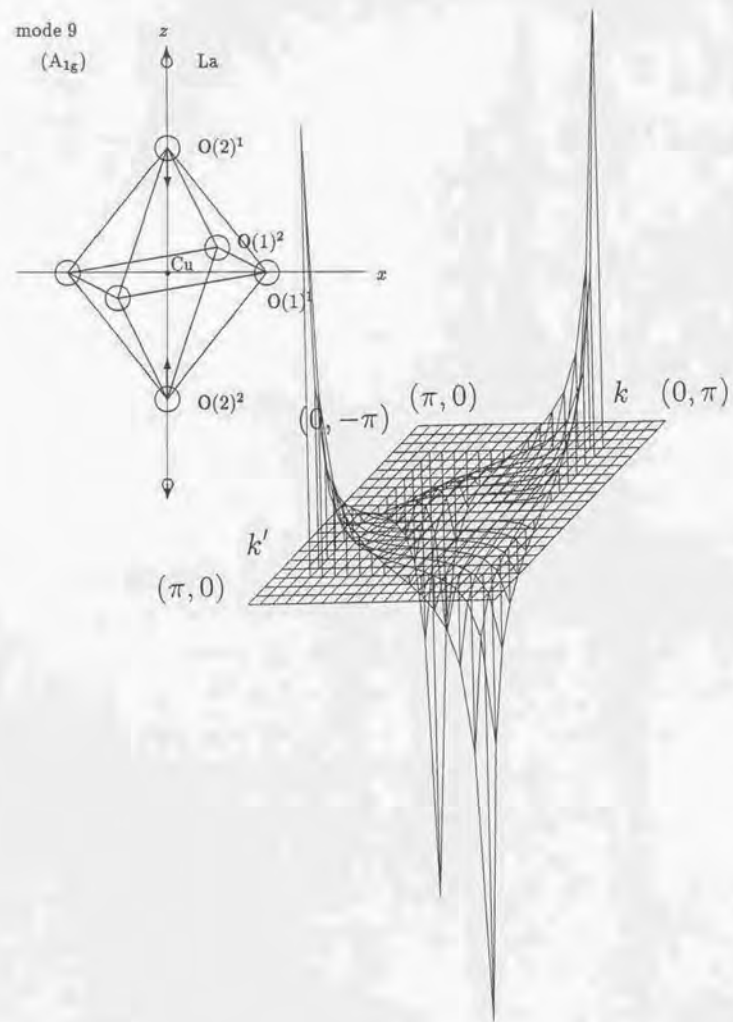
mode 9

(A$_{1g}$)

mode 11

(E$_u$)

Figure 32: (a.4) The θ and θ' dependence of the momentum-dependent spectral function $\alpha^2 F_{\uparrow\downarrow}(\Omega, \theta, \theta')$ calculated for an A$_{1g}$ phonon mode shown in the inset of the figure for fixed values of Ω. In this figure $\alpha^2 F_{\uparrow\downarrow}(\Omega, \theta, \theta')$ is shown for $3\pi/2 \leq \theta \leq 2\pi$ and $0 \leq \theta' \leq \pi/2$
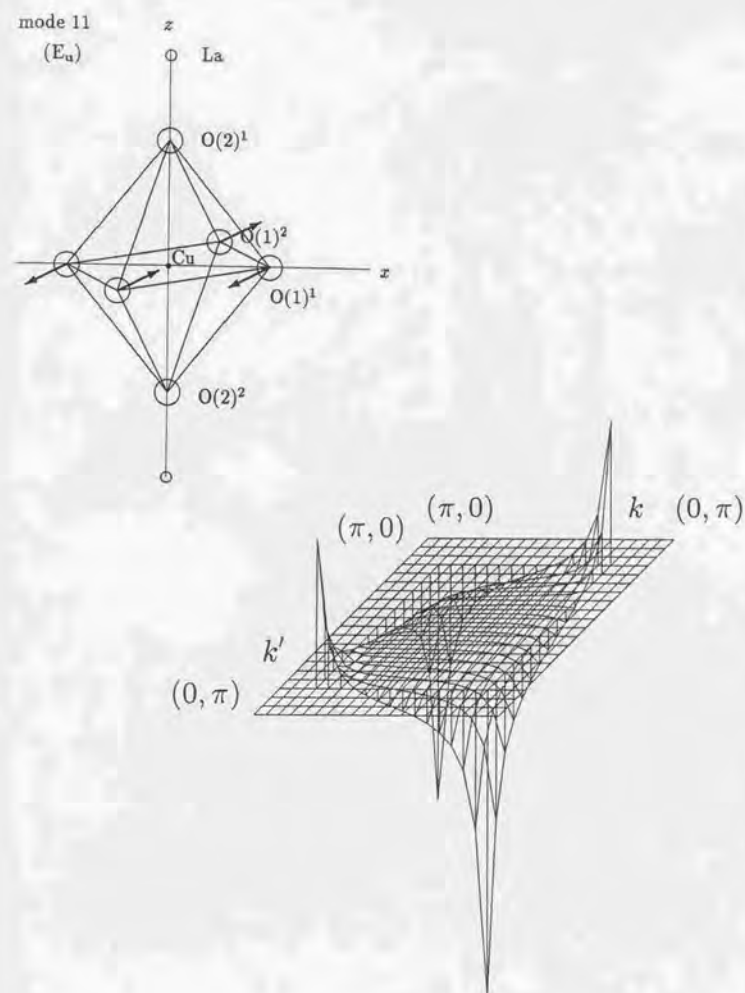
Figure 32: (b.1) The θ and θ' dependence of the momentum-dependent spectral function $\alpha^2 F_{\uparrow\downarrow}(\Omega, \theta, \theta')$ calculated for an E$_u$ phonon mode shown in the inset of the figure for fixed values of Ω. In this figure $\alpha^2 F_{\uparrow\downarrow}(\Omega, \theta, \theta')$ is shown for $0 \leq \theta \leq \pi/2$ and $0 \leq \theta' \leq \pi/2$
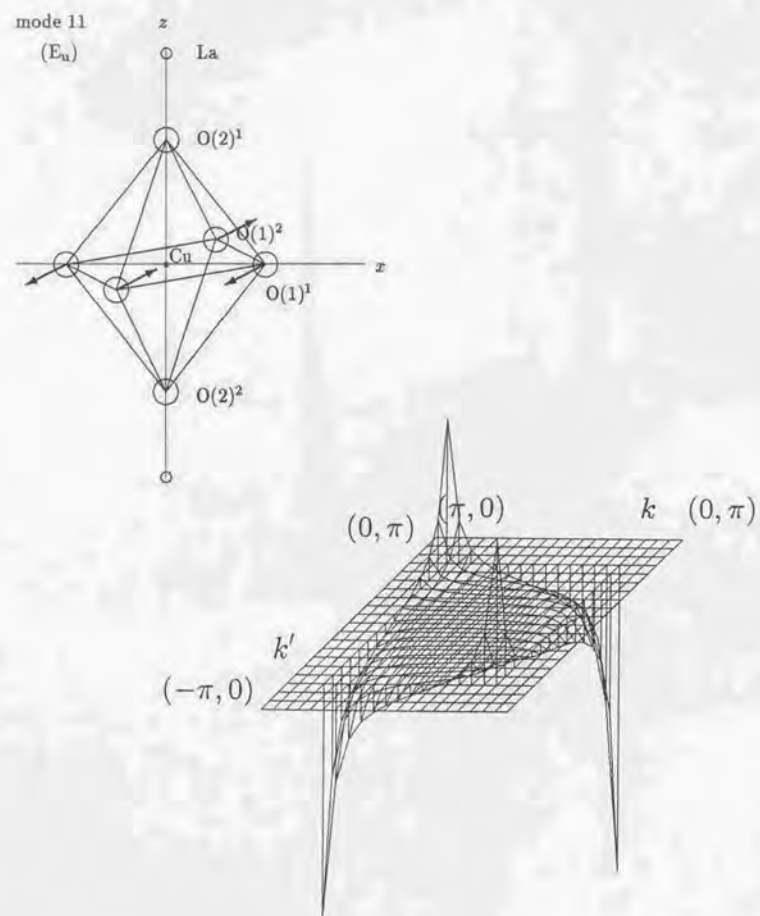
mode 11
(E$_u$)

Figure 32: (b.2) The θ and θ' dependence of the momentum-dependent spectral function $\alpha^2 F_{\uparrow\downarrow}(\Omega, \theta, \theta')$ calculated for an E$_u$ phonon mode shown in the inset of the figure for fixed values of Ω. In this figure $\alpha^2 F_{\uparrow\downarrow}(\Omega, \theta, \theta')$ is shown for $\pi/2 \leq \theta \leq \pi$ and $0 \leq \theta' \leq \pi/2$

mode 11
(E$_u$)

Figure 32: (b.3) The θ and θ' dependence of the momentum-dependent spectral function $\alpha^2 F_{\uparrow\downarrow}(\Omega, \theta, \theta')$ calculated for an E$_u$ phonon mode shown in the inset of the figure for fixed values of Ω. In this figure $\alpha^2 F_{\uparrow\downarrow}(\Omega, \theta, \theta')$ is shown for $\pi \leq \theta \leq 3\pi/2$ and $0 \leq \theta' \leq \pi/2$
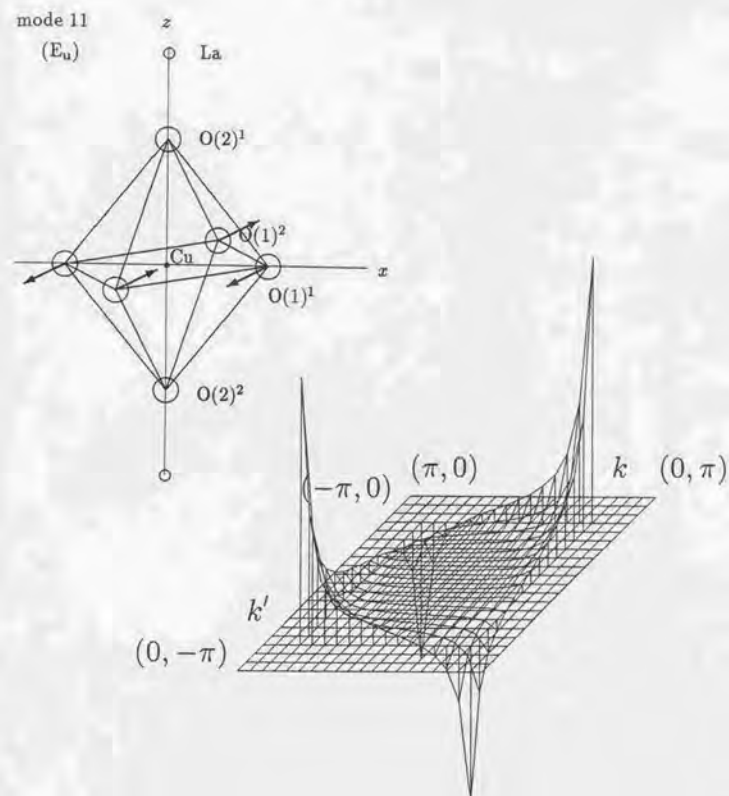
mode 11
(E_u)

mode 9
(A_{1g})

Figure 32: (b.4) The θ and θ' dependence of the momentum-dependent spectral function $\alpha^2 F_{\uparrow\downarrow}(\Omega, \theta, \theta')$ calculated for an E_u phonon mode shown in the inset of the figure for fixed values of Ω. In this figure $\alpha^2 F_{\uparrow\downarrow}(\Omega, \theta, \theta')$ is shown for $3\pi/2 \leq \theta \leq 2\pi$ and $0 \leq \theta' \leq \pi/2$
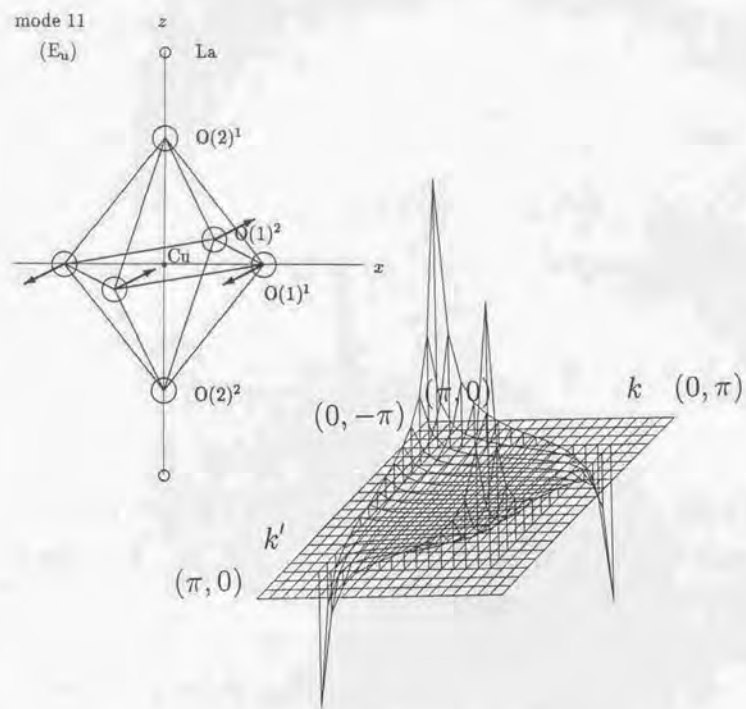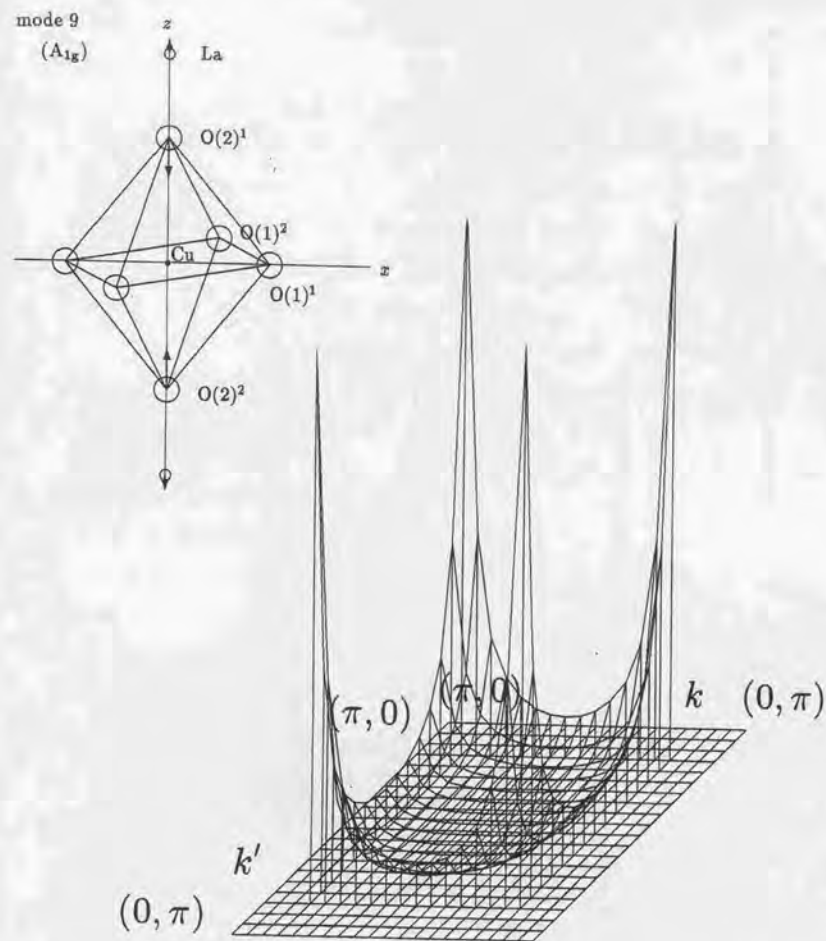
Figure 32:(c1) The θ and θ' dependence of the momentum-dependent spectral function $\alpha^2 F_{\uparrow\uparrow}(\Omega, \theta, \theta')$ calculated for an E_u phonon mode shown in the inset of this figure, for fixed values of Ω. The spectral function $\alpha^2 F_{\uparrow\uparrow}(\Omega, \theta, \theta')$ is shown for $0 \leq \theta \leq \pi/2$ and $0 \leq \theta' \leq \pi/2$.

Figure 32:(c2) The θ and θ' dependence of the momentum-dependent spectral function $\alpha^2 F_{\uparrow\uparrow}(\Omega, \theta, \theta')$ calculated for an E_u phonon mode shown in the inset of this figure, for fixed values of Ω. The spectral function $\alpha^2 F_{\uparrow\uparrow}(\Omega, \theta, \theta')$ is shown for $\pi/2 \leq \theta \leq \pi$ and $0 \leq \theta' \leq \pi/2$

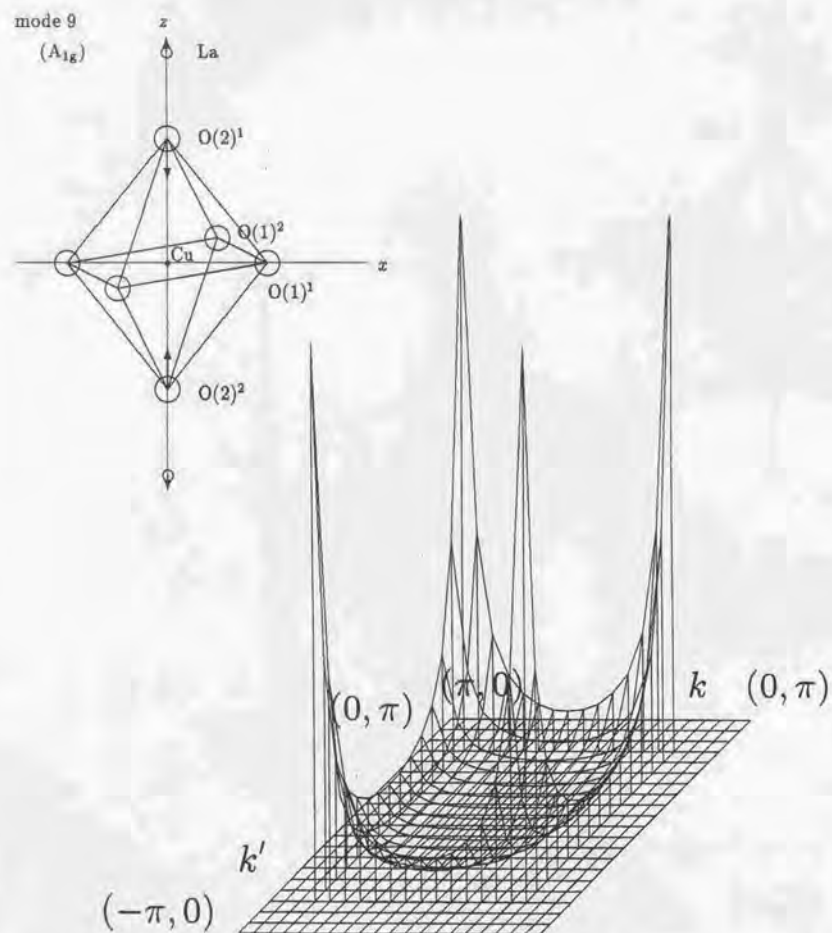**Figure 32:**(c3) The θ and θ' dependence of the momentum-dependent spectral function $\alpha^2 F_{\uparrow\uparrow}(\Omega, \theta, \theta')$ calculated for an E_u phonon mode shown in the inset of this figure, for fixed values of Ω. The spectral function $\alpha^2 F_{\uparrow\uparrow}(\Omega, \theta, \theta')$ is shown for $\pi \leq \theta \leq 3\pi/2$ and $0 \leq \theta' \leq \pi/2$
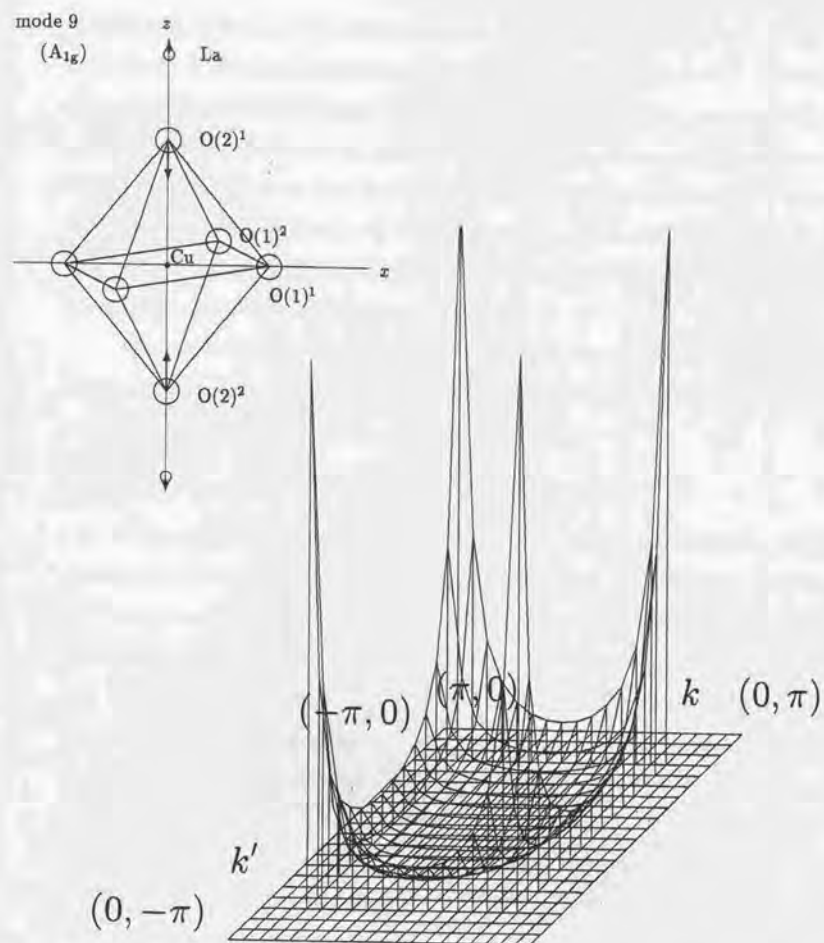
Figure 32:(c4) The θ and θ' dependence of the momentum-dependent spectral function $\alpha^2 F_{\uparrow\uparrow}(\Omega, \theta, \theta')$ calculated for an E_u phonon mode shown in the inset of this figure, for fixed values of Ω. The spectral function $\alpha^2 F_{\uparrow\uparrow}(\Omega, \theta, \theta')$ is shown for $3\pi/2 \leq \theta \leq 2\pi$ and $0 \leq \theta' \leq \pi/2$
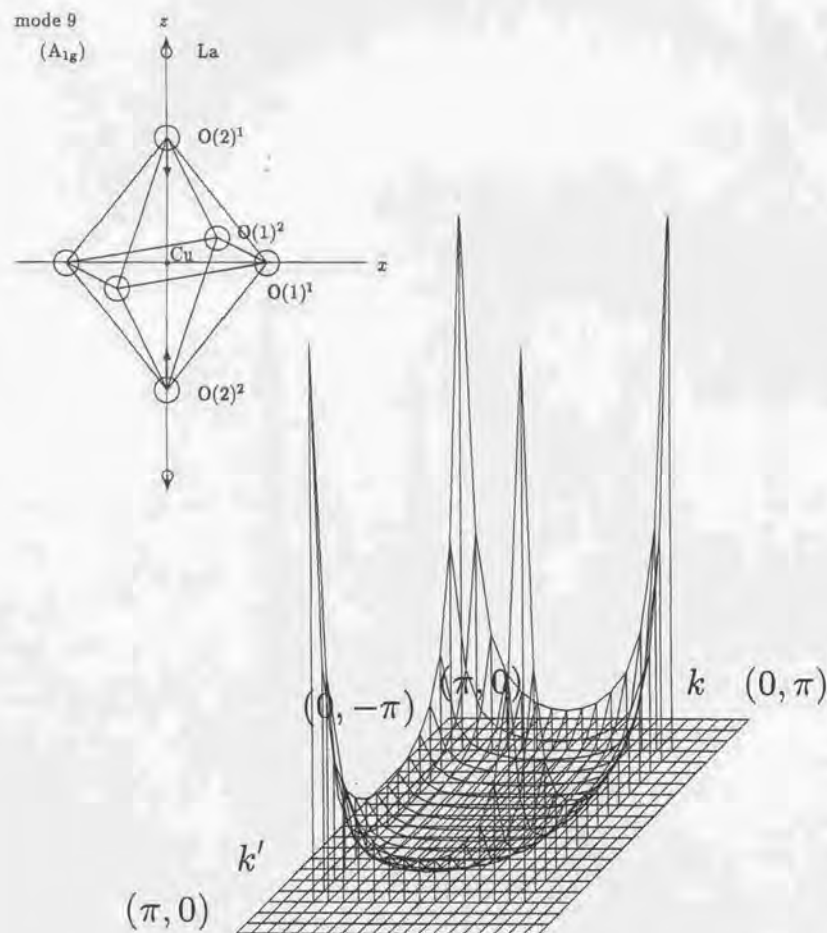
Cooper pair, $\alpha^2 F_{\uparrow\downarrow}(\Omega, \theta, \theta')$, shows a sharp $\boldsymbol{k}$-dependence and a $d_{x^2-y^2}$ symmetry. The sharp peaks of the spectral function at G_1 points $i.e.$ $(\pm\pi/a, 0, 0)$ and $(0, \pm\pi/a, 0)$, are due to the appearance of the van Hove singularity in the density of states (DOS) at G_1 points. The θ-dependence of the spectral functions may be more easily understood from Fig. 33 and Fig. 34, where the calculated results of the spectral functions $\alpha^2 F_{\uparrow\downarrow}$ are shown as a function of θ for fixed values of Ω and θ' for an A_{1g} phonon mode in which the apical oxygens move vertically for a CuO_2 plane (Fig. 33) and for an E_u phonon mode in which the oxygens move within a CuO_2 plane (Fig. 34).

Then, by summing up the contributions from all the phonon modes in Table 6 to the spectral function, we have calculated s-wave component of spectral function $\alpha^2 F_{\uparrow\downarrow}^{(0)}(\Omega)$ and d-wave component $\alpha^2 F_{\uparrow\downarrow}^{(2)}(\Omega)$, which are defined as,

$$\alpha^2 F_{\uparrow\downarrow}(\Omega, \theta, \theta') = \frac{1}{2\pi} \sum_{n=0}^{\infty} \alpha^2 F_{\uparrow\downarrow}^{(n)}(\Omega) \cos n\theta \cos n\theta'. \tag{6.23}$$

As will be explained in Section 6-5 and Appendix F, the d-wave component $\alpha^2 F_{\uparrow\downarrow}^{(2)}(\Omega)$ contributes to the appearance of d-wave superconductivity. As a result we find that, for phonon modes in which oxygen and copper ions vibrate within a CuO_2 plane such as a breathing mode, the d-wave component in the spectral function is negative (repulsive) and the s-wave component is very small. Thus the in-plane modes do not contribute to the formation of Cooper pairs. On the other hand, for the phonon modes in which the apical oxygen ions move vertically for CuO_2 plane, the d-wave component of the spectral function, $\alpha^2 F_{\uparrow\downarrow}^{(2)}(\Omega)$, has a positive (attractive) sign. In Fig. 35 we show the calculated results of the total contribution for the d-wave components of the spectral function, $\alpha^2 F_{\uparrow\downarrow}^{(2)}(\Omega)$, from all the phonon modes of LSCO. We can obtain the value of electron-phonon coupling constant for d-wave pairing, λ_d by integrating the positive part of the calculated d-wave component of the spectral function $\alpha^2 F_{\uparrow\downarrow}^{(2)}(\Omega)$ over the phonon frequency Ω by the following expression.

$$\lambda_d = 2 \int_0^\infty \frac{\frac{1}{2}\alpha^2 F_{\uparrow\downarrow}^{(2)}(\Omega)}{\Omega} d\Omega. \tag{6.24}$$

The value of λ_d thus calculated for $x = 0.15$ is 1.96. From this we find that LSCO is the superconductor of a strong coupling. We also show the calculated results of the total
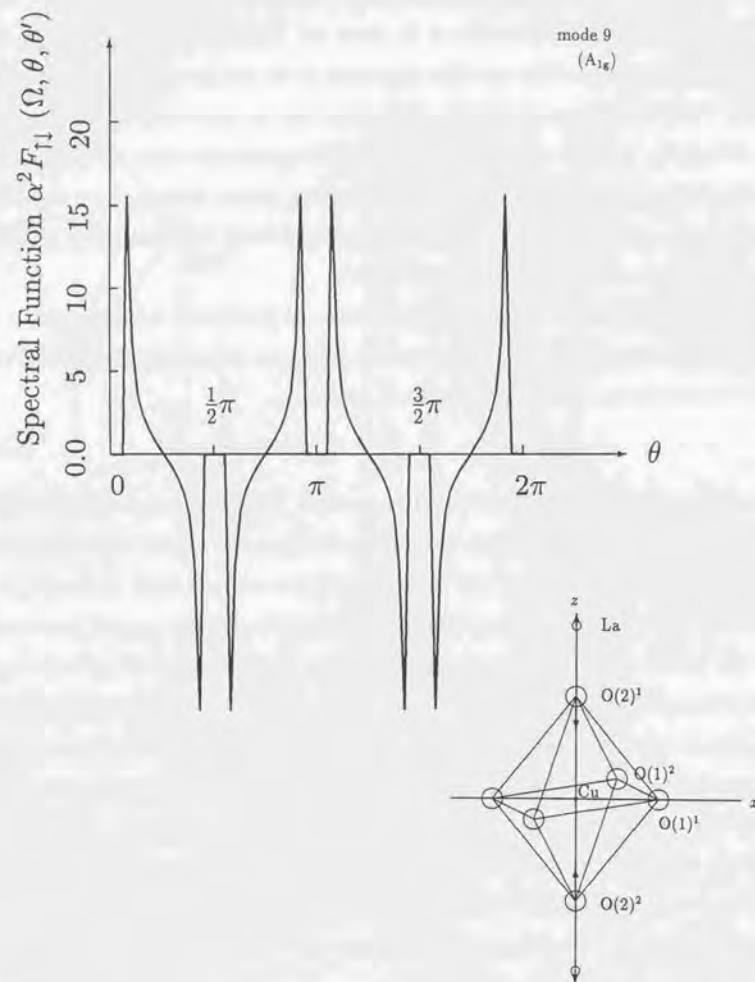
111

Figure 33: The θ dependence of the momentum-dependent spectral function $\alpha^2 F_{\uparrow\downarrow}(\Omega, \theta, \theta')$ calculated for an A_{1g} phonon mode shown in the inset of the figure for fixed values of Ω and θ', in octahedral type cuprates. In this case θ' is taken a value near G_1 point.
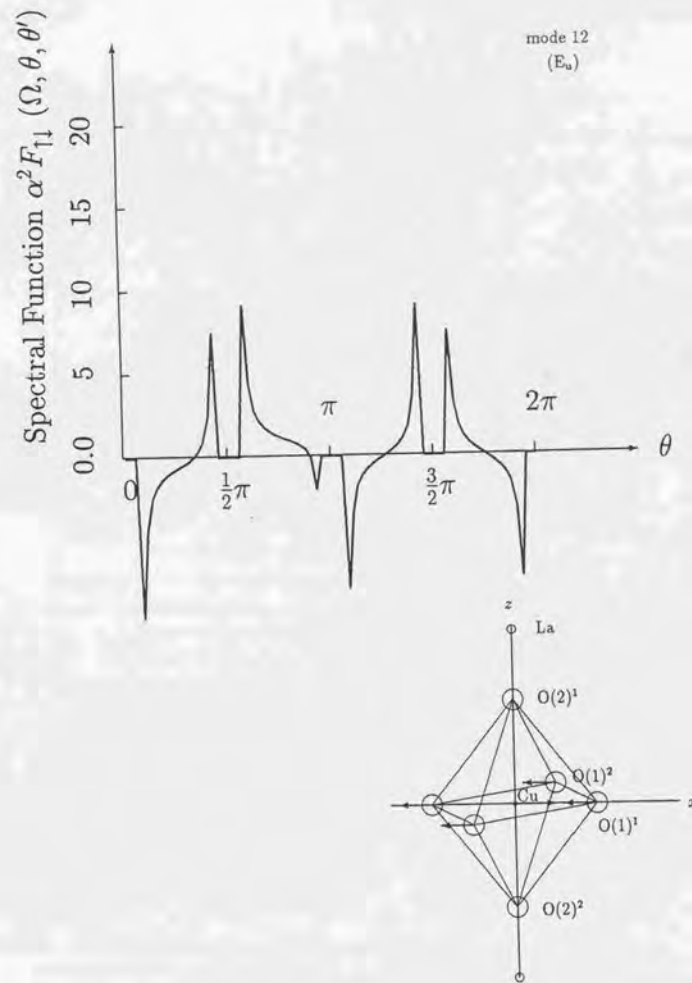
Figure 34: The θ dependence of the momentum dependent spectral function $\alpha^2 F_{\uparrow\downarrow}(\Omega, \theta, \theta')$ calculated for an E_u phonon mode shown in the inset of the figure for fixed values of Ω and θ', in octahedral type cuprates. In this case θ' is taken a value near G_1 point.
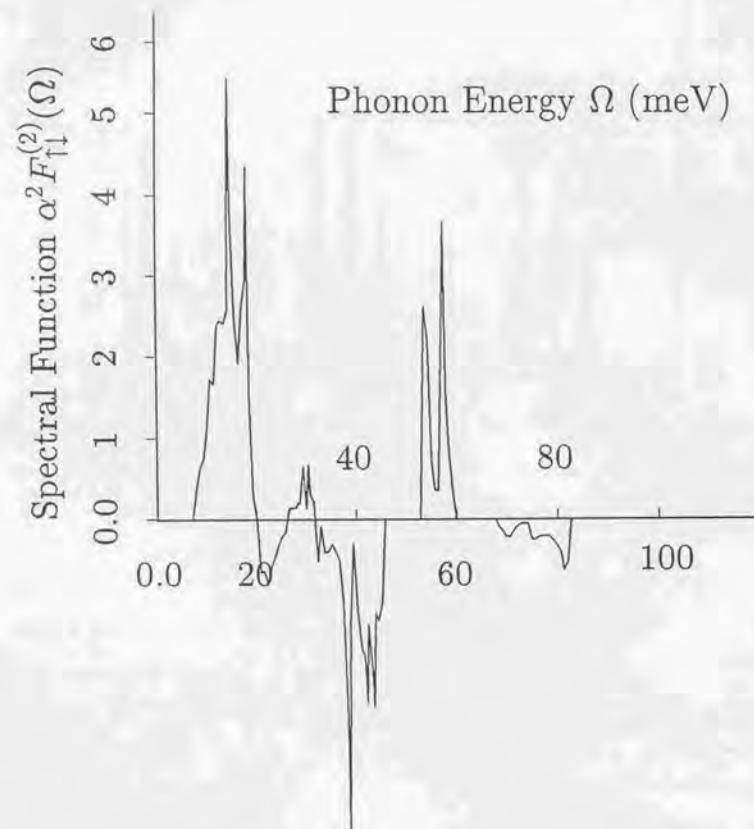
Figure 35: The d-wave component of the spectral function, $\alpha^2 F_{\uparrow\downarrow}^{(2)}(\Omega)$, calculated for LSCO with $x = 0.15$, due to the contribution from all the phonon modes in LSCO.

	La¹	La²	Cu	O(1)¹	O(1)²	O(2)¹	O(2)²	mode
La	(100)	(100)	(100)	(100)	(100)	(100)	(100)	E_u
	(010)	(010)	(010)	(010)	(010)	(010)	(010)	E_u
	(001)	(001)	(001)	(001)	(001)	(001)	(001)	A_{2u}
	(100)	($\bar{1}$00)				(100)	($\bar{1}$00)	E_g
	(010)	(0$\bar{1}$0)				(010)	(0$\bar{1}$0)	E_g
	(001)	(00$\bar{1}$)				(001)	(00$\bar{1}$)	A_{1g}
Cu	($\frac{3}{4}$00)	($\frac{3}{4}$00)	(100)	(100)	(100)	($\frac{3}{4}$00)	($\frac{3}{4}$00)	E_u
	(0$\frac{3}{4}$0)	(0$\frac{3}{4}$0)	(010)	(010)	(010)	(0$\frac{3}{4}$0)	(0$\frac{3}{4}$0)	E_u
	(00$\frac{3}{4}$)	(00$\frac{3}{4}$)	(001)	(001)	(001)	(00$\frac{3}{4}$)	(00$\frac{3}{4}$)	A_{2u}
O(1) s				(100)	($\bar{1}$00)			E_u
				(010)	(0$\bar{1}$0)			E_u
O(1) b			(200)	($\bar{1}$00)	($\bar{1}$00)			E_u
			(020)	(0$\bar{1}$0)	(0$\bar{1}$0)			E_u
			(002)	(001)	(001)			A_{2u}
				(001)	(00$\bar{1}$)			B_{2u}
O(2) s	(001)	(001)				(00$\bar{1}$)	(00$\bar{1}$)	A_{2u}
	(001)	(001)				(00$\bar{1}$)	(001)	A_{1g}
O(2) b	(100)	(100)				($\bar{1}$00)	($\bar{1}$00)	E_u
	(010)	(010)				(0$\bar{1}$0)	(0$\bar{1}$0)	E_u
	(100)	(100)				(100)	(100)	E_g
	(010)	(010)				(010)	(010)	E_g

Table 6: Normal modes corresponding to Δ-line, $(0,0)\rightarrow(\pi,0)$, for LSCO. The mass ratio to satisfy the orthogonality relation are omitted in the table. See S. Mase *etal.*, Phonon Dispersion Curves of High T_c Superconductors I. $(La_{1-x}Sr_x)_2\,Cu\,O_4$, J. Phys. Soc. Jpn. **57** (1988) 607.

contribution to the spectral function which causes a mass enhancement of the electronic states, $\alpha^2 F_{\uparrow\uparrow}^{(0)}(\Omega)$, in Fig. 36.

In the present electron and spin structure characterized by the alternant appearance of the a_{1g}^* and the b_{1g} orbitals and the different spatial distribution of Bloch wave functions for up-spin and down-spin dopant holes, $V_{\uparrow}^{\gamma}(\boldsymbol{k}, \boldsymbol{k}')$ is different from $V_{\downarrow}^{\gamma}(\boldsymbol{k}, \boldsymbol{k}')$ and thus $\alpha^2 F_{\uparrow\downarrow}(\Omega, \theta, \theta')$ changes its sign as is shown in Appendix E. This situation makes the $\boldsymbol{k}$ dependence of $\alpha^2 F_{\uparrow\downarrow}(\Omega, \theta, \theta')$ much sharper and stronger than in the case of an ordinary unit cell, and this characteristic $\boldsymbol{k}$ dependence produces the large d-wave component of the spectral function. In the ordinary case, a d-wave component is always small because of the positive definite $\boldsymbol{k}$ dependence of $\alpha^2 F_{\uparrow\downarrow}(\Omega, \theta, \theta')$. Thus the present electron and spin structure is a key factor in creating d-wave pairing in the phonon mechanism [40].
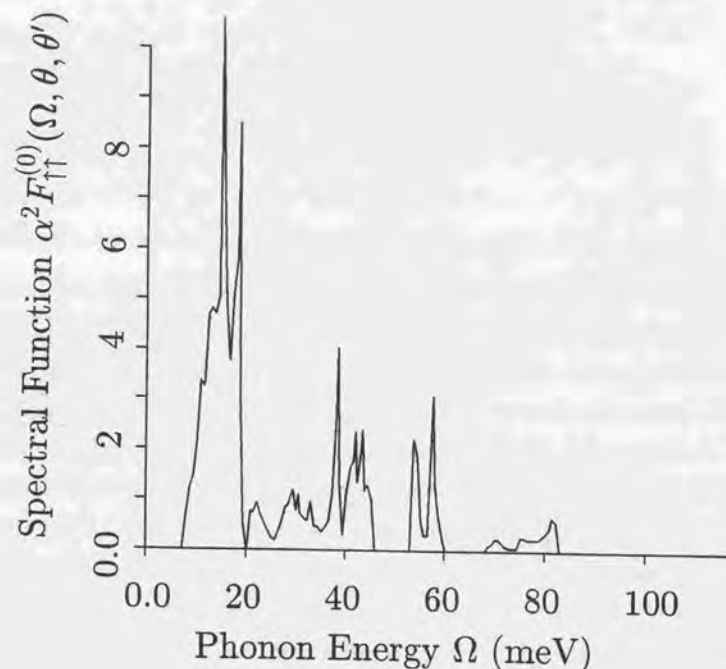

Figure 36: The spectral function, which contributes to mass enhancement, $\alpha^2 F_{\uparrow\uparrow}^{(0)}(\Omega)$, calculated for LSCO with $x = 0.15$, due to the contribution from all the phonon modes in LSCO.

6-5. The d-wave Superconductivity and the Transition Temperature of LSCO

Recently Ushio and Kamimura[18] have extended a McMillan's simplified version of the Eliashberg gap equation to the case of a complicated band structure, in which the density of states near the Fermi level is exceedingly large. Now we follow their treatment to calculate T_c as a function of hole concentration x. In the usual McMillan equation which determines T_c, the integral over the energy is taken from 0 to ω_D, but in the present case, in which the holes have coherence only within the spin correlated region, the lower limit of the integral becomes ω_s as was discussed by Matsuno et.al.[36]. Here the cut-off parameter ω_s is defined by the relation $\omega_s = v_F/\lambda_s$ with v_F being the Fermi velocity and λ_s the characteristic length for the coherent motion of a hole which should be proportional to the AF correlation length determined by the neutron inelastic scattering experiments, λ_{AF}. The new cut-off parameter ω_s appeared in the present theory is clearly unfavorable to the occurrence of superconductivity, because it excludes the contribution from a certain energy region across the Fermi surface. In other words, because of the relation $\omega_s = v_F/\lambda_s$, when λ_s becomes shorter, physical quantities which contributes superconductivity become smaller, and thus T_c becomes lower. We take into account the effects of λ_s by substituting $d\omega' \cdot \omega'^2/(\omega'^2 + \omega_s^2)$ for $d\omega'$ in the integration over energy.

The linearized Eliashberg equation for d-wave superconductivity is derived in Appendix F. By using the Eq.(8.32) and Eq.(8.33) in Appendix F, we obtain the set of equations which determine the transition temperature of d-wave superconductivity, T_c,

as follows[36,18,124],

$$1 = \lambda' \int_0^{\omega_D} d\omega' \frac{\omega'^2}{\omega'^2 + \omega_s^2} \frac{[\rho(\omega' Z(0)) + \rho(-\omega' Z(0))]}{2\rho_F} \frac{1}{\omega'} \tanh\left(\frac{\omega'}{2k_B T_c}\right), \quad (6.25)$$

$$Z(0) = 1 + \lambda_0 \int_0^{\infty} d\omega' \frac{\omega'^2}{\omega'^2 + \omega_s^2} \frac{[\rho(\omega' Z(0)) + \rho(-\omega' Z(0))]}{2\rho_F} \frac{\omega_D}{(\omega' + \omega_D)^2}, \quad (6.26)$$

where

$$\lambda' = \frac{\lambda_d - \mu^*}{Z(0)}, \quad (6.27)$$

with $\rho(\omega)$ being the energy-dependent density of states, ρ_F the density of states at Fermi level, and μ^* being the effective Coulomb repulsion term. As seen from Eq. (6.25) and Eq. (6.26) (from Eq. (6.26), it is apparent that $Z(0) > 1$), the normalization factor $Z(0)$ has a reduction effect of T_c, i.e. a 'bare' Cooper pair coupling constant λ_d is reduced to λ' in the T_c equation Eq. (6.25). In addition, we note that unlike ordinary Eliashberg equation, the ω-dependence of the density of states ρ appears in Eq. (6.25) as $\rho = \rho(\omega Z(0))$. This term is important for the present case because it is favorable for the occurrence of superconductivity, since the large peak value of the DOS can contribute to the integral of Eq. (6.25) even if the Fermi level is somewhat distanced from the peak of the DOS.

In the present section, we have applied the above set of equations (6.25)-(6.27) to the conduction band of LSCO calculated in Chapter 4. Although the value of λ_d depends on x, it is nearly proportional to $\rho_F(x)$. So that, in the present calculation, we have used the approximation that $\lambda_d(x) = \lambda_{do}\rho_F(x)/\rho_{Fo}$ where λ_{do} and ρ_{Fo} are the values of $\lambda_d(x)$ and $\rho_F(x)$ corresponding to optimal doping, i.e. $x = 0.15$. In doing so, we have used a calculated value for λ_{do}, i.e. $\lambda_{do} = 1.96$, following Section 6-4. For a value of the effective Coulomb repulsion constant μ^*, we have adopted a value of $\mu^* = 0$, because the holes with up-spin and down-spin occupy different orbitals at the same CuO_6 cluster so that the Coulomb repulsion energy between those holes with different spins is expected to be small in itself and its d-wave component becomes smaller. We have used the value $\omega_D = 50\text{meV}$ considering that the various optical modes contribute to the d-wave pairing.

The cut-off parameter ω_s in Eq. (6.25) depends on the hole concentration x

through λ_s and v_F as seen from the relation $\omega_s = v_F/\lambda_s$. For a value of v_F we have used the calculated value of the Fermi velocity averaged over the Fermi surface, i.e. $v_F(x) \sim 1.1 \times 10^{-7}$cm/s for $x = 0.15$. As regards the x-dependent spin correlation length λ_{AF}, Mason et al.[78] and Yamada et al.[125] have recently reported independently by the neutron inelastic scattering experiments in LSCO that, below T_c the spin correlation length increases with increase of hole concentration up to the optimal doping. In particular, Mason et al. have reported an extraordinarily long correlation length, in excess of 50 Å. In the overdoped regime, our theory predicts the decrease of the spin correlation length. Assuming the $\lambda_s(x)$ to be similar in shape to the spin correlation length $\lambda_{AF}(x)$ but different in the magnitude, we have calculated T_c as a function of hole concentration x. The magnitude of λ_s was determined so as to reproduce the experimental T_c-x relation. The calculated T_c is shown as a function of x in Fig. 37(a), with the experimental data by Takagi et al.[44]. The calculated T_c in the whole concentration region agrees very well with that of experimental result by Takagi et al.

According to Matsuno et al.[124], T_c suddenly decreases and T_c becomes zero as a ratio ω_D/ω_s reaches the value r_0 which is given as $r_0 = \exp[1/\lambda_d]$ Thus in the Sr concentration region $x \leq 0.05$ where λ_d is small, the calculated transition temperature T_c vanishes by the reduction effect of λ_s. In the region $0.05 \leq x \leq 0.15$, the transition temperature T_c increases with increasing x, because both DOS and λ_s increase. The transition temperature T_c takes a maximum value at $x = 0.15$. Then T_c decreases from its maximum with further increasing x. The decrease of T_c in the region $x \geq 0.15$ mainly comes from the fact that the coherence length λ_s decreases in this region. According to the present calculation, T_c in the well-over-doped region ($x \geq 0.25$) is zero.

The assumed coherence length λ_s represented by thin line in Fig. 37(a) is considerably larger than the reported AF correlation length λ_{AF}. In the present calculation, however, the electron-phonon interaction due to the change of the distance between O-O, La-Cu, La-O etc. are not taken into account, and so the value $\lambda_{do} = 1.96$ may be underestimated. Thus it is not surprising that we had to take much larger value for λ_s compared to λ_{AF}. We have also calculated the transition temperature T_c with
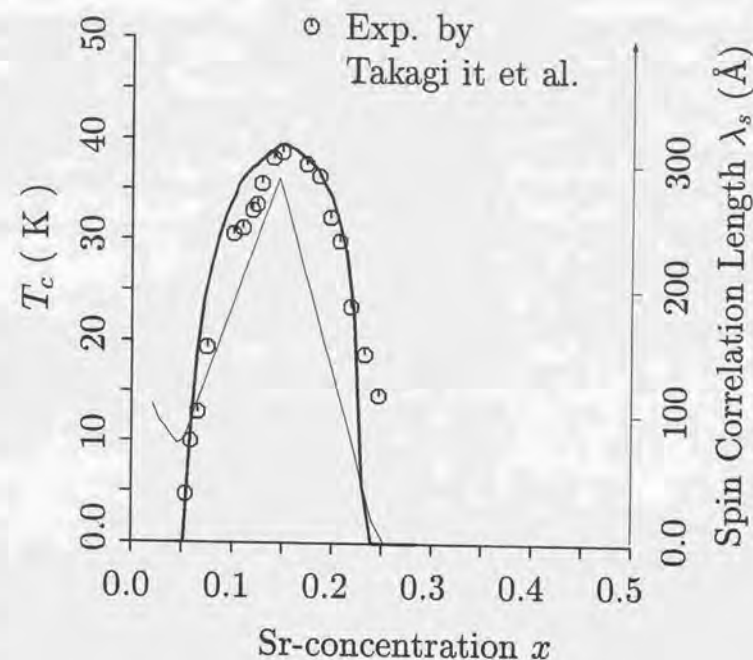
Figure 37: (a) The calculated T_c curve (thick line) of LSCO. The thin line shows the x-dependence of λ_s the magnitude of which is determined so as to reproduce T_c in the theoretical calculation.

the effective electron-phonon coupling constant $\lambda_{do} = 2.4$ which is 20% larger than the calculated value. The result is shown in the Fig. 37(b) with the coherence length $\lambda_s(x)$ which is used in this calculation. In this case, λ_s is comparable to the AF correlation length observed by neutron inelastic scattering experiments, λ_{AF}. | Fig. 37 |

In the ordinary BCS theory the zero-temperature energy gap parameter $\Delta(0)$ and the transition temperature T_c are related by a relation of $\frac{2\Delta(0)}{T_c} = 3.5$, while the experimentally reported ratio for cuprates vary from 5 to 9. Thus it is interesting to calculate the energy gap parameter $\Delta(0)$ based on the present electronic structure. The energy gap parameter $\Delta(T)$ is calculated from the following gap equation,

$$1 = \lambda' \int_0^{\omega_D} d\omega' \frac{\omega'^2}{\omega'^2 + \omega_s^2} \frac{[\rho(\omega' Z(0)) + \rho(-\omega' Z(0))]}{2\rho_F} \frac{1}{E} \tanh\left(\frac{E}{2k_B T}\right), \quad (6.28)$$

$$(6.29)$$

where

$$E = [\omega'^2 + \Delta(T)^2]^{1/2} . \quad (6.30)$$

The calculated results for the zero temperature energy gap parameter $\Delta(T = 0) \equiv \Delta(0)$ gives the ratio of $\frac{2\Delta(0)}{T_c} = 4.1$ for $x = 0.15$.*

---

* Note added in proof: In this section $\Delta(0)$ is the energy gap parameter averaged with respect to θ. And we obtain the relation $\frac{2\Delta_{max}(0)}{T_c} \sim \frac{\pi}{2}\Delta(0) \sim 6$.
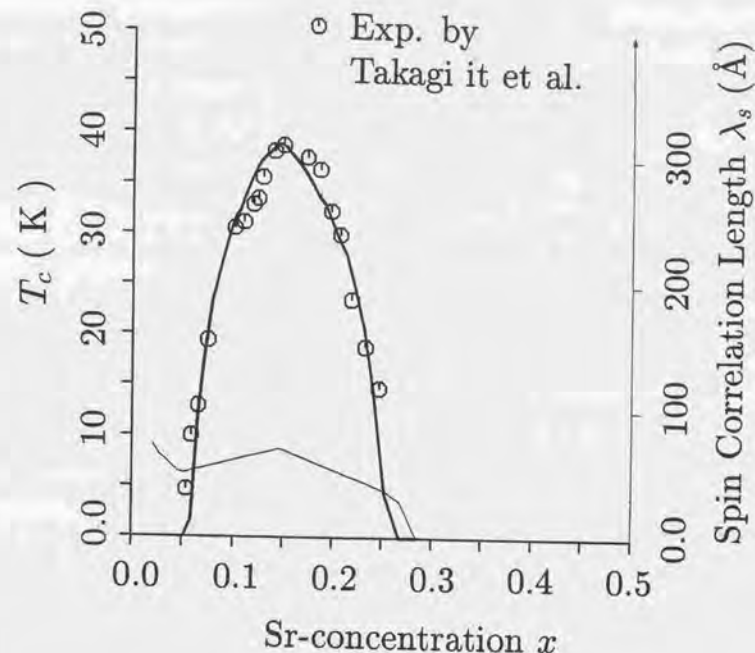

Figure 37: (b) The calculated T_c curve (thick line) by adopting the normalized non-dimensional coupling constant multiplied by a factor 1.2. The thin line shows the x-dependence of λ_s the magnitude of which is determined so as to reproduce T_c in the theoretical calculation.

6-6. Conclusions

In this chapter we have calculated the electron-phonon interaction in $La_{2-x}Sr_xCuO_4$ and then the spectral function, by using the renormalized electronic energy band and their structure obtained in Chapter 4. First we have showed that the electron-phonon interactions which scatter pairs of electrons from one pair state $(k \uparrow, -k \downarrow)$ to a different pair state $(k' \uparrow, -k' \downarrow)$ are repulsive for some combinations of (k, k') and attractive for other combinations. Then we have calculated numerically $\alpha^2 F_{\uparrow\uparrow}(\Omega, \theta, \theta')$ and $\alpha^2 F_{\uparrow\downarrow}(\Omega, \theta, \theta')$ which contribute to mass renormalization and gap formation, respectively. The calculated momentum-dependent spectral function for the singlet Cooper pairs, $\alpha^2 F_{\uparrow\downarrow}(\Omega, \theta, \theta')$, exhibits a sharp k-dependence and a d-wave symmetry. The calculated d-wave component of the spectral function, $\alpha^2 F_{\uparrow\downarrow}^{(2)}(\Omega)$, is large and the calculated s-wave component of the spectral function, $\alpha^2 F_{\uparrow\downarrow}^{(0)}(\Omega)$ is almost zero. This leads to the occurrence of d-wave superconductivity in LSCO. In general the ordinary phonon-mediated interaction always favors s-wave symmetry, then the fact that d-wave symmetry is favored in the present calculation is unique to our model where such pairing interaction originates from the different spatial distribution of Bloch wave functions for up-spin and down-spin dopant holes. From the calculated d-wave component of the spectral function, the electron-phonon coupling constant for d-wave pairing is estimated as 1.96 for optimal doped LSCO, suggesting that LSCO is a strong coupling superconductor.

The transition temperature for superconductivity with d-wave symmetry is also calculated. The large electron-phonon coupling constant and the property of d-wave coupling that the Coulomb repulsion effect is almost negligible enable us to obtain very high superconducting transition temperature. However, in the present model, the existence of the condition that a Cooper pair must be formed within the range of spin correlated region reduces T_c. Thus T_c is determined mainly by three key factors; the electron-phonon coupling constant λ_d, the density of states at Fermi energy $\rho(E_F)$ and the coherence length λ_s which is the scale for antiferromagnetic domain.

Chapter 7.

Summary

We have constructed the effective one-electron-type band structure by renormalizing the effects of the exchange interaction between the spin of a carrier hole and a localized spin and the Hubbard U interaction for localized holes into the electronic state of the carriers. Important calculated results are listed below. (1) In undoped La_2CuO_4, all the calculated bands are occupied by electrons and thus La_2CuO_4 becomes an insulator. (2) The top of the highest band is at Δ-point and the calculated Fermi surface is small with finite lifetime, and this is consistent with AF super-structure for $Bi_2Sr_2CaCu_2O_{8+\delta}$ (Bi 2212) determined by angle-resolved photoemission[104,105,102,108,109], (3)The wave function of the conduction band consists of the b_{1g} orbital at the low hole concentration region. While, in the superconducting region, holes itinerate from the a_{1g}^* orbital at A-site and the b_{1g} orbital at B-site, consistent with the polarization-dependent X-ray absorption measurements for O K-edge and Cu L-edge in LSCO by Chen et al..

We have also explained various anomalous features of normal state properties of LSCO by using the effective one-electron-type energy band. The density of states calculated from conduction band in Chapter 4 is consistent with the observed x-dependence of the electronic specific heat. The prediction of the small Fermi surface is also consistent with the linear temperature dependence of the resistivity down to T_c, the x-dependence of Hall coefficient which decreases more rapidly than the $1/x$ behavior and changes its sign around $x = 0.3$, and the large T dependence of R_H. The shape of the Fermi surface is discussed with respect to the possible occurrence of the incommensurate peak of the neutron scattering and the instability at $x = 0.125$.

Assuming a realistic electron-phonon coupling term, we have calculated the spectral functions and showed the occurrence of d-wave superconductivity due to the present electronic structure that the wave function for up-spin dopant holes differs from that for down-spin and the a_{1g}^* and the b_{1g} orbitals appear alternately. We have also calculated the transition temperature of d-wave superconductivity. The key factors of the high transition temperature are the large electron-phonon coupling constant, large density of states near the Fermi energy, the large coherence length λ_s of the optimal doped LSCO, and the negligibly small Coulomb repulsion effect due to both the property of d-wave pairing and the different spatial distribution of Bloch wave functions for up-spin and down-spin dopant holes at the same CuO_6 cluster.

Finally we would like to make a remark for the experiment which would confirm the validity of the present theory, especially the characteristic features of the wave functions mentioned before. We would expect that the atomic site STM experiments with extremely strong magnetic field might detect the difference of the wave functions of up-spin and down-spin dopant holes. If the strong magnetic field is applied parallel to z-axis, the number of the up-spin dopant holes increases and that of down-spin decreases. The difference between the number of up-spin dopant holes and that of down-spin is nearly 1% with the applied magnetic field $H \sim 10T$. Then the the number of the a_{1g}^* holes is increases at A-site and decreases at B-site, while that of the b_{1g} holes increases at B-site and decreases at A-site. Assuming that the tunneling probability of a_{1g}^* orbitals is different from that of b_{1g} orbitals, the difference between A-site and B-site is expected to be observed by the atomic site STM experiments.

Appendix A. The Matrix Elements of 17×17 Hamiltonian Matrix

The matrix elements of the Hamiltonian matrix shown in Table 2, are expressed with 17 SK parameters as

$$E_1 = E_p^1$$

$$E_2 = E_p^2$$

$$E_3 = E_{dxy} + 2\ t(dd\pi)(\cos k_x a + \cos k_y a)$$

$$E_4 = E_{dxy} + 2\ t(dd\pi)\cos k_y a + 2\ t(dd\delta)\cos k_x a$$

$$E_5 = E_{dxy} + 2\ t(dd\pi)\cos k_x a + 2\ t(dd\delta)\cos k_y a$$

$$E_6 = E_{dx^2-y^2} + [\ \frac{3}{2}\ t(dd\sigma) + \frac{1}{2}\ t(dd\delta)\ ]\ (\cos k_x a + \cos k_y a)$$

$$E_7 = E_{dx^2-y^2} + [\ \frac{1}{2}\ t(dd\sigma) + \frac{3}{2}\ t(dd\delta)\ ]\ (\cos k_x a + \cos k_y a)$$

$$T_1 = 2\ [\ t_1(pp\sigma) + t_1(pp\pi)\ ]\ \cos \frac{k_x a}{2}\cos \frac{k_y a}{2}$$

$$T_2 = -2\ [\ t_1(pp\sigma) - t_1(pp\pi)\ ]\ \sin \frac{k_x a}{2}\sin \frac{k_y a}{2}$$

$$T_3 = 4\ t_1(pp\pi)\cos \frac{k_x a}{2}\cos \frac{k_y a}{2}$$

$$T_4 = 2\ [\ l_1^2\ t_2(pp\sigma) + (1 - l_1^2)\ t_2(pp\pi)\ ]\ \cos \frac{k_x a}{2}e^{i\ 0.364 k_z c/2}$$

$$T_5 = i\ 2l_1 n_1\ [\ t_2(pp\sigma) - t_2(pp\pi)\ ]\ \sin \frac{k_x a}{2}e^{i\ 0.364 k_z c/2}$$

$$T_6 = 2\ t_2(pp\pi)\cos \frac{k_x a}{2}e^{i\ 0.364 k_z c/2}$$

$$T_7 = 2\ [\ n_1^2\ t_2(pp\sigma) + (1 - n_1^2)\ t_2(pp\pi)\ ]\ \cos \frac{k_x a}{2}e^{i\ 0.364 k_z c/2}$$

$$T_4' = 2\ [\ l_1^2\ t_2(pp\sigma) + (1 - l_1^2)\ t_2(pp\pi)\ ]\ \cos \frac{k_y a}{2}e^{i\ 0.364 k_z c/2}$$

$$T_5' = i\ 2l_1 n_1\ [\ t_2(pp\sigma) - t_2(pp\pi)\ ]\ \sin \frac{k_y a}{2}e^{i\ 0.364 k_z c/2}$$

$$T_6' = 2\ t_2(pp\pi)\cos \frac{k_y a}{2}e^{i\ 0.364 k_z c/2}$$

$$T_7' = 2\ [\ n_1^2\ t_2(pp\sigma) + (1 - n_1^2)\ t_2(pp\pi)\ ]\ \cos \frac{k_y a}{2}e^{i\ 0.364 k_z c/2}$$

$$T_8 = 4\ [\ l_2^2\ t_3(pp\sigma) + (1 - l_2^2)\ t_3(pp\pi)\ ]\ \cos \frac{k_x a}{2}\cos \frac{k_y a}{2}e^{i\ 0.272 k_z c/2}$$

$$T_9 = 4\ [\ n_2^2\ t_3(pp\sigma) + (1 - n_2^2)\ t_3(pp\pi)\ ]\ \cos \frac{k_x a}{2}\cos \frac{k_y a}{2}e^{i\ 0.272 k_z c/2}$$

$$T_{10} = -4l_2^2\ [\ t_3(pp\sigma) - t_3(pp\pi)\ ]\ \sin \frac{k_x a}{2}\sin \frac{k_y a}{2}e^{i\ 0.272 k_z c/2}$$

$$T_{11} = i\ 4l_2 n_2\ [\ t_3(pp\sigma) - t_3(pp\pi)\ ]\ \sin \frac{k_x a}{2}\cos \frac{k_y a}{2}e^{i\ 0.272 k_z c/2}$$

$$T_{12} = i\ 4l_2 n_2\ [\ t_3(pp\sigma) - t_3(pp\pi)\ ]\ \cos \frac{k_x a}{2}\sin \frac{k_y a}{2}e^{i\ 0.272 k_z c/2}$$

$$T_{13} = i\ \sqrt{3}\ t_1(pd\sigma)\sin \frac{k_x a}{2}$$

$$T_{14} = -i\ t_1(pd\sigma)\sin \frac{k_x a}{2}$$

$$T_{15} = i\ 2\ t_1(pd\pi)\sin \frac{k_x a}{2}$$

$$T_{13}' = -i\ \sqrt{3}\ t_1(pd\sigma)\sin \frac{k_y a}{2}$$

$$T_{14}' = -i\ t_1(pd\sigma)\sin \frac{k_y a}{2}$$

$$T_{15}' = i\ 2\ t_1(pd\pi)\sin \frac{k_y a}{2}$$

$$T_{16} = t_2(pd\pi)e^{i\ 0.364 k_z c/2}$$

$$T_{17} = t_2(pd\sigma)e^{i\ 0.364 k_z c/2}$$

$$T_{18} = \frac{\sqrt{3}}{2}\ [\ -t(dd\sigma) + t(dd\delta)\ ]\ (\cos k_x a - \cos k_y a) \tag{8.1}$$

where

$$l_1 = \frac{0.5a}{\sqrt{(0.5a)^2 + (0.364c/2)^2}}$$

$$n_1 = \frac{0.364c/2}{\sqrt{(0.5a)^2 + (0.364c/2)^2}}$$

$$l_2 = \frac{0.5a}{\sqrt{2(0.5a)^2 + (0.272c/2)^2}}$$

$$n_2 = \frac{0.272c/2}{\sqrt{2(0.5a)^2 + (0.272c/2)^2}} \tag{8.2}$$

Appendix B. The Matrix Elements of 34×34 Hamiltonian Matrix

The matrix elements in Table 3 are expressed with SK parameters as follows. For on-site elements of $\tilde{H}_{AA}^0(\boldsymbol{k})$ and $\tilde{H}_{BB}^0(\boldsymbol{k})$,

$$E_1 = E_p^1$$
$$E_2 = E_p^2$$
$$E_3 = E_{dxy}$$
$$E_4 = E_{dxy}$$
$$E_5 = E_{dxy}$$
$$E_6 = E_{dx^2-y^2}$$
$$E_7 = E_{dx^2-y^2},$$

$$(8.3)$$

for the diagonal elements of $\tilde{H}_{AB}^0(\boldsymbol{k})$ and $\tilde{H}_{BA}^0(\boldsymbol{k})$,

$$E_1 = 0$$
$$E_2 = 0$$
$$E_3 = +2\,t(dd\pi)(\cos k_x a + \cos k_y a)$$
$$E_4 = +2\,t(dd\pi)\cos k_y a + 2\,t(dd\delta)\cos k_x a$$
$$E_5 = +2\,t(dd\pi)\cos k_x a + 2\,t(dd\delta)\cos k_y a$$
$$E_6 = + \left[\,\frac{3}{2}\,t(dd\sigma) + \frac{1}{2}\,t(dd\delta)\,\right](\cos k_x a + \cos k_y a)$$
$$E_7 = + \left[\,\frac{1}{2}\,t(dd\sigma) + \frac{3}{2}\,t(dd\delta)\,\right](\cos k_x a + \cos k_y a),$$

$$(8.4)$$

for the off-diagonal elements of $\tilde{H}_{AA}^0(\boldsymbol{k})$ and $\tilde{H}_{BB}^0(\boldsymbol{k})$

$$T_1 = \frac{1}{2}\,[\,t_1(pp\sigma) + t_1(pp\pi)\,]\,(e^{i\frac{k_x a}{2}}e^{-i\frac{k_y a}{2}} + e^{-i\frac{k_x a}{2}}e^{i\frac{k_y a}{2}})$$
$$T_2 = -\frac{1}{2}[\,t_1(pp\sigma) - t_1(pp\pi)\,]\,(e^{i\frac{k_x a}{2}}e^{-i\frac{k_y a}{2}} + e^{-i\frac{k_x a}{2}}e^{i\frac{k_y a}{2}})$$
$$T_3 = t_1(pp\pi)(e^{i\frac{k_x a}{2}}e^{-i\frac{k_y a}{2}} + e^{-i\frac{k_x a}{2}}e^{i\frac{k_y a}{2}})$$
$$T_4 = [\,l_1^2\,t_2(pp\sigma) + (1-l_1^2)\,t_2(pp\pi)\,]\,e^{-i\frac{k_x a}{2}}e^{i\,0.364k_z c/2}$$
$$T_5 = -l_1 n_1\,[\,t_2(pp\sigma) - t_2(pp\pi)\,]\,e^{-i\frac{k_x a}{2}}e^{i\,0.364k_z c/2}$$
$$T_6 = t_2(pp\pi)e^{-i\frac{k_x a}{2}}e^{i\,0.364k_z c/2}$$
$$T_7 = [\,n_1^2\,t_2(pp\sigma) + (1-n_1^2)\,t_2(pp\pi)\,]\,e^{-i\frac{k_x a}{2}}e^{i\,0.364k_z c/2}$$
$$T_4' = [\,l_1^2\,t_2(pp\sigma) + (1-l_1^2)\,t_2(pp\pi)\,]\,e^{-i\frac{k_y a}{2}}e^{i\,0.364k_z c/2}$$
$$T_5' = -l_1 n_1\,[\,t_2(pp\sigma) - t_2(pp\pi)\,]\,e^{-i\frac{k_y a}{2}}e^{i\,0.364k_z c/2}$$
$$T_6' = t_2(pp\pi)e^{-i\frac{k_y a}{2}}e^{i\,0.364k_z c/2}$$
$$T_7' = [\,n_1^2\,t_2(pp\sigma) + (1-n_1^2)\,t_2(pp\pi)\,]\,e^{-i\frac{k_y a}{2}}e^{i\,0.364k_z c/2}$$
$$T_8 = [\,l_2^2\,t_3(pp\sigma) + (1-l_2^2)\,t_3(pp\pi)\,]\,(e^{i\frac{k_x a}{2}}e^{-i\frac{k_y a}{2}} + e^{-i\frac{k_x a}{2}}e^{i\frac{k_y a}{2}})e^{i\,0.272k_z c/2}$$
$$T_9 = [\,n_2^2\,t_3(pp\sigma) + (1-n_2^2)\,t_3(pp\pi)\,]\,(e^{i\frac{k_x a}{2}}e^{-i\frac{k_y a}{2}} + e^{-i\frac{k_x a}{2}}e^{i\frac{k_y a}{2}})e^{i\,0.272k_z c/2}$$
$$T_{10} = -l_2^2\,[\,t_3(pp\sigma) - t_3(pp\pi)\,]\,(e^{i\frac{k_x a}{2}}e^{-i\frac{k_y a}{2}} + e^{-i\frac{k_x a}{2}}e^{i\frac{k_y a}{2}})e^{i\,0.272k_z c/2}$$
$$T_{11} = l_2 n_2\,[\,t_3(pp\sigma) - t_3(pp\pi)\,]\,(e^{i\frac{k_x a}{2}}e^{-i\frac{k_y a}{2}} - e^{-i\frac{k_x a}{2}}e^{i\frac{k_y a}{2}})e^{i\,0.272k_z c/2}$$
$$T_{12} = l_2 n_2\,[\,t_3(pp\sigma) - t_3(pp\pi)\,]\,(-e^{i\frac{k_x a}{2}}e^{-i\frac{k_y a}{2}} + e^{-i\frac{k_x a}{2}}e^{i\frac{k_y a}{2}})e^{i\,0.272k_z c/2}$$
$$T_{13} = -\frac{\sqrt{3}}{2}\,t_1(pd\sigma)e^{-i\frac{k_x a}{2}}$$
$$T_{14} = \frac{1}{2}t_1(pd\sigma)e^{-i\frac{k_x a}{2}}$$
$$T_{15} = -t_1(pd\pi)e^{-i\frac{k_x a}{2}}$$
$$T_{13}' = \frac{\sqrt{3}}{2}\,t_1(pd\sigma)e^{-i\frac{k_y a}{2}}$$
$$T_{14}' = \frac{1}{2}t_1(pd\sigma)e^{-i\frac{k_y a}{2}}$$
$$T_{15}' = -t_1(pd\pi)e^{-i\frac{k_y a}{2}}$$
$$T_{16} = t_2(pd\pi)e^{i\,0.364k_z c/2}$$
$$T_{17} = t_2(pd\sigma)e^{i\,0.364k_z c/2}$$
$$T_{18} = 0,$$

$$(8.5)$$

and for the off-diagonal elements of $\tilde{H}^0_{AB}(\boldsymbol{k})$ and $\tilde{H}^0_{BA}(\boldsymbol{k})$

$$T_1 = \frac{1}{2}\left[\, t_1(pp\sigma) + t_1(pp\pi) \,\right] (e^{i\frac{k_x a}{2}} e^{i\frac{k_y a}{2}} + e^{-i\frac{k_x a}{2}} e^{-i\frac{k_y a}{2}})$$

$$T_2 = \frac{1}{2}\left[\, t_1(pp\sigma) - t_1(pp\pi) \,\right] (e^{i\frac{k_x a}{2}} e^{i\frac{k_y a}{2}} + e^{-i\frac{k_x a}{2}} e^{-i\frac{k_y a}{2}})$$

$$T_3 = t_1(pp\pi)\cos\frac{k_x a}{2}(e^{i\frac{k_x a}{2}} e^{i\frac{k_y a}{2}} + e^{-i\frac{k_x a}{2}} e^{-i\frac{k_y a}{2}})$$

$$T_4 = \left[\, l_1^2\, t_2(pp\sigma) + (1 - l_1^2)\, t_2(pp\pi) \,\right] e^{i\frac{k_x a}{2}} e^{i\,0.364 k_z c/2}$$

$$T_5 = l_1 n_1 \left[\, t_2(pp\sigma) - t_2(pp\pi) \,\right] e^{i\frac{k_x a}{2}} e^{i\,0.364 k_z c/2}$$

$$T_6 = t_2(pp\pi) e^{i\frac{k_x a}{2}} e^{i\,0.364 k_z c/2}$$

$$T_7 = \left[\, n_1^2\, t_2(pp\sigma) + (1 - n_1^2)\, t_2(pp\pi) \,\right] e^{i\frac{k_x a}{2}} e^{i\,0.364 k_z c/2}$$

$$T_4' = \left[\, l_1^2\, t_2(pp\sigma) + (1 - l_1^2)\, t_2(pp\pi) \,\right] e^{i\frac{k_y a}{2}} e^{i\,0.364 k_z c/2}$$

$$T_5' = l_1 n_1 \left[\, t_2(pp\sigma) - t_2(pp\pi) \,\right] e^{i\frac{k_y a}{2}} e^{i\,0.364 k_z c/2}$$

$$T_6' = t_2(pp\pi) e^{i\frac{k_y a}{2}} e^{i\,0.364 k_z c/2}$$

$$T_7' = \left[\, n_1^2\, t_2(pp\sigma) + (1 - n_1^2)\, t_2(pp\pi) \,\right] e^{i\frac{k_y a}{2}} e^{i\,0.364 k_z c/2}$$

$$T_8 = \left[\, l_2^2\, t_3(pp\sigma) + (1 - l_2^2)\, t_3(pp\pi) \,\right] (e^{i\frac{k_x a}{2}} e^{i\frac{k_y a}{2}} + e^{-i\frac{k_x a}{2}} e^{-i\frac{k_y a}{2}}) e^{i\,0.364 k_z c/2}$$

$$T_9 = \left[\, n_2^2\, t_3(pp\sigma) + (1 - n_2^2)\, t_3(pp\pi) \,\right] (e^{i\frac{k_x a}{2}} e^{i\frac{k_y a}{2}} + e^{-i\frac{k_x a}{2}} e^{-i\frac{k_y a}{2}}) e^{i\,0.272 k_z c/2}$$

$$T_{10} = l_2^2 \left[\, t_3(pp\sigma) - t_3(pp\pi) \,\right] (e^{i\frac{k_x a}{2}} e^{i\frac{k_y a}{2}} + e^{-i\frac{k_x a}{2}} e^{-i\frac{k_y a}{2}}) e^{i\,0.272 k_z c/2}$$

$$T_{11} = l_2 n_2 \left[\, t_3(pp\sigma) - t_3(pp\pi) \,\right] (e^{i\frac{k_x a}{2}} e^{i\frac{k_y a}{2}} - e^{-i\frac{k_x a}{2}} e^{-i\frac{k_y a}{2}}) e^{i\,0.272 k_z c/2}$$

$$T_{12} = l_2 n_2 \left[\, t_3(pp\sigma) - t_3(pp\pi) \,\right] (e^{i\frac{k_x a}{2}} e^{i\frac{k_y a}{2}} - e^{-i\frac{k_x a}{2}} e^{-i\frac{k_y a}{2}}) e^{i\,0.272 k_z c/2}$$

$$T_{13} = \frac{\sqrt{3}}{2}\, t_1(pd\sigma) e^{i\frac{k_x a}{2}}$$

$$T_{14} = -\frac{1}{2} t_1(pd\sigma) e^{i\frac{k_x a}{2}}$$

$$T_{15} = t_1(pd\pi) e^{i\frac{k_x a}{2}}$$

$$T_{13}' = -\frac{\sqrt{3}}{2}\, t_1(pd\sigma) e^{i\frac{k_y a}{2}}$$

$$T_{14}' = -\frac{1}{2} t_1(pd\sigma) e^{i\frac{k_y a}{2}}$$

$$T_{15}' = t_1(pd\pi) e^{i\frac{k_y a}{2}}$$

$$T_{16} = 0$$

$$T_{17} = 0$$

$$T_{18} = \frac{\sqrt{3}}{2}\left[\, -t(dd\sigma) + t(dd\delta) \,\right](\cos k_x a - \cos k_y a), \tag{8.6}$$

where

$$l_1 = \frac{0.5a}{\sqrt{(0.5a)^2 + (0.364c/2)^2}}$$

$$n_1 = \frac{0.364c/2}{\sqrt{(0.5a)^2 + (0.364c/2)^2}}$$

$$l_2 = \frac{0.5a}{\sqrt{2(0.5a)^2 + (0.272c/2)^2}}$$

$$n_2 = \frac{0.272c/2}{\sqrt{2(0.5a)^2 + (0.272c/2)^2}}. \tag{8.7}$$

Appendix C. The k Dependence of the Effective Interaction Part of the Hamiltonian

By using the approximation that the effective interaction term $\tilde{H}_{int}$ have matrix elements only between nearest neighbor atomic orbitals, we can represent the k dependence of the effective interaction part of the hamiltonian matrix, $\tilde{H}_{int}(k)$, as follows,

for the matrix elements between A-site and A-site, or between B-site and B-site,

for $O(1)^1$–$O(1)^1$ $\quad H_{ab}^{int}(k) = S_{ab} + A_{ab}$

for $O(1)^1$–$O(1)^2$ $\quad H_{ab}^{int}(k) = S_{ab}\cos\dfrac{k_x - k_y}{2} + A_{ab}\sin\dfrac{k_x - k_y}{2}$

for $O(1)^1$–$O(2)^1$ $\quad H_{ab}^{int}(k) = (S_{ab} + A_{ab})e^{-ik_x a/2}e^{i\,0.364k_z c/2}$

for $O(1)^1$–$O(2)^2$ $\quad H_{ab}^{int}(k) = (S_{ab} + A_{ab})e^{-ik_x a/2}e^{-i\,0.364k_z c/2}$

for $O(1)^1$–Cu $\quad H_{ab}^{int}(k) = (S_{ab} + A_{ab})e^{-ik_x a/2}$

for $O(1)^2$–$O(1)^2$ $\quad H_{ab}^{int}(k) = S_{ab} + A_{ab}$

for $O(1)^2$–$O(2)^1$ $\quad H_{ab}^{int}(k) = (S_{ab} + A_{ab})e^{-ik_y a/2}e^{i\,0.364k_z c/2}$

for $O(1)^2$–$O(2)^2$ $\quad H_{ab}^{int}(k) = (S_{ab} + A_{ab})e^{-ik_y a/2}e^{-i\,0.364k_z c/2}$

for $O(1)^2$–Cu $\quad H_{ab}^{int}(k) = (S_{ab} + A_{ab})e^{-ik_y a/2}$

for $O(2)^1$–$O(2)^1$ $\quad H_{ab}^{int}(k) = S_{ab} + A_{ab}$

for $O(2)^1$–$O(2)^2$ $\quad H_{ab}^{int}(k) = (S_{ab}\cos\dfrac{k_x - k_y}{2} + A_{ab}\sin\dfrac{k_x - k_y}{2})e^{i\,0.272k_z c/2}$

for $O(2)^1$–Cu $\quad H_{ab}^{int}(k) = (S_{ab} + A_{ab})e^{-i\,0.364k_z c/2}$

for $O(2)^2$–$O(2)^2$ $\quad H_{ab}^{int}(k) = S_{ab} + A_{ab}$

for $O(2)^2$–Cu $\quad H_{ab}^{int}(k) = (S_{ab} + A_{ab})e^{i\,0.364k_z c/2}$

for Cu–Cu $\quad H_{ab}^{int}(k) = S_{ab} + A_{ab}$

$$(8.8)$$

and for the matrix elements between A-site and B-site, or between B-site and A-site,

for $O(1)^1$–$O(1)^1$ $\quad H_{ab}^{int}(k) = S_{ab} + A_{ab}$

for $O(1)^1$–$O(1)^2$ $\quad H_{ab}^{int}(k) = S_{ab}\cos\dfrac{k_x + k_y}{2} + A_{ab}\sin\dfrac{k_x + k_y}{2}$

for $O(1)^1$–$O(2)^1$ $\quad H_{ab}^{int}(k) = (S_{ab} + A_{ab})e^{ik_x a/2}e^{i\,0.364k_z c/2}$

for $O(1)^1$–$O(2)^2$ $\quad H_{ab}^{int}(k) = (S_{ab} + A_{ab})e^{ik_x a/2}e^{-i\,0.364k_z c/2}$

for $O(1)^1$–Cu $\quad H_{ab}^{int}(k) = (S_{ab} + A_{ab})e^{ik_x a/2}$

for $O(1)^2$–$O(1)^2$ $\quad H_{ab}^{int}(k) = S_{ab} + A_{ab}$

for $O(1)^2$–$O(2)^1$ $\quad H_{ab}^{int}(k) = (S_{ab} + A_{ab})e^{ik_y a/2}e^{i\,0.364k_z c/2}$

for $O(1)^2$–$O(2)^2$ $\quad H_{ab}^{int}(k) = (S_{ab} + A_{ab})e^{ik_y a/2}e^{-i\,0.364k_z c/2}$

for $O(1)^2$–Cu $\quad H_{ab}^{int}(k) = (S_{ab} + A_{ab})e^{ik_y a/2}$

for $O(2)^1$–$O(2)^1$ $\quad H_{ab}^{int}(k) = S_{ab} + A_{ab}$

for $O(2)^1$–$O(2)^2$ $\quad H_{ab}^{int}(k) = (S_{ab}\cos\dfrac{k_x + k_y}{2} + A_{ab}\sin\dfrac{k_x + k_y}{2})e^{i\,0.272k_z c/2}$

for $O(2)^1$–Cu $\quad H_{ab}^{int}(k) = S_{ab} + A_{ab}$

for $O(2)^2$–$O(2)^2$ $\quad H_{ab}^{int}(k) = S_{ab} + A_{ab}$

for $O(2)^2$–Cu $\quad H_{ab}^{int}(k) = S_{ab} + A_{ab}$

for Cu–Cu $\quad H_{ab}^{int}(k) = S_{ab}(\cos k_x a + \cos k_y a) + A_{ab}(\sin k_x a + \sin k_y a)$

$\qquad\qquad\qquad\qquad\quad + S'_{ab}(\cos k_x a - \cos k_y a) + A'_{ab}(\sin k_x a - \sin k_y a)$

$$(8.9)$$

where a and b denote $2p_x$, $2p_y$ and $2p_z$ atomic orbitals for each of eight oxygen atoms and $3d_{yz}$, $3d_{xz}$, $3d_{xy}$, $3d_{x^2-y^2}$ and $3d_{z^2}$ atomic orbitals for each of two Cu atoms in the antiferromagnetic unit cell.

Appendix D. The Explicit Forms of the Electron-Phonon Interaction

In this appendix the explicit forms of the electron-phonon interaction $g_\mu^\alpha(kk')$ are given for $\mu = $ Cu, O(1)^1, O(1)^2, O(2)^1 and O(2)^2 which are the copper atom, the oxygen atoms in CuO$_2$ plane and the apical oxygen atoms, respectively.

$$g^x_{Cu}(kk') = -\frac{1}{\sqrt{N}} [\ A_s{}^*(k)_{16}A(k')_1 T^x_{1,16}(k')^* + A^*(k)_1 A_s(k')_{16} T^x_{1,16}(k)$$
$$+ A_s{}^*(k)_{17}A(k')_1 T^x_{1,17}(k')^* + A^*(k)_1 A_s(k')_{17} T^x_{1,17}(k) \ ],$$

$$g^x_{O(1)^1}(kk') = +\frac{1}{\sqrt{N}} [\ A_s{}^*(k)_1 A(k')_{16} T^x_{1,16}(k') + A^*(k)_{16} A_s(k')_1 T^x_{1,16}(k)^*$$
$$+ A_s{}^*(k)_1 A(k')_{17} T^x_{1,17}(k') + A^*(k)_{17} A_s(k')_1 T^x_{1,17}(k)^* \ ],$$

$$g^y_{Cu}(kk') = -\frac{1}{\sqrt{N}} [\ A_s{}^*(k)_{16}A(k')_5 T^y_{5,16}(k')^* + A^*(k)_5 A_s(k')_{16} T^y_{5,16}(k)$$
$$+ A_s{}^*(k)_{17}A(k')_5 T^y_{5,17}(k')^* + A^*(k)_5 A_s(k')_{17} T^y_{5,17}(k) \ ],$$

$$g^y_{O(1)^2}(kk') = +\frac{1}{\sqrt{N}} [\ A_s{}^*(k)_5 A(k')_{16} T^y_{5,16}(k') + A^*(k)_{16} A_s(k')_5 T^y_{5,16}(k)^*$$
$$+ A_s{}^*(k)_5 A(k')_{17} T^y_{5,17}(k') + A^*(k)_{17} A_s(k')_5 T^y_{5,17}(k)^* \ ],$$

$$g^z_{Cu}(kk') = -\frac{1}{\sqrt{N}} [\ A_s{}^*(k)_{17}A(k')_9 T^z_{9,17}(k')^* + A^*(k)_9 A_s(k')_{17} T^z_{9,17}(k)$$
$$+ A_s{}^*(k)_{17}A(k')_{12} T^z_{12,17}(k')^* + A^*(k)_{12} A_s(k')_{17} T^z_{12,17}(k) \ ],$$

$$g^z_{O(2)^1}(kk') = +\frac{1}{\sqrt{N}} [\ A_s{}^*(k)_9 A(k')_{17} T^z_{9,17}(k') + A^*(k)_{17} A_s(k')_9 T^z_{9,17}(k)^*$$
$$+ A_s{}^*(k)_{17} A(k')_{17} T^{*z}_{9,17}(k' - k) + A_s{}^*(k)_{16} A(k')_{16} T^{*z}_{9,16}(k' - k)],$$

$$g^z_{O(2)^2}(kk') = +\frac{1}{\sqrt{N}} [\ A_s{}^*(k)_{12} A(k')_{17} T^z_{12,17}(k') + A^*(k)_{17} A_s(k')_{12} T^z_{12,17}(k)^*$$
$$+ A_s{}^*(k)_{17} A(k')_{17} T^{*z}_{12,17}(k' - k) + A_s{}^*(k)_{16} A(k')_{16} T^{*z}_{12,16}(k' - k)],$$

$$(8.10)$$

where $A(k)_i$ is the i-th element of the transformation matrix and $A_s(k)_i$ is defined as,

$$A_s(k)_i \ = \ -A(k)_i \quad \text{when} \quad \gamma \text{ is 2nd-mode and } i \text{ is } B\text{-site}$$
$$= \ A(k)_i \quad \text{otherwise.}$$

$$(8.11)$$

The matrix elements of the transfer interactions in Eq.(8.10), between an A-site and another A-site or between a B-site and another B-site, $T^\alpha_{\mu' a \nu' b}(k)$, are expressed as follows,

$$T^x_{1,16}(k) = T^x_{O(1)^1 x \ Cu x^2-y^2}(k) = \frac{\sqrt{3}}{2} t'_1(pd\sigma)e^{-i\frac{k_x a}{2}} = -T^x_{16,1}(k)^*,$$

$$T^x_{1,17}(k) = T^x_{O(1)^1 x \ Cu z^2}(k) = -\frac{1}{2} t'_1(pd\sigma)e^{-i\frac{k_x a}{2}} = -T^x_{17,1}(k)^*,$$

$$T^y_{5,16}(k) = T^y_{O(1)^2 y \ Cu x^2-y^2}(k) = -\frac{\sqrt{3}}{2} t'_1(pd\sigma)e^{-i\frac{k_y a}{2}} = -T^y_{16,5}(k)^*,$$

$$T^y_{5,17}(k) = T^y_{O(1)^2 y \ Cu z^2}(k) = -\frac{1}{2} t'_1(pd\sigma)e^{-i\frac{k_y a}{2}} = -T^y_{17,5}(k)^*,$$

$$T^z_{9,17}(k) = T^z_{O(2)^1 z \ Cu z^2}(k) = t'_2(pd\sigma)e^{-i \ k_z 0.364 c/2} = -T^z_{17,9}{}^*(k),$$

$$T^z_{12,17}(k) = T^z_{O(2)^2 z \ Cu z^2}(k) = t'_2(pd\sigma)e^{i \ k_z 0.364 c/2} = -T^z_{17,12}{}^*(k),$$

$$T^{*z}_{9,16}(k) = T^{*z}_{O(2)^1 z \ Cu x^2-y^2}(k) = E'_{A_{1g}} e^{-i \ k_z 0.364 c/2} = T^{*z}_{12,16}(k),$$

$$T^{*z}_{9,17}(k) = T^{*z}_{O(2)^2 z \ Cu z^2}(k) = E'_{B_{1g}} e^{-i \ k_z 0.364 c/2} T^{*z}_{12,17}(k)$$

$$(8.12)$$

where $t'_i(pd\sigma)$ is the derivative of transfer integral between a Cu d orbital and a neighbouring O p orbital. The transfer integral $t_i(pd\sigma)$ have been defined in section 3-2. For the matrix elements between A-site and B-site, those are expressed as

$$T^x_{1,16}(k) = T^x_{O(1)^1 x \ Cu x^2-y^2}(k) = \frac{\sqrt{3}}{2} t'_1(pd\sigma)e^{i\frac{k_x a}{2}} = -T^x_{16,1}(k)^*,$$

$$T^x_{1,17}(k) = T^x_{O(1)^1 x \ Cu z^2}(k) = -\frac{1}{2} t'_1(pd\sigma)e^{i\frac{k_x a}{2}} = -T^x_{17,1}(k)^*,$$

$$T^y_{5,16}(k) = T^y_{O(1)^2 y \ Cu x^2-y^2}(k) = -\frac{\sqrt{3}}{2} t'_1(pd\sigma)e^{i\frac{k_y a}{2}} = -T^y_{16,5}(k)^*,$$

$$T^y_{5,17}(k) = T^y_{O(1)^2 y \ Cu z^2}(k) = -\frac{1}{2} t'_1(pd\sigma)e^{i\frac{k_y a}{2}} = -T^y_{17,5}(k)^*,$$

$$T^z_{9,17}(k) = T^z_{O(2)^1 x \ Cu z^2}(k) = 0 = -T^z_{17,9}{}^*(k),$$

$$T^x_{12,17}(k) = T^x_{O(2)^2 x \ Cu z^2}(k) = 0 = -T^x_{17,12}{}^*(k).$$

$$(8.13)$$

Appendix E.

Repulsive Electron-Phonon Interaction between Up- and Down-Spin Carriers with Different Wave Function

As we mentioned before in Chapter 4, the wave function for up-spin carriers is different from that for down-spin carriers, which makes the electron-phonon coupling constant for up-spin carriers different from that for down-spin carriers. Now we will explain why $V_\uparrow^\gamma(k, k')$ is different from $V_\downarrow^\gamma(k, k')$. Any phonon mode in the ordinary Brillouin zone becomes to have two branches, as a result of folding it into the AF Brillouin zone. One branch corresponds to "acoustic type mode" in which the motion of the two neighbouring CuO_6 octahedra with localized up- and down-spins is the same except for the phase factor $\exp(iq \cdot a)$, while the other to "optic type mode" in which the motion of the two neighbouring CuO_6 octahedra is opposite except for the phase factor $\exp(iq \cdot a)$. If we denote the positions of two atoms in the l-th AF unit cell whose distance is separated by a, the translation vector from one Cu atom to a neighbouring Cu atom, by $R_{l\mu1}$ and $R_{l\mu2}$, then $R_{l\mu2} = R_{l\mu1} + a$. The displacement of the atom at $R_{l\mu2}$, $\delta R_{l\mu2}$, is related to that at $R_{l\mu1}$, $\delta R_{l\mu1}$, as

$$\delta R_{l\mu2} = \pm \exp(iqa)\delta R_{l\mu1}, \tag{8.14}$$

where the sign $+$ and $-$ correspond to "acoustic type phonon mode" and "optic type phonon mode" respectively. Here it should be noted that a is non-primitive translation vector in the AF unit cell though it is primitive translation vector in the ordinary unit

138

cell. While, by using Bloch theorem, the wave functions for up- and down-spin carriers are written as

$$\Psi_{k\uparrow}(r) = \exp(ikr)u_{k\uparrow}(r) \tag{8.15}$$

$$\Psi_{k\downarrow}(r) = \exp(ikr)u_{k\downarrow}(r) \tag{8.16}$$

where $u_{k\uparrow}(r)$ and $u_{k\downarrow}(r)$ have the periodicity of the lattice of the AF unit cell. In the present model, the effective Hamiltonian for up- and down-spin carriers, $H_{\text{eff}\uparrow}(r)$ and $H_{\text{eff}\downarrow}(r)$, satisfy the relation $H_{\text{eff}\downarrow}(r + a) = H_{\text{eff}\uparrow}(r)$, then

$$u_{k\downarrow}(r + a) = u_{k\uparrow}(r) \tag{8.17}$$

This leads to the relation

$$\Psi_{k\downarrow}(r + a) = \exp(ika)\Psi_{k\uparrow}(r) \tag{8.18}$$

From Eq. (6.3) (8.14) and (8.18) it is clear that $V_\uparrow^\gamma(k, k')$ and $V_\downarrow^\gamma(k, k')$ satisfy the following relation;

$$V_\uparrow^\gamma(k, k') = \pm \exp(iK \cdot a)V_\downarrow^\gamma(k, k'), \tag{8.19}$$

where $K = k - k' - q$ and $a = (a, 0, 0)$. The vector K takes a value of $mQ_1 + nQ_2 = (\pi/a, \pi/a, 0)m + (-\pi/a, \pi/a, 0)n$, with m and n being integers. And $\exp(iK \cdot a)$ takes a value of $+1$ or -1, depending on whether a scattering process is normal or umklapp.

For the electron-phonon interaction matrix element in the case of an ordinary unit cell without the AF order, $\tilde{V}^\gamma(k, k')$, we have

$$\tilde{V}_\uparrow^\gamma(k, k')\tilde{V}_\downarrow^\gamma(-k, -k') = \left|\tilde{V}_\uparrow^\gamma(k, k')\right|^2 \tag{8.20}$$

and in this case the spectral function $\alpha^2 \tilde{F}_{\uparrow\downarrow}(\Omega, \theta, \theta')$ is always positive, $i.e.$ attractive, for any combination of k and k'. In the case of the AF unit cell which we are considering in this paper, however, we have

$$V_\uparrow^\gamma(k, k')V_\downarrow^\gamma(-k, -k') = \pm \exp(iK \cdot a)\left|V_\uparrow^\gamma(k, k')\right|^2 \tag{8.21}$$

and $\alpha^2 F_{\uparrow\downarrow}(\Omega, \theta, \theta')$ changes its sign according to the sign of $\pm \exp(iK \cdot a)$.

139

Appendix F.

D-wave Component of a Spectral Function and D-wave Superconductivity

In order to study the possibility of the occurrence of d-wave superconductivity, we have to solve the k-dependent Eliashberg equation. Let a set of functions, $F_J(k)$'s, be complete and orthonormal when integrated on the Fermi surfaces. It is clear that $F_J(k)$'s reflect the symmetry of the band structure. In terms of this set of functions we can write

$$\Delta(\omega, k) = \sum_J \Delta_J(\omega) F_J(k) \tag{8.22}$$

$$Z(\omega, k) = \sum_J Z_J(\omega) F_J(k) \tag{8.23}$$

$$\alpha^2 F_{\uparrow\uparrow}(\Omega, k, k') = \sum_{JJ'} \alpha^2 F_{\uparrow\uparrow JJ'}(\Omega) F_J(k) F_{J'}(k') \tag{8.24}$$

$$\alpha^2 F_{\uparrow\downarrow}(\Omega, k, k') = \sum_{JJ'} \alpha^2 F_{\uparrow\downarrow JJ'}(\Omega) F_J(k) F_{J'}(k'). \tag{8.25}$$

With the use of these expansion coefficients of the gap function $\Delta(\omega, k)$, the renormalization function $Z(\omega, k)$ and the spectral functions $\alpha^2 F_{s,s'}(\Omega, k, k')$, we obtain the following linearized Eliashberg equation for anisotropic superconductivity.

$$[1 - Z_J(\omega)]\omega = \sum_{J'} \int_{-\infty}^{\infty} d\omega' \int_0^{\infty} d\Omega \; \frac{\rho(\omega' Z(\omega'))}{\rho(E_F)} \alpha^2 F_{\uparrow\uparrow JJ'}(\Omega) I(\omega, \omega', \Omega) \tag{8.26}$$

$$[\Delta(\omega) Z(\omega)]_J = -\sum_{J'} \int_{-\infty}^{\infty} d\omega' \int_0^{\infty} d\Omega \; \frac{\rho(\omega' Z(\omega'))}{\rho(E_F)} \alpha^2 F_{\uparrow\downarrow JJ'}(\Omega) I(\omega, \omega', \Omega) \frac{\Delta_{J'}(\omega')}{\omega'} \tag{8.27}$$

where

$$I(\omega, \omega', \Omega) = \frac{1 - f(\omega')}{\omega - \Omega - \omega'} + \frac{f(\omega')}{\omega + \Omega - \omega'} \tag{8.28}$$

$$f(\omega) = \frac{1}{1 + \exp(\omega'/kT)} \tag{8.29}$$

$$\tag{8.30}$$

Here $\rho(\omega)$ is the renormalized density of states of the hole carrier at energy ω. As we have already noted in Chapter 6, the spectral function which appears in the formula for the renormalization function Eq.(8.26), must be $\alpha^2 F_{\uparrow\uparrow JJ'}(\Omega)$ because this term contains the processes of virtual emissions and absorptions of various modes of phonons by a single electron, while the spectral function in Eq.(8.27) is $\alpha^2 F_{\uparrow\downarrow JJ'}(\Omega)$ which contains scattering processes of a pair of electrons from one pair state $(k \uparrow, -k \downarrow)$ to a different state $(k' \uparrow, -k' \downarrow)$.

From the two dimensional properties of LSCO, it seems to be an adequate approximation to take $\cos n\theta$'s as the complete and orthonormal set of functions, $F_J(k)$'s, where $\theta = \tan^{-1}(k_y/k_x)$. Then the linearized Eliashberg equation becomes,

$$[1 - Z_n(\omega)]\omega = \sum_{n'} \int_{-\infty}^{\infty} d\omega' \int_0^{\infty} d\Omega \; \frac{\rho(\omega' Z(\omega'))}{\rho(E_F)} \alpha^2 F_{\uparrow\uparrow nn'}(\Omega) I(\omega, \omega', \Omega) \tag{8.31}$$

$$[\Delta(\omega) Z(\omega)]_n = -\sum_{n'} \int_{-\infty}^{\infty} d\omega' \int_0^{\infty} d\Omega \; \frac{\rho(\omega' Z(\omega'))}{\rho(E_F)} \alpha^2 F_{\uparrow\downarrow nn'}(\Omega) I(\omega, \omega', \Omega) \frac{\Delta_{n'}(\omega')}{\omega'} \tag{8.32}$$

where

$$\Delta(\omega, \theta) = \sum_n C_n \Delta_n(\omega) \cos(n\theta) \tag{8.33}$$

$$Z(\omega, \theta, \theta') = \sum_n C_n Z_n(\omega) \cos(n\theta) \tag{8.34}$$

$$\alpha^2 F_{\uparrow\downarrow}(\Omega, \theta, \theta') = \sum_{nn'} C_n C_{n'} \alpha^2 F_{\uparrow\downarrow nn'}(\Omega) \cos n\theta \cos n\theta'. \tag{8.35}$$

where $C_n = 1/\sqrt{2\pi}$ for $n = 0$ and $C_n = 1/\sqrt{\pi}$ for $n \neq 0$. In Chapter 6 we have calculated the spectral function and shown that among the components of the spectral function, $\alpha^2 F_{\uparrow\uparrow nn'}(\Omega)$'s and $\alpha^2 F_{\uparrow\downarrow nn'}(\Omega)$'s, all terms are small and negligible except for $\alpha^2 F_{\uparrow\uparrow 0,0}(\Omega)$ and $\alpha^2 F_{\uparrow\downarrow 2,2}(\Omega)$. Following the expressions in Chapter 6, we include the normalization factor C_n in the expressions of $\alpha^2 F$ and for simplicity we use the notation $\alpha^2 F_{\uparrow\uparrow}^{(0)}(\Omega)$ and $\frac{1}{2}\alpha^2 F_{\uparrow\downarrow}^{(2)}(\Omega)$ for $\alpha^2 F_{\uparrow\uparrow 0,0}(\Omega)$ and $\alpha^2 F_{\uparrow\downarrow 2,2}(\Omega)$ respectively. Hereafter we use this notation. Then we obtain the following equation,

$$[1 - Z_0(\omega)]\,\omega = \int_{-\infty}^{\infty} d\omega' \int_0^{\infty} d\Omega \; \frac{\rho(\omega' Z(\omega'))}{\rho(E_F)} \alpha^2 F_{\uparrow\uparrow}^{(0)}(\Omega) I(\omega, \omega', \Omega) \tag{8.36}$$

$$\Delta_2(\omega) Z_0(\omega) = -\int_{-\infty}^{\infty} d\omega' \int_0^{\infty} d\Omega \; \frac{\rho(\omega' Z(\omega'))}{\rho(E_F)} \frac{\alpha^2 F_{\uparrow\uparrow}^{(2)}(\Omega)}{2} I(\omega, \omega', \Omega) \frac{\Delta_2(\omega')}{\omega'}$$
$$\tag{8.37}$$

Note that the component of the spectral function which connects the s- and d-wave symmetry, $\alpha^2 F_{\uparrow\downarrow 2,0}(\Omega)$, vanishes from C_4 symmetry, and that the d-wave component of the spectral function $\alpha^2 F_{\uparrow\downarrow}^{(2)}(\Omega)$ is large while the s-wave component $\alpha^2 F_{\uparrow\downarrow}^{(0)}(\Omega)$ is negligibly small, as we have seen in Chapter 6. The d-wave component $\alpha^2 F_{\uparrow\downarrow}^{(2)}(\Omega)$ contributes to the formation of d-wave pairing as is known from Eq.(8.37). These results establish the appearance of the d-wave superconductivity in LSCO system.

References

[1] J. G. Bednorz and K. A. Müller, Z. Phys. **B64** (1986) 189.

[2] Y. Tokura *et al*, Phys. Rev. **B39** (1989) 9704.

[3] Y. Tokura, H. Takagi and S. Uchida, Nature **337** (1989) 345.

[4] See, for example, Mechanisms of High Temperature Superconductivity, (Springer Series in Materials Science 11, eds. H. Kamimura and A. Oshiyama, Springer-Verlag, Heidelberg, 1989).

[5] See also, Strong Correlation and Superconductivity, (Springer Series in Solid-State Sciences 89, eds. H. Fukuyama, S. Maekawa and A. P. Malozemoff, Springer-Verlag, Heidelberg, 1989).

[6] H. Kamimura : in *Progress in High Temperature Superconductivity* Vol.14, ed. S. Lundqvist, E. Tosatti, M. P. Tosi and Y. Lu (World Scientific,Singapore,1988) p.163.

[7] T. Schimizu and H. Kamimura: J. Phys. Soc. Jpn. **59** (1990) 3691.

[8] H. Kamimura and M. Eto, J. Phys. Soc. Jpn. **59** (1990) 3053.

[9] N. Shima, K. Shiraishi, T. Nakayama, A. Oshiyama and H. Kamimura : in *Proc. 1st Int. Conf. on Electronic Materials*, ed. T. Sugano, R. P. H. Chang, H. Kamimura, I. Hayashi and T. Kamiya (MRS, Pittsberg) (1988), p. 51.

[10] H. Ushio and H. Kamimura,solid state commun. **76** (1990) 1115

[11] H. Kamimura, M. Eto, K. Ishida, S. Matsuno, T. Schimizu and H. Ushio, Supercond. Sci. Technol. **4** (1991) s121- s123

[12] H. Ushio, T. Schimizu and H. Kamimura, J. Phys. Soc. Jpn. **60** (1991) 1445.

[13] S. Matsuno, H. Ushio and H. Kamimura, Physica C **185-189** (1991) 1695.

[14] H. Kamimura,T. Schimizu and H. Ushio, Physica C **185-189** (1991) 1697.

[15] H. Ushio and H. Kamimura, Physica C **185-189** (1991) 1699.

[16] H. Kamimura, M. Eto, S. Matsuno and H. Ushio, Comments on Condensed Matter Physics Vol.15, No.5 & 6 (1992) p303-325.

[17] H. Ushio and H. Kamimura, in *Elementary Excitation in Solids*, A Festschrift in honour of Professor Minko Balkanski, eds. J. L. Birman,C. Sebenne and R. F. Wallis (Elsevier Science Publishers, Amsterdam, 1992) 367.

[18] H. Ushio and H. Kamimura, J. Phys. Soc. Jpn. **61** (1992) 2877.

[19] C. T. Chen *et al.*, Phys. Rev. Lett. **68** (1992) 2543.

[20] R. J. Birgeneau*et al.*, Phys. Rev. **B 38** (1988) 6614.

[21] H. Kamimura and Y. Suwa, J. Phys. Soc. Jpn. **62** (1993) 3368.

[22] N. F. Mott: in *New Horizons in Low-Dimensional Electron Systems*, Festschrift in Honour of Professor H. Kamimura, ed. H. Aoki *et al.* (Kluwer Academic Publishers, Amsterdam, 1991) p.181.

[23] M. L. Cohen: in *New Horizons in Low-Dimensional Electron Systems*, Festschrift in Honour of Professor H. Kamimura, ed. H. Aoki *et al.* (Kluwer Academic Publishers, Amsterdam, 1991) p.191.

[24] A. Sano, Y. Suwa and H. Kamimura, to be published in International Journal of Modern Physics B.

[25] K. Ueda *et al.*, J. Phys. Chem. Solids **53** (1992) 1515.

[26] M. K. Crawford, M. N. Kunchur, W. E. Farneth, E. M. McCarron,III, and S. J. Poon, Phys. Rev. **B41**, (1989)282.

[27] M. K. Crawford, W. E. Farneth, E. M. McCarron III, R. L. Harlow and A. H. Moudden, Science,**250**, (1990) 1390

[28] M. Ronay *et al.*, Phys. Rev. **B45** (1992) 355.

[29] B.Renker et al, Z. Phys. **B73**, (1988) 309.

[30] W.Reichardt, N.Pyka, L.Pintschovius, B.Hennion and G.Collin, Physica **C162-164**, (1989) 464.

[31] F.Siakey, S.L.Cooper, M.V.Klein, J.P.Rice and D.M.Ginsberg, Phys. Rev. **B39**, (1989) 2781.

[32] N. Miyakawa *et al.*, J. Phys. Soc. Jpn. **59** (1990) 2473.

[33] D. Shimada *et al.*, J. Phys. Soc. Jpn. **58** (1989) 387.

[34] N. Miyakawa *et al.*, J. Phys. Soc. Jpn. **58** (1989) 1141.

[35] N. Miyakawa *et al.*, J. Phys. Soc. Jpn. **58** (1989) 383.

[36] H. Kamimura, S. Matsuno, Y. Suwa and H. Ushio, Comments on Condensed Matter Physics Vol.17, No.2 (1994) p107-134.

[37] H. Kamimura, S. Matsuno, Y. Suwa and H. Ushio, to be published in *Quantum Theory of Real Materials* a Festschrift in honour of Prof. M. Cohen (Kluwer Academic Publishers) (1996) p465-p490.

[38] H. Kamimura, S. Matsuno, Y. Suwa and H. Ushio, Physica **C263** (1996) 126.

[39] H. Kamimura, S. Matsuno, Y. Suwa and H. Ushio, Materials Science and Engineering **B 41** (1996) 10.

[40] H. Kamimura, S. Matsuno, Y. Suwa and H. Ushio, Phys. Rev. Lett**77** (1996) 723.

[41] See, for example, Proceedings of the Int. Conf. on stripes, the electron-phonon interaction and hightemperature superconductivity, ed. A. Bianconi, special issue of J. Superconductivity (1997).

[42] H. Kamimura and H. Ushio, Solid State Commun. **91** (1994) 97.

[43] H. Ushio and H. Kamimura, J. Phys. Soc. Jpn. Vol.64 No.7 (1995) 2585.

[44] H. Takagi, T. Ido, S. Ishibashi, M. Uota, S. Uchida and Y. Tokura, Phys. Rev. **B40**, (1989) 2254.

[45] H. Takagi, Y. Tokura and S. Uchida : in *Mechanisms of High Temperature Superconductivity*, ed. H. Kamimura and A. Oshiyama (Springer, Heidelberg, 1989) Springer Series in Materials Science Vol.11, p. 238.

[46] H. Takagi, S. Uchida and Y. Tokura, Phys. Rev. Lett. **62** (1989) 1197.

[47] J. B. Torrance *et al*, Phys. Rev. **B40** (1989) 8872.

[48] B. Ellman, H. M. Jaeger,D. P. Katz, T. F. Rosenbaum, A. S. Cooper and G. P. Espinosa, Phys. Rev. B 39 (1989) 9012.

[49] M. Gurvitch and A. T. Fiory, Phys. Rev. Letters **59** (1987) 1337.

[50] Y. Iye : in *Mechanisms of High Temperature Superconductivity*, ed. H. Kamimura and A. Oshiyama (Springer, Heidelberg, 1989) Springer Series in Materials Science Vol.11, p. 263.

[51] N. P. Ong, Z. Z. Wang, J. Clayhold, J. M. Tarascon, L. H. Greene and W. R. Mckinnon, Phys. Rev. **B35** (1987) 8807.

[52] K. Kumagai, 4th MMM symposium,Taiwan,1988,April

[53] M. Kato, Y. Maeno and T. Fujita, Physica **C152** (1988) 116.

[54] T. Ito *et al.*, Nature **350** (1991) 596.

[55] B. Bucher *et al.*, Phys. Rev. Lett. **70** (1993) 2012.

[56] G. Kido *et al.*, JJAP Series 7 Mechanisms of Superconductivity (1992) 247

[57] J. R. Cooper *et al* , Phys. Rev. **B35** (1987) 8794.

[58] Y. Ando *et al*, Solid State Commun. **70** (1989) 303.

[59] M. F. Hundley *et al*, Phys. Rev. **B35** (1987) 8800.

[60] J. W. Loram *et al.*, Physica **C162** (1990) 498.

[61] T. Takahashi, JJAP Series 7 Mechanisms of Superconductivity (1992) 141.

[62] T. Takahashi *et al.*, Nature **334** (1988) 691.

[63] S. Uchida *et al.*, JJAP Series 7 Mechanisms of Superconductivity (1992) 133.

[64] S. Uchida *et al.*, Phys. Rev.**B 43** (1991) 7942.

[65] K. Ohbayashi *et al.*, JJAP Series 7 Mechanisms of Superconductivity (1992) 147.

[66] K. Ohbayashi *et al.*, J. Phys. Soc. Jpn. **59** (1990) 4419.

[67] A. Fujimori, JJAP Series 7 Mechanisms of Superconductivity (1992) 125.

[68] A. Fujimori *et al.*, Phys. Rev. **B 39** (1989) 2252.

[69] A. Fujimori *et al.*, Phys. Rev. **B 35** (1987) 8814.

[70] Ohura *et al.*, private communication.

[71] M. Cardona, Physica **C 185-189** (1991) 65.

[72] M. Cardona *et al.*, Solid State Commun. **66** (1988) 1225.

[73] S. Sugai, JJAP Series 7 Mechanisms of Superconductivity (1992) 154.

[74] S. Sugai *et al.*, Solid State Commun. **76** (1990) 371.

[75] Matsuno and Kamimura, submitted to Phys. Rev. Lett..

[76] Y. Endoh *et al.*, JJAP Series 7 Mechanisms of Superconductivity (1992) 174.

[77] Y. Endoh *et al.*, Physica **C263** (1996) 394.

[78] T. E. Mason *et al.*, Phys. Rev. Lett. **71** 919 (1993).

[79] J. Rossat-Mignod *et al.*, *Proc. 19th Int. Conf. Low Tem. Phys.* edited by D. D. Bett, Brighton August 1990North-Holland.

[80] J. Rossat-Mignod *et al.*, Physica Scripta **45** (1992) 74.

[81] Y. Kitaoka *et al.*, JJAP Series 7 Mechanisms of Superconductivity (1992) 185

[82] H. Monien and D. Pines, Phys. Rev. **B41** (1990) 6297.

[83] J. D. Axe *et al.*, Phys. Rev. Lett. **62** (1989) 2751.

[84] R. Moodenbaugh, Y. Xu, M. Suenaga, T. J. Folkerts, and R. N. Shelton, Phys. Rev. **B38** (1988) 4596.

[85] Y. Maeno *et al.*, JJAP Series 7 Mechanisms of Superconductivity (1992) 91

[86] Y. Koike *et al.*, JJAP Series 7 Mechanisms of Superconductivity (1992) 99

[87] K. Kitazawa *et al.*, JJAP Series 7 Mechanisms of Superconductivity (1992) 253

[88] T. Ekino *et al.*, JJAP Series 7 Mechanisms of Superconductivity (1992) 260.

[89] L. C. Bourne *et al*, Phys. Rev. Lett. **58** (1987) 2337.

[90] B. Batlogg *et al*, Phys. Rev. Lett., **58** (1987) 2333

[91] H. Katayama-Yoshida *et al* , Physica bf C156 (1988) 481.

[92] C. C. Tsuei, D. M. News, C. C. Chi,and P. C. Pattnaik, Phys. Rev. Lett. **65**, (1989)2724.

[93] C. C. Tsuei *et al.*, Physica **C 263** (1996) 232.

[94] C. C. Tsuei *et al.*, Phys. Rev. Lett. **72** (1994) 593.

[95] F. C. Zhang and T. M. Rice, Phys. Rev. **B37** (1988) 3759.

[96] W. Weber, Phys. Rev. Lett. **58** (1987) 1371.

[97] M. J. DeWeert, D. A. Papaconstantopoulos and W. E. Pickett, Phys. Rev. **B39** (1989) 4235.

[98] V. I. Anisimov, M. A. Korotin, J. Zaanen and O. K. Andersen, Phys. Rev. Lett. **68** (1992) 345.

[99] K. Motizuki and N. Suzuki : in *Structural Phase Transition in Layered Transition-metal Compounds* (Dordecht, Reidel, 1986) 1-133.

[100] M. Shirai, N. Suzuki and K. Motizuki, J. Phys: Condens. Matter **2** (1990) 3553.

[101] K. Motizuki, M. Shirai and N. Suzuki, in*Proceedings of Second CINVESTAV Superconductivity Symposium* (World Scientific, Singapore, 1990) p.176.

[102] P. Aebi *et al.*, Phys. Rev. Lett. **72** (1994) 2757.

[103] M. Eto and H. Kamimura, J. Phys. Soc. Jpn. **60** (1991) 2311.

[104] Z. X. Shen *et al.*, Phys. Rev. Lett. **70** (1993) 1553.

[105] D. S. Desseau *et al.*, Phys. Rev. Lett. **71** (1993) 2781.

[106] H. Kamimura, S. Ohura and C. T. Chen, in preparation.

[107] D. M. King *et al.*, Phys. Rev. Lett. **73** (1994) 3298.

[108] P. Aebi *et al.*, to be published in Physica **C**.

[109] Z. X. Shen *et al*, to be published in: Proc. Int. Sym. Frontier of High Temperature Superconductivity.

[110] D. S. Marshall *et al.*, Phys. Rev. Lett. **76** (1996) 4841.

[111] J. M. Luttinger and J. C. Ward, Phys. Rev. **118** (1960) 1417; J. M. Luttinger, Phys. Rev. **119** (1960) 1153.

[112] S-W. Cheong *et al.*, Phys. Rev. Lett. **67** (1991) 1791.

[113] R. Micnas and J. Ranninger, Phys. Rev. **B36**, (1987) 4051.

[114] A. P. Ramirez *et al*, Phys. Rev. **BB35** (1987) 8833

[115] J. M. Ziman : in *Electrons and Phonons*, (Oxford Univ. Press, London, 1960).

[116] T. Inoshita and H. Kamimura, Synthetic Metals, **3** (1981) 223.

[117] S. Mase *et al.*, J. Phys. Soc. Jpn. **57** (1988) 607.

[118] H. Fukuyama: Prog. theor. Phys. **42** (1969) 1284.

[119] T. Nishikawa, J. Takeda and M. Sato, J. Phys. Soc. Jpn. **63** 1441 (1994)

[120] J. Takeda, T. Nishikawa and M. Sato, Physica **C231** (1994) 293.

[121] M. Sera *et al.*,Solid State Commun. **92** (1994) 289.

[122] For example, D. Wollman *et al.* Phys. Rev. Lett. **74** (1995) 797.

[123] S. A. Trugman,Phys. Rev. Lett. **65** (1990) 500.

[124] S. Matsuno, H. Ushio, Y. Suwa and H. Kamimura, to be published in International Journal of Modern Physics B.

[125] K. Yamada *et al.*, to be published in J. Supercond., proceedings of Stripes, Lattice Instability and High T_c Superconductivity.

[126] B. Batlogg *et al* , Phys. Rev. Lett. **59** (1987) 912.

[127] T. A. Faltens, Phys. Rev. Lett., **59** (1987) 915.

[128] H. Ushio and H. Kamimura, to be published in International Journal of Modern Physics B.

[129] H. Ushio and H. Kamimura, to be published in Int. J. Mod. Phys.

[130] T. Timusk, C. D. Porter and D. B. Tanner, Phys. Rev. Lett. **66**, (1989) 663.

[131] D. A. Wollman *et al.*, Phys. Rev. Lett. **71** (1993) 2134.